

# Conventional and New Growth Phenomena during Metal Deposition on Transition Metal Dichalcogenides

Dissertation  
zur Erlangung des akademischen Grades  
Doktor der Naturwissenschaften  
(Dr. rer. nat.)  
der Technischen Fakultät  
der Christian-Albrechts-Universität zu Kiel

vorgelegt von  
**Rainer Kunz**

Kiel  
2005

1. Gutachter: Prof. Dr. Franz Faupel

2. Gutachter: Prof. Dr. Lutz Kipp

Datum der mündlichen Prüfung: 10.03.2006

# Contents

<b>1</b>	<b>Introduction</b>	<b>1</b>
<b>2</b>	<b>Microscopic model of diffusion and growth mechanism on surfaces</b>	<b>3</b>
2.1	Adsorption processes . . . . .	4
2.2	Diffusion . . . . .	4
2.3	Surface diffusion and nucleation . . . . .	5
2.4	Growth modes . . . . .	8
2.5	Diffusion limited aggregation . . . . .	9
<b>3</b>	<b>Fracture, buckling and delamination of thin films</b>	<b>10</b>
3.1	Origin of stress . . . . .	10
3.2	Crack driving force and crack resistance . . . . .	11
3.3	Cracking in a film under tension . . . . .	11
3.4	Debonding of a film under compression . . . . .	13
<b>4</b>	<b>The substrates: Transition metal dichalcogenides</b>	<b>15</b>
<b>5</b>	<b>Crystal growth and preparation</b>	<b>18</b>
5.1	Chemical vapor transport . . . . .	18
5.2	Sample preparation . . . . .	18
<b>6</b>	<b>Experimental setup</b>	<b>20</b>
6.1	Scanning tunneling microscopy . . . . .	20
6.2	Scanning electron microscopy . . . . .	21
6.3	Energy dispersive X-ray analysis . . . . .	25
6.4	Atomic force microscopy . . . . .	26
6.5	The UHV deposition system . . . . .	30
<b>7</b>	<b>Surface structures obtained after metal deposition</b>	<b>32</b>
7.1	Homogeneous thin film growth . . . . .	33
7.1.1	WSe <sub>2</sub> . . . . .	33
7.2	Adsorbate structures . . . . .	35
7.2.1	TaS <sub>2</sub> . . . . .	35
7.2.2	TiTe <sub>2</sub> . . . . .	36
7.2.3	HfS <sub>2</sub> . . . . .	38
7.2.4	TiS <sub>2</sub> . . . . .	39
7.3	Adsorbate-Substrate structure reconfiguration . . . . .	40
7.3.1	TaS <sub>2</sub> . . . . .	40
7.3.2	VSe <sub>2</sub> . . . . .	42
<b>8</b>	<b>Variation of the deposition parameters</b>	<b>45</b>
8.1	Deposition amount and rate . . . . .	45
8.2	Substrate temperature . . . . .	46
8.2.1	Subsequent annealing after copper deposition . . . . .	57
8.2.2	Diffusion length . . . . .	59
8.3	Substrate pre-modification by ion beam . . . . .	61

9 Discussion and conclusion	66
10 Summary	75
References	78
List of abbreviations	82
List of publications	83
Acknowledgements	86



# 1 Introduction

Nanotechnology promises big advantages for future applications in health care, medicine, security, electronics, communications and computing.

For a long time two approaches have been pursued to realize nanostructures, the so called top down approach (by the downscaling of conventional techniques) and the bottom up approach (using new techniques that assemble structures atom by atom).

The first approach is making remarkable progress, important candidates like UV-lithography confirm this.

But following the latest ITRS roadmap (Ref. [1]) it will take about 15 years before it is possible to structure nanowires with diameters of 16 nm by conventional lithography.

The latter approach is already used to realize, e.g. nanowires on wafer-scales (Ref. [2]).

But most of these approaches result in self organization phenomena and have the disadvantage that the materials used are not useful for devices: On one hand the properties of the materials cause the self organization process. On the other hand these materials are not useful for any other purpose since there is only little freedom left to fulfill a function. This holds also for self-organization phenomena we observed recently on the layered crystals from the family of the transition metal dichalcogenides (TMDC).

The atomically flat and electronically inert surface of the crystals generates many different nanostructures after the deposition of metal in UHV. One can find a whole bunch of self organized structures such as nanowire networks, fractal shaped islands or areas with geometric figures such as triangles or parallelograms (Ref. [3]).

Nevertheless, understanding why such structures occur on systems like the TMDC crystals is a key to generate nanostructures on other materials that could be used for technical applications.

The approach we want to follow here is to identify the parameters that determine the metal growth process on the layered crystals.

Therefore, it is necessary to investigate the diffusion and the growth of different adsorbants on different TMDC substrates.

Diffusion and growth processes are explained in chapter 2.

Defects in thin films after metal deposition are discussed in chapter 3.

The substances will be introduced in chapter 4 and chapter 5.

The first aim of this thesis is the deposition of different metals on different TMDC substrates.

The occurring structures will be investigated by scanning probe techniques and the experimental techniques are explained in chapter 6.

The results will be presented in chapter 7.

The second aim is the investigation of the most interesting of the observed adsorbate sub-

strate systems by advanced preparation and measurement techniques presented in chapter 8.

Therefore, a new UHV system for controlled and reproducible metal deposition has to be constructed and put into operation. The new preparation chamber gives us the possibility to vary the deposition parameter systematically in order to understand the influence of different deposition parameters like deposition amount or substrate temperature during and after the preparation under constant conditions.

The configuration of the chamber will be presented in chapter 6.5.

An extensive conclusion and discussion of the experimental results with respect to theoretical calculations will be presented in chapter 9.

A summary of the performed preparations, investigations, results and conclusions are given in chapter 10 to get a short overview of this thesis.

## 2 Microscopic model of diffusion and growth mechanism on surfaces

The structure formation on a sample surface after evaporation of metal or molecules (see Ref. [4]) can be extremely complex. The morphology of the structures depends on the growth mode. Essential for the growth modes are the adsorption, diffusion and the nucleation of the deposited material. The conditions under which the processes take place have an influence on the results, as well as the materials chosen for the experiments. Therefore, this chapter will introduce and explain adsorption, diffusion, nucleation and growth modes of material deposited on a surface. Before any growth of deposited material can take place, the material has to be, e.g., evaporated in an effusion cell and an atom impingement on the surface will take place.

### Atom impingement on a surface

On a surface under surrounding (UHV) conditions material will be deposited. The flux  $\Phi$  of impinging atoms or molecules on the surface is given by

$$\Phi = n \int_0^{\infty} v_x dn_x \quad (\text{molecules/cm}^2\text{s}) \quad (2.1)$$

where  $n_x$  is the number and  $v_x$  the Boltzmann velocity of the impinging atoms.

At thermal equilibrium, the Maxwell-Boltzmann velocity distribution at temperature  $T$  is

$$f(v_x) = \frac{dn_x}{dv_x} = \sqrt{\frac{m}{2\pi kT}} e^{-\frac{1}{2} \frac{mv_x^2}{kT}} \quad (2.2)$$

with  $m$  the mass of the impinging atoms or molecules and  $k$  the Boltzmann constant.

One gets for the flux by using equations 2.1 and 2.2

$$\Phi = n \sqrt{\frac{m}{2\pi kT}} \int_0^{\infty} v_x e^{-\frac{1}{2} \frac{mv_x^2}{kT}} dv_x = n \sqrt{\frac{kT}{2\pi m}} \quad (2.3)$$

The ideal gas law  $PV = nkT$  with the volume  $V = 1$  yields

$$\Phi = \frac{P}{\sqrt{2\pi mkT}} \quad (2.4)$$

One can substitute appropriate constants and gets for the flux

$$\Phi \approx 3.51 \times 10^{22} \frac{P}{\sqrt{MT}} \quad (2.5)$$

where  $P$  is the pressure in torr and  $M$  the atomic number of atoms or gas molecules. The inverse of the impinging flux  $\Phi$  is the time  $\tau_c$  it takes to cover a surface with a monolayer of molecules

$$\tau_c \approx \frac{N}{3.51 \times 10^{22}} \frac{\sqrt{MT}}{P} \quad (2.6)$$

with  $N$  the number of atoms or molecules the monolayer consists of. The next step of growth is the adsorption process.



## 2.1 Adsorption processes

For any structure formation of a deposited material on a surface it is necessary that the material will not desorb from the surface. The material has to be adsorbed by chemical or physical mechanisms, explained in the next passage.

### Chemi- and physisorption

A qualitative distinction can be made between chemisorption and physisorption in terms of their relative binding strengths and mechanisms.

In chemisorption, a strong chemical bond is formed between the adsorbate atom or molecule and the substrate. In this case, the adsorption energy,  $E_a$ , of the adatom is likely to be comparable to or even larger than the sublimation energy of the substrate (typically a few eV/atom). Physisorption is weaker, and is often being considered as having no chemical interaction involved. The attractive interaction, in this case, is largely due to the van der Waals force. This force is due to fluctuating dipole (and higher order) moments on the interacting adsorbate and substrate, and is present between closed-shell systems. Physisorption energies are in the range of 100 meV/atom (Ref. [4]).

### Condensation

The adsorption of atoms/molecules is often preceded by condensation. The adsorbate needs to stay on the substrate surface for long enough time for the reaction to occur (chemisorption) or simply stick in there (physisorption).

At a certain temperature there is an equilibrium vapor pressure (sublimation pressure); no atoms could be deposited unless one has supersaturation. Normally, supersaturation is only achieved in near vicinity to the substrate surface.

## 2.2 Diffusion

Diffusion is defined as the movement (Fig. 2.1) of chemical species (ions, atoms or molecules) under the influence of a concentration difference  $dc$  (Ref. [5]).

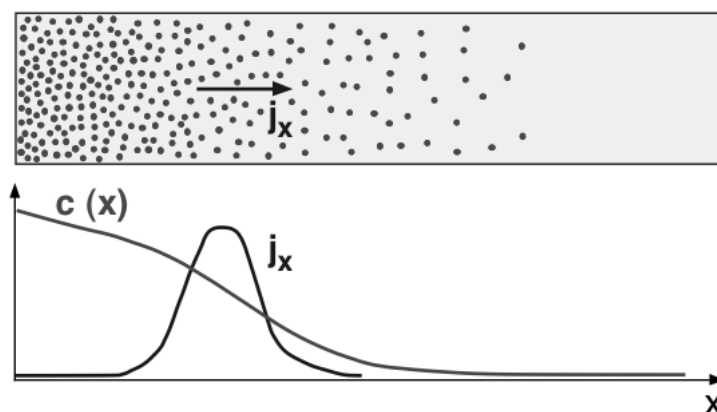


**Figure 2.1:** Schematic graphic of the diffusion process driven by a concentration difference.

The species will move from the high concentration area to the low concentration area until the concentration is uniform in the whole phase. Diffusion in solutions is the most important phenomenon in electrochemistry, but diffusion will also occur in gases and solids. The rate of diffusion (diffusion flux or diffusion current)  $j_x$  is proportional to the gradient of the concentration  $\frac{dc}{dx}$  in the solution, with the proportionality constant  $D$  called the diffusion coefficient. The process can be described by Fick's first law

$$j_x = -D \frac{dc}{dx} \quad (2.7)$$

## 2.3 Surface diffusion and nucleation

This chapter provides a short introduction in order to understand the atomic processes which occur after material deposition on a surface (Ref. [6]).

### Surface Diffusion

Under supersaturation the atoms/molecules in the gas phase condense at the substrate surface. The deposition rate  $R$  or flux  $\Phi$  (of adatoms) is related to the pressure as  $R = \frac{P}{\sqrt{2\pi mkT}}$ .

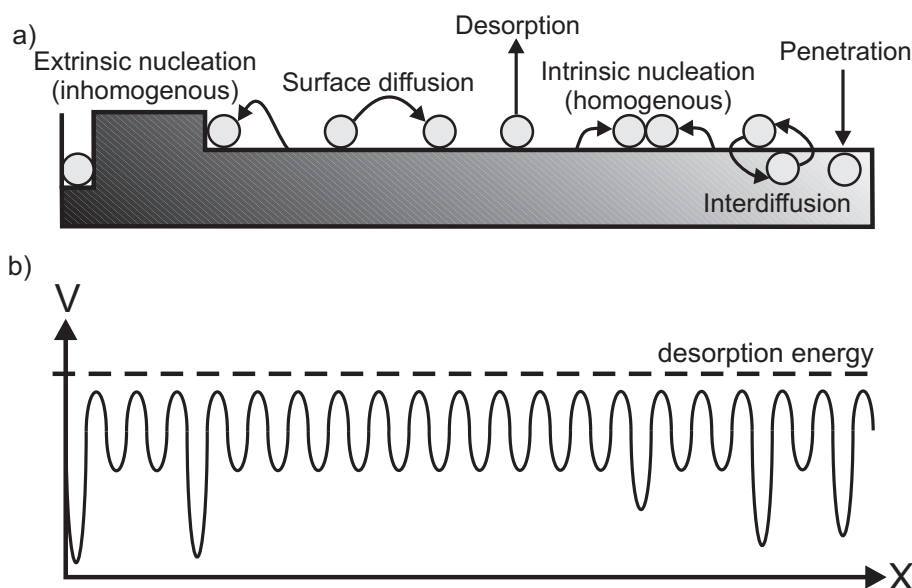


**Figure 2.2:** a) The kinetic surface processes during film growth. b) The spatial distribution of the relative free energy in relation to the different particle positions with respect to the underlying surface atoms.

After the atoms being adsorbed on the surface, they become adatoms with a (positive) adsorption energy  $E_a$ , relative to zero in the vapor (this is sometimes called desorption energy). The desorption rate  $R_d$  of adatoms is roughly given by

$$R_d \approx \nu_a e^{-\left(\frac{E_a}{kT}\right)} \quad (2.8)$$

where  $\nu_a$  is the characteristic atomic vibration frequency and is expected to vary with  $T$ . Note that the desorption energy is assumed to result from lattice vibration only. The adatom can diffuse over the surface, with energy  $E_d$  (migration barrier energy) and the corresponding frequency  $\nu_d$  (order of  $10^{14} \text{ s}^{-1}$ ). Since  $E_d \ll E_a$ , surface diffusion is far more likely than desorption. The probability that the adatom will have enough thermal energy to pass over the barrier within one second is  $\nu_d e^{-\left(\frac{E_d}{kT}\right)}$ . In unit time the adatom makes  $\nu_d$  attempts to pass the barrier, with a probability of  $e^{-\left(\frac{E_d}{kT}\right)}$  of surmounting the barrier on each try. The adatom diffusion coefficient  $D$  (jumping a distance  $l$ ) is then approximately

$$D = \nu_d l^2 e^{-\left(\frac{E_d}{kT}\right)} \quad (2.9)$$

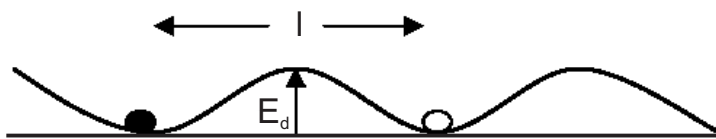


**Figure 2.3:** Schematic sketch of the migration barrier energy  $E_d$ .

This is the mean square displacement of the random walker per unit time, or the adatom diffusion coefficient. It is convenient to express surface areas in terms of substrate unit cells. Then  $D$  becomes the number of unit cells visited by the adatom per unit time. The adatom lifetime  $\tau_a$  before desorption is

$$\tau_a = \nu_d^{-1} e^{-\left(\frac{E_a}{kT}\right)} \quad (2.10)$$

Then the characteristic length  $L$  the adatom can move is given by

$$L = \sqrt{D\tau_a} \quad (2.11)$$

### Nucleation and island growth

In the course of deposition, the atoms (monomer) arrive from the gas phase with a rate  $R$  (Ref. [6]).

For simplicity, we assume the surface temperature is low enough so that only monomers diffuse on the surface and that dimers remain immobile. As deposition proceeds, the number of dimers will increase roughly linearly until their concentration  $n_2$  becomes comparable to the density of monomers  $n_1$ . From there on, the probabilities of a diffusing monomer to encounter one of its own or a dimer become comparable and cluster growth competes with the creation of new stable nuclei (dimers in this model). After the density of stable nuclei  $n_x$  ( $x$  standing for any size that is stable) has increased sufficiently, any further deposition will exclusively lead to island growth. At this saturation island density, the mean free path of diffusing adatoms is equal to the mean island separation and adatoms will attach themselves with much higher probability to existing islands than create new ones. Approaching a coverage of about half a monolayer, islands eventually coalesce which decreases their density. If dimers are immobile and no re-evaporation occurs, then the rate equations for the density of monomers and stable islands are:

$$\frac{dn_1}{dt} = R - 2\sigma_1 D n_1^2 - \sigma_x D n_1 n_x - \kappa_x R (Rt - n_1) - 2\kappa_1 R n_1 \quad (2.12)$$

$$\frac{dn_x}{dt} = \sigma_1 D n_1^2 + \kappa_1 R n_1 \quad (2.13)$$

The terms on the right-hand side of equation 2.12 denote the increase of monomer density due to deposition with flux  $R$ , its decrease due to the encounter of two diffusing adatoms resulting in the creation of a dimer (associated with the disappearance of two atoms), the decrease occurring when a monomer is captured by a stable island, and finally two terms which denote the decrease caused by direct impingement onto stable island density,  $n_x$ .

The last effect is caused by creation of dimers, when either two monomers meet by diffusion or when an atom is directly deposited onto an adatom. In these equations coalescence is neglected; incorporation would add a further term  $-2n_x(R - \frac{dn_1}{dt})$  to the second equation. In general the problem is treated in the mean-field assumption, that is, outside the islands the monomer density immediately takes on its average value. The time evolution of island and monomer densities can be obtained from integration of these equations. Very often, one is interested in the saturation island density, as this reflects the mean free path for monomer diffusion. The temperature dependence of this quantity thus allows to extract information on surface diffusion. The power law expressed by these equations leads to an approximation

$$\frac{D}{R} \approx \frac{L^6}{\ln(L^2)} \quad (2.14)$$

The characteristic length  $L$  can either be identified with the mean island distance or with the mean free path of diffusing adatoms before they create a new nucleus or are captured by existing islands. The logarithmic correction term appearing in the denominator is small. Omitting this term one gets

$$L \approx \left(\frac{D}{R}\right)^{\frac{1}{6}} \quad (2.15)$$

So  $L$  depends only on the ratio  $D/R$ . This is due to the fact that the flux is the only quantity introducing time, if there is no re-evaporation and dimers are stable. Thus, the ratio of deposition to diffusion rate determines the mean free diffusion path and the mean island distance attained at saturation.

## 2.4 Growth modes

The classification of three growth modes (see Fig. 2.4) was first introduced by Ernst Bauer in 1958 (Ref. [7]).

Lattice mismatch between substrate and adsorbate has a marked effect on film morphology (Ref. [4]). The strain resulting from lattice mismatch contributes to the interface energy, is a key parameter in determining the growth mode. However, the surface free energies for the substrate and film materials also influence the mode of growth. For heteroepitaxy in general, observed growth modes have been placed in three categories depending on the resulting film morphology (Ref. [8]). These are: (1) Frank van-der-Merwe (FM) or layer-by-layer growth, (2) Volmer-Weber (VW) or 3D island growth and (3) Stranski-Krastanov

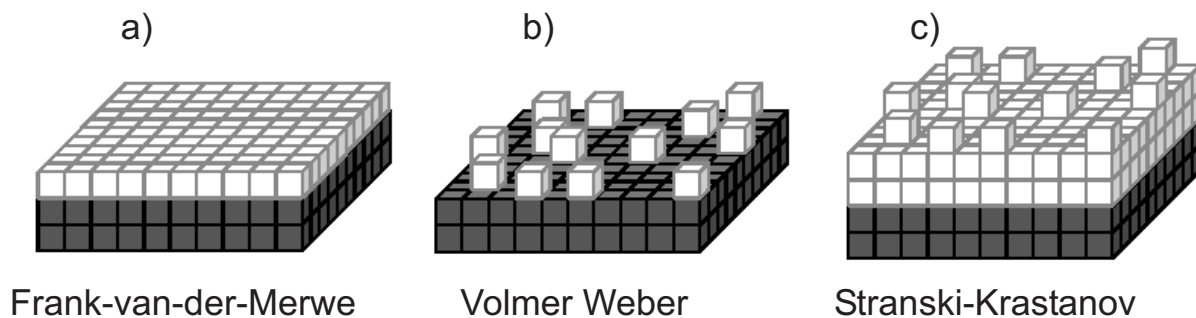


**Figure 2.4:** The growth modes. a) Frank-van-der Merwe (layer-by-layer) growth, b) Volmer-Weber (3D island) growth and c) Stranski-Krastanov (3D island-onwetting-layer) growth.

(SK) or 3D island-on-wetting-layer growth. The interatomic interactions between substrate and film materials are stronger and more attractive than those between the different atomic species within the film material in FM growth, whereas just the opposite is true in VW growth. SK growth occurs for interaction strengths somewhere in the middle. Bauer and van der Merwe (Ref. [9]) have cast the energetics of film growth into a particularly simple form under the assumption of equilibrium between the film components in the gas phase and those in the film surface. In this formalism, layer-by-layer growth of A on B requires that

$$\Delta\gamma = \gamma_A + \gamma_i - \gamma_B \leq 0 \quad (2.16)$$

where  $\gamma_A$  and  $\gamma_B$  are the surface free energies of material A and material B, respectively, and  $\gamma_i$  the interfacial free energy. The latter quantity depends on the strain and the strength of chemical interactions between A and B at the interface. Equation 2.16 says in effect that the sum of the film surface energy and the interface energy must be less than the surface energy of the substrate in order for wetting to occur. Alternatively, it becomes easier for layer-by-layer growth to occur as the surface energy of the substrate increases. Thus, FM growth is expected if equation 2.16 is obeyed. However, the strain energy, which is a term in  $\gamma_i$ , increases linearly with the number of strained layers. At some thickness,  $\gamma_A + \gamma_i$  exceeds  $\gamma_B$  and the growth mode transforms from FM to SK resulting in 3D islands on the 2D wetting layer. Alternatively,  $\gamma_A$  may be sufficiently in excess of  $\gamma_B$  that equation 2.16 is never fulfilled even for a strong attractive interaction between A and B and little strain ( $\gamma_i \leq 0$ ). In this case, 3D islands nucleate from the onset resulting in VW growth. Finally, in the limit of zero lattice mismatch and weak chemical interactions between A and B at the interface ( $\gamma_i \cong 0$ ), the growth mode is determined entirely by the surface free energies of the film and substrate material. An interesting ramification of equation 2.16 is that growing superlattices (A/B/A/B...) that consist of perfectly laminar films and atomically flat interfaces is not likely unless  $\Delta\gamma \cong 0$ . If  $\Delta\gamma \leq 0$  for A on B, then  $\Delta\gamma \geq 0$  for B on A. However, the clever use of surfactants, which have the effect of lowering the surface energy of the high-surface-energy component, can alleviate this problem.

## 2.5 Diffusion limited aggregation

The Diffusion Limited Aggregation (DLA) model was introduced by Witten and Sander (Ref. [10, 11]) and simulates the epitaxial growth at a low deposition rate of impinging particles within a discrete, kinetic model: Fix a seed particle at the origin of some coordinate system. Now introduce another particle at a large distance from the seed, and let it perform a random walk. Ultimately, that second particle will either escape to infinity or contact the seed, to which it will stick irreversibly. Now introduce a third particle into the system and allow it to walk randomly until it either sticks to the two-particle cluster or escapes to infinity. Once it hits the aggregate, it sticks with a certain probability given by the sticking coefficient. The smaller the sticking coefficient, the more dense the aggregate should become (Ref. [12]). The cluster's dendritic structure arises because the faster growing parts of the cluster shield the other parts, which therefore become less accessible to incoming particles. An arriving random walker is far more likely to attach to one of the tips of the cluster than to penetrate deeply into one of the cluster channels without first contacting any surface site. Thus, the tips tend to screen the channels, a process that evidently operates on all length scales. Extending the DLA model to several seed particles (Ref. [13]), the same dendritic island shape is observed. With increasing coverage and island size, the clusters become rounder and denser, but are still separated by channels even at a high coverage (Ref. [14–16]). In Fig. 2.5 after Ref. [12] for a point attractor as nucleation center two aggregates with different sticking coefficients are depicted. It shows that with decreasing sticking coefficients the aggregate becomes more dense.

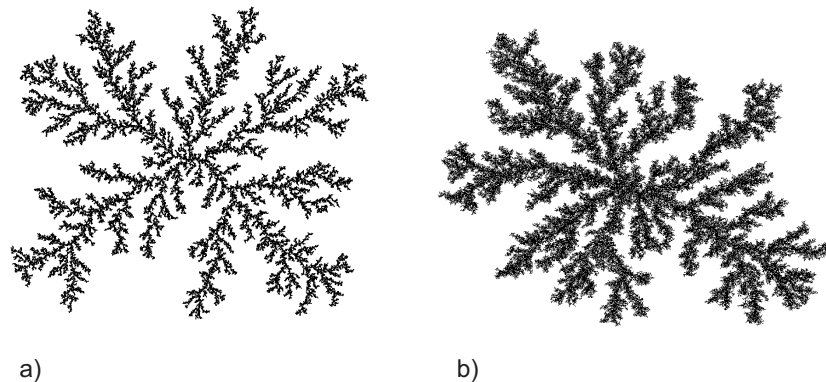


**Figure 2.5:** DLA aggregates for point attractors with sticking coefficient a) 0,2 and b) 0,01.

### 3 Fracture, buckling and delamination of thin films

Thin film fracture is a common phenomenon and it is of special importance in respect to layered materials such as TMDC. The mechanisms leading to defects in thin films are quite complex. Therefore, in this chapter a theoretical description and introduction after Z. Suo et al. is given which addresses the most important points in the underlying mechanisms.

#### 3.1 Origin of stress

As a film grows on a substrate at a fixed temperature,  $T_G$ , a mismatch strain field arises in the film due to, e.g., defects annihilation, epitaxy, phase transition, and new material growing into grain boundaries in the film (Ref. [17, 18]). The film accommodates the mismatch by inelastic and elastic deformation. It is usually difficult to predict from first principles the stress generated in the film during growth. In practice, the growth stress is measured experimentally by using methods such as wafer bending, X-ray diffraction, and luminescence piezospectroscopy [19, 20]. If the substrate is much thicker than the film and both are flat, the stress field developed during film growth is uniform throughout the film, and equally biaxial in the plane of the film. Under these assumptions, the substrate is stress free. After the film is grown, the temperature may be changed from  $T_G$  to a different level  $T$ . The thick substrate acquires a thermal strain, but remains stress free. The film also acquires a thermal strain, which differs from that of the substrate by

$$\varepsilon_T = \int_{T_G}^T (\alpha_f - \alpha_s) dT \quad (3.1)$$

where  $\alpha_f$  and  $\alpha_s$  are the thermal expansion coefficients of the film and the substrate. When the film and the substrate are well bonded, the net in-plane strain in the film must be the same as the thermal strain of the substrate. Consequently, the mismatch strain, equation 3.1, needs to be accommodated by elastic and inelastic deformation in the film. If the film remains elastic during the temperature change, this mismatch strain induces a biaxial stress in the plane of the film,  $\sigma_T$ , given by

$$\sigma_T = \frac{E_f \varepsilon_T}{1 - \nu_f} \quad (3.2)$$

where  $E_f$  is Young's modulus and  $\nu_f$  is the Poisson's ratio of the film. Additional stress can be generated by, e.g., a bending moment applied to the film-substrate composite.

In the case of, e.g., epitaxial growth (Ref. [4]) the lattice match refers to the quantitative comparison of in-plane lattice parameters of the substrate ( $a_{sub}$ ) and the film ( $a_{film}$ ). The lattice mismatch  $f$  can be defined as

$$f = \frac{\Delta a}{a} = \frac{a_{film} - a_{sub}}{a_{sub}} \quad (3.3)$$

where both lattice parameters are in the growth plane. This quantity should be as small as possible in order to reduce strain in the film. If  $a_{film} < (>) a_{sub}$  the film will be in tension (compression) prior to relaxation. Indentation and scratching are other means to generate stress; however, the stress field so generated is complicated. The total stress in the film is

the sum of the growth stress, the thermal stress, and the applied stress.

### 3.2 Crack driving force and crack resistance

Following the Linear Elastic Fracture Mechanics (LEFM), one adopts a crack growth approach. Cracklike flaws are assumed to pre-exist in the film, in the substrate, and on the interface. When the stress in the composite is large enough, one of the flaws will grow. The crack driving force,  $G$ , is the elastic energy reduction associated with the crack advancing per unit area. For a given crack geometry, the crack driving force is calculated by solving an elasticity boundary value problem. The crack resistance,  $\Gamma$ , is the energy needed to advance the crack per unit area. A crack cannot grow when the driving force is below the resistance, and grows when the driving force is equal or larger than the resistance. The crack resistance is measured experimentally for a crack running in the film, in the substrate or on the interface. The three locations have different values of crack resistance, denoted as  $\Gamma_f$ ,  $\Gamma_s$  and  $\Gamma_i$ . The crack resistance also depends on the environment and the crack velocity. For a crack running on the interface, the crack resistance in addition depends on the interfacial chemistry, the interfacial morphology, and the mode mixity. Experimental methods to determine the crack resistance in film-substrate composite are discussed by Ref. [17].

### 3.3 Cracking in a film under tension

If a film is under tension and is brittle, a possible failure mode is cracking in the film. Starting from a flaw in the film, a crack propagates from the surface through the film. For the time being, the crack is assumed to arrest at the interface, leaving the interface and the substrate intact. The crack, however, propagates laterally in the film, uninhibited until it meets a film edge or another crack. The lateral crack length can be many times the film thickness. Such a crack is known as a channel crack. Because the film may have many pre-existing flaws, under a large stress, many channel cracks can form.

The complex morphology of a cracked film is difficult to quantify. Consequently, attention is focused on the formation of the first channel crack, originated from the most distinctive pre-existing flaw in the film. For the time being, both the film and the substrate are assumed to be elastic. Let  $h$  be the film thickness,  $\sigma$  the stress in the film, and  $a$  the size of the pre-existing crack in the film. Fig. 3.1 distinguishes two cases.

In case A, the pre-existing crack size is much smaller than the film thickness,  $a \ll h$ , so that the crack front runs in the direction of the interface and laterally in the film. The crack driving force is given by

$$G = 3.94 \frac{(1 - \nu_f^2) \sigma^2 a}{E_f} \quad (3.4)$$

This expression comes from an edge crack of depth  $a$  in an infinite homogeneous material. The form of the equation applies to cracks of other shapes, with the numerical coefficient being shape dependent [21]. The pre-existing crack grows when the crack driving force equals the crack resistance, namely,



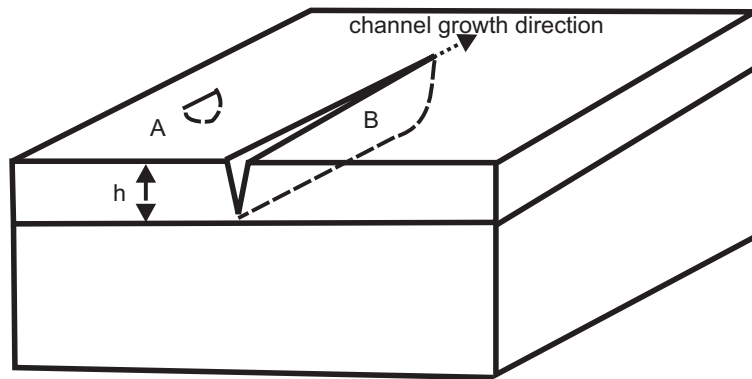


**Figure 3.1:** Case A: The initial flaw size is much smaller than the film thickness. Case B: The initial flaw size is comparable to the film thickness.

$$\Gamma_f = G = 3.94 \frac{(1 - \nu_f^2) \sigma^2 a}{E_f} \quad (3.5)$$

Once started, the crack will grow and form a channel. In equation 3.5, the crack resistance, Young's modulus, and Poisson's ratio are all material constants. Consequently, the critical stress needed to form a channel crack varies with the size of the pre-existing flaw. Flaws are generated during film growth or subsequent use, and measuring the flaw sizes on a routine basis is impractical.

The above consideration leads us to examine case B illustrated in Fig. 3.1. When the pre-existing crack size is comparable to the film thickness,  $a \approx h$ , the crack can only propagate laterally in the film. When the lateral crack length exceeds several times the film thickness, the driving force at the growing front attains a steady-state value, given by [22]

$$G = \beta \frac{(1 - \nu_f^2) \sigma^2 a}{E_f} \quad (3.6)$$

The dimensionless number  $\beta$  depends on the elastic constants of the film and the substrate. When the substrate is stiffer than the film,  $\beta$  is between 1 to 2. When the substrate is much more compliant than the film,  $\beta$  can be very large.

For a given film-substrate composite, equation 3.6 gives the largest driving force for flaws of any size to form a channel. Consequently, regardless of the details of the initial flaws, no channel can form if this driving force is below the crack resistance:

$$\beta \frac{(1 - \nu_f^2) \sigma^2 a}{E_f} < \Gamma_f \quad (3.7)$$

When the condition is satisfied, no channel can form. The critical value for the crack formation depends on the film thickness, rather than on the pre-existing flaw size (Ref. [23]). This mathematical description shows that either no crack forms or a crack forms through the hole film. There is no intermediate state.

### 3.4 Debonding of a film under compression

Similar to thin film fracture, debonding of thin films is also of major interest in respect to layered materials. Just as thin films can debond buckling of several layers could occur. When a film (or layer) is under compression, it may still debond from the substrate, but will do so in quite different manners from a film under tension. To appreciate basic behaviors, first assume the plane strain conditions. The plane strain condition model reduces a three dimensional strain problem to a two dimensional one.

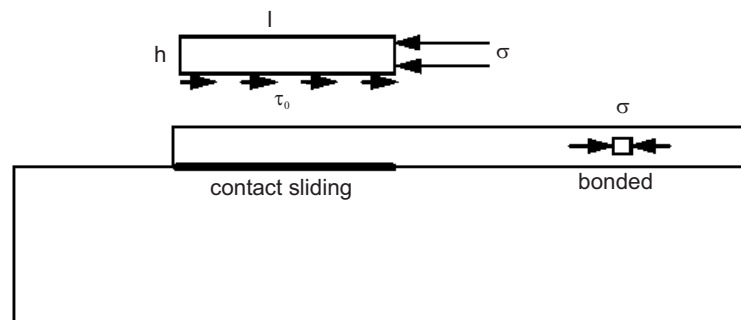


**Figure 3.2:** A debond crack initiated from an edge of the film

Fig. 3.2 illustrates a debond crack initiated from an edge of a film under compression. The debonded film remains in contact with the substrate. This can be understood as follows. If the two crack faces were not in contact, they would be traction free.

The residual stress in the film is now compressive.

The two crack faces may slide relative to each other against friction. Such a crack will stop after a certain length. Assume that the sliding friction has a constant value,  $\tau_0$ .

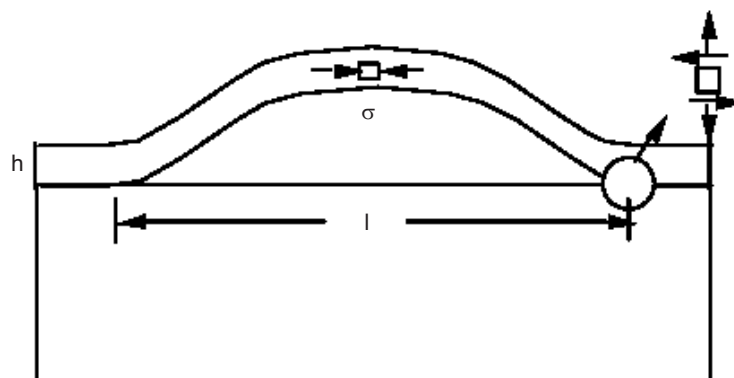


**Figure 3.3:** After the unbonded film buckles, stress arises on the interface.

When the film is perfectly bonded with the substrate, the film is under compression, but the interface is stress free. Even when an area underneath the film is unbonded, as long as the film remains flat, there is no stress acting on the interface. However, a large enough area of unbonded film may buckle (Fig. 3.3). After buckling, at the interface at the buckle front both normal and shear stresses develop, which may motivate the unbonded area to

grow like a crack. Three aspects need to be considered: pre-buckling development of an unbonded area, buckling of the unbonded film, and post-buckling growth of the unbonded area. Despite their practical significance, pre-buckling processes are little understood beyond a few qualitative observations. A contaminated substrate may lead to large unbonded areas after the film is grown. Voids are sometimes seen on the interface. Further research into the pre-buckling processes holds a key to averting failure of films under compression. By contrast, film buckling is well understood. If the film has a sufficiently large unbonded area, the film above this area buckles. The critical unbonded length for buckling,  $l_c$ , is given by

$$l_c = \frac{\pi h}{\sqrt{3(1-\nu_f^2)}} \left[ \frac{E_f}{-\sigma} \right]^{\frac{1}{2}} \quad (3.8)$$

with the film thickness  $h$ .

It can be seen as criteria; above the critical value  $l_c$  a sudden change of the film (layer) morphology occurs.

Equation 3.8 applies to an unbonded area of any shape, with the numerical coefficient being shape dependent. Taking  $-\sigma/E = 10^{-2}$ , which is quite a large elastic strain, equation 3.8 yields  $l_c \approx 20h$ . Such a large unbonded area is not usually produced in film growth. Several post buckling behaviors have been studied (Ref. [22, 24]). A large unbonded area can buckle into complicated shapes.

A debond buckle, however, can grow like a tunnel underneath the film, uninhibited laterally until it approaches another tunnel or an edge of the film. Initiated from isolated unbonded areas, the tunnels can cause the entire film to disintegrate. Further aspects like substrate cracking can be reviewed in Ref. [25, 26]. The role of inelastic deformation is discussed in Ref. [27], [28–30].

## 4 The substrates: Transition metal dichalcogenides

The layered transition metal dichalcogenides (TMDC) crystals (Fig. 4.1) used for the experiments were grown by CVT (chemical vapor transport, chapter 5.1) and possess the stacking order XTX-XTX-XTX (X: chalcogenide atoms like S, Se, Te; T: transition metal like Ta, W, V etc.). They are built up by three atomic sandwich layers, which are stacked on top of each other. Depending on their components the crystals are metallic or semi-conducting. Only weak van der Waals forces act between neighboring triple layers, so it is easily possible to cleave such crystals along a triple layer. Substrates prepared in this way often possess a surface that is atomically flat over hundreds of  $\mu\text{m}^2$  without any structural defects. The only defects that can eventually be found are step edges, separated by several micrometers.

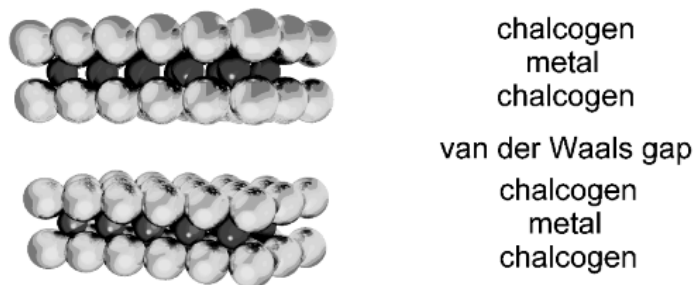


**Figure 4.1:** Layered structure of transition metal dichalcogenides.

**geometric structure** All transition metal dichalcogenides are built up in a similar way but they differ in their crystallographic description. Shown in Fig. 4.2 a) and b) the transition metal atom can be coordinated by the six nearest chalcogen atoms in two different ways: In the 1T structure (symmorphic space group  $P\bar{3}m1$ ) the chalcogen atoms form a nearly regular octahedron. In this type the unit cell contains only one sandwich layer in the  $c$  direction. The unit cell of the 2H structure (non-symmorphic space group  $P6_3/mmc$ ) is extended over two sandwich layers. In one layer the chalcogen atoms are located above each other. The layer is rotated by  $60^\circ$  with respect to the neighboring layers. Different stacking sequences of the layers result in various polymorphic types such as 1T,  $2H_a$ ,  $2H_b$ , 3R etc. The number in front of the letter denotes the number of layers one unit cell contains.

**electronic structure** Wilson and Yoffe [32] offered a general scheme to describe the electronic structure of transition metal dichalcogenides. According to this scheme the  $s$ - and  $p$ - orbitals of the chalcogen atoms are divided into unoccupied ( $\sigma^*$ ) and occupied ( $\sigma$ ) band states. The states are separated by an energy gap of several eV. The metal derived  $d$  states are located within this bonding-antibonding energy gap. They are split into a twofold degenerate level  $e_g$  associated with the  $d_{xz}$  and  $d_{yz}$  orbitals and into a threefold degenerate level  $t_{2g}$  associated with the  $d_{z^2}$ ,  $d_{x^2-y^2}$  and  $d_{xy}$  orbitals. The degree of filling of  $d$  bands largely determines the electrical, magnetic and optical character of the various compounds. A simple ionic picture helps to understand this: Two electrons are transferred from the transition metal to the chalcogen atoms where the  $p$  orbitals are then completely filled. The remaining electrons can occupy the  $d_{z^2}$  band of the metal to a certain degree: The

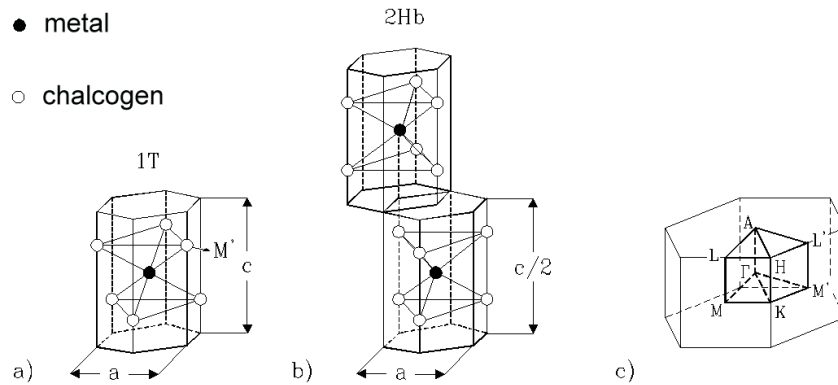


**Figure 4.2:** a) Unit cells of the 1T and b) the 2H<sub>b</sub> polytype and c) the corresponding Brillouin zone, from [31].

transition metals of group IVb are in a  $d^0$  configuration, the  $d_{z^2}$  band stays unoccupied, the respective TMDC are generally semiconductors. In TMDC with transition metals from group Vb, the  $d_{z^2}$  band is half filled resulting in metallic behaviour. Due to the completely filled  $d_{z^2}$  band of group VI transition metals, the respective TMDC show semiconducting properties.

The electronic structure is directly related to the geometric structure and vice versa. This can be seen by the effect that the coordination of chalcogen atoms changes from octahedral for group IVb metals to trigonal prismatic for group VIb metals. (Group Vb TMDC exist in both coordinations.) In the latter case the  $d_{z^2}$  band is split off from the other d bands and lowered in energy. This energy gain compensates in trigonal prismatic TMDC the energy loss due to a higher Madelung energy in this coordination.

**adsorption or intercalation?** The possibility to intercalate foreign atoms or molecules into the van der Waals gap between the host layers is of particular interest. In view of practical applications this method of modifying the physical properties and in particular the electronic structure was widely studied and discussed. It is for instance possible to achieve semiconductor-to-metal transitions (or vice versa) or to turn a normal conductor into a superconductor. The occurring changes are ascribed to a charge transfer from the introduced species to the host lattice. This is also regarded as the driving force of the intercalation. They are simply described in terms of the rigid band model (RBM), in which it is assumed that the band structure of the host material is not changed except for the filling of the conduction band due to the charge transfer. Going into more detail it is evident that the rigid band model is not strictly applicable. Due to a decoupling of the host layers other changes going beyond the RBM occur: In general, the perpendicular dispersion of electronic states is markedly reduced and band widths and band gaps are significantly altered. These changes are already taking place at an early stage of intercalation. The most important categories of intercalants are alkali metals and other simple metals like copper and silver [33], 3d transition metals [34] and organic molecules like ammonia and hydrazine [35]. The intercalation of transition metal dichalcogenides with alkali metals can be achieved by different methods, e. g. immersion in alkali-ammonia solutions, electrolysis of a solution of an appropriate metal salt or *in situ* through alkali-metal deposition in ultra

high vacuum onto a clean surface. Although the latter method has the great advantage that the surface remains more or less intact it is a complex process which is not well understood.

## 5 Crystal growth and preparation

The quality of experimental results and therefrom derived conclusions are certainly strongly dependent on the quality of the underlying substrates. In order to achieve these kind of samples appropriate techniques for crystal growth preparation are necessary. One possibility to grow such crystals is the chemical vapor transport.

### 5.1 Chemical vapor transport

Chemical Vapor Transport (CVT) represents the standard technique to grow crystalline bulk transition metal dichalcogenides (TMDC). All of the single crystals investigated in this thesis were grown by CVT. The principle of CVT is shown in Fig. 5.1.

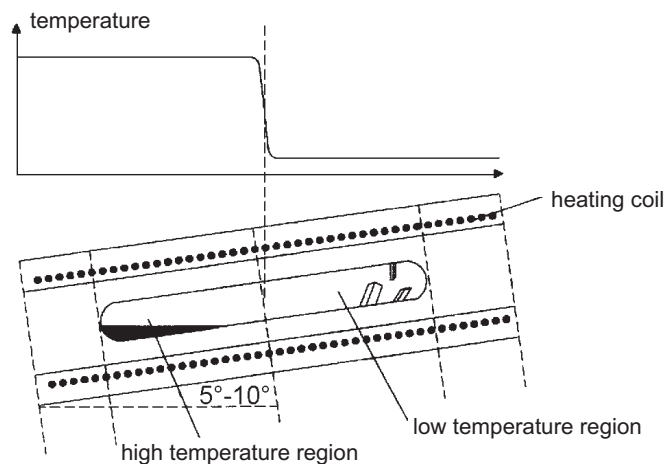


**Figure 5.1:** Temperature gradient and furnace for the chemical vapor transport. In the high temperature region the pure components evaporate and grow as a single crystal in the low temperature region.

A stoichiometric amount of the pure elements is introduced into a quartz tube with iodine ( $I_2$ ). The iodine acts as transport agent. The tube is evacuated and sealed. Then, the tube is inserted into a four-zone furnace. In the furnace a temperature gradient is established with the source zone on the high temperature side and the growth zone on the low temperature side of the tube. Within 26 days single crystals of the respective TMDC sample are grown after the chemical formula:



with  $T = V, Ti, W, Ta, Hf$  and  $X = S, Se, Te$ .

Crystals grown by CVT the process possess a high stacking order and purity.

### 5.2 Sample preparation

It is very important to avoid contamination of the crystal surfaces by air or dust particles. Therefore the crystals can be cleaved in UHV by removing a cleavage bar, fixed on top

of the crystals with a two component UHV capable silver glue. After the cleavage, the crystal can be transferred into the sample holder of the preparation chamber by a magnetic transfer tube.

Fig. 5.2 shows how the proper vapor deposition takes place.

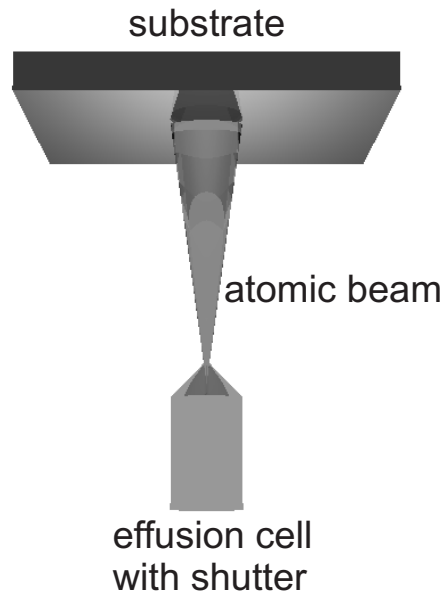


**Figure 5.2:** Basic principle of thermal evaporation of metal onto a substrate.

A thermal effusion cell evaporates a high-purity atomic beam at a certain evaporation rate. The atomic beam is directed to the sample surface. The shutter of the effusion cell ensures an exact timing of the preparation by its opened or closed position. Thus, it is possible to deposit on a substrate material with a well defined film thickness.



## 6 Experimental setup

### 6.1 Scanning tunneling microscopy

Since 1981, when the first successful experiments were performed by G. Binnig, H. Rohrer and coworkers (Ref. [36]), the scanning tunneling microscope (STM) has evolved as the most powerful tool for the investigation of the local geometric and electronic structure of surfaces in real space. Only five years later Binnig and Rohrer received the Nobel Price in physics.

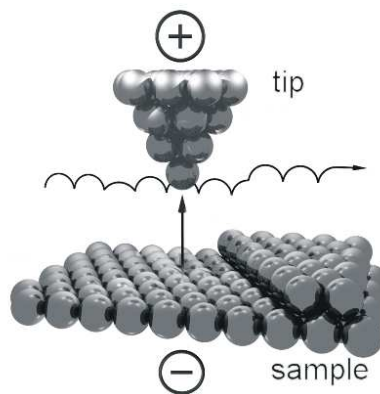


**Figure 6.1:** Principle set up of an STM experiment. A voltage is applied between the sample and the tip. When the distance between them is small enough, electrons can tunnel from the sample to the tip or vice versa (from [37]).

The principle of scanning tunneling microscopy is depicted in Fig. 6.1. A voltage  $U_g$  is applied between a thin metal tip (here: tungsten) and the sample. The tip is approached very closely to a distance of only a few Å to the sample surface. When the distance is small enough that the wave functions of the tip and the sample overlap significantly, the current  $I_t$  arising from electrons that tunnel between tip and sample can be measured:

$$I_t \propto e^{-2\kappa d} \quad (6.1)$$

The quantum mechanical tunneling effect is strongly dependent on the distance  $d$  between the tip and the sample surface ( $\kappa$  is a constant depending on the height of the potential barrier) [38]. By scanning the tip over a defined area of the surface it is thus possible to receive detailed information about the surface topography. One can distinguish between two standard modes of using the STM: The *constant current mode* uses an electronic feedback loop to keep the tunneling current constant by moving the tip vertically to the surface. Hence, the tip follows a contour line of constant local density of states which offers information about the surface morphology. In the *constant height mode* the feedback loop is switched off so that the tip remains at a constant height above the sample and the tunneling current is measured which contains information about the local density of states (LDOS) of the sample surface.

## 6.2 Scanning electron microscopy

Electron microscopes were developed due to the fact that light microscopes are limited by the physics of light to 500x or 1000x magnification and a resolution of 0.2 micrometers. In the early 1930's this theoretical borderline had been reached and there was a scientific desire to discern the fine details of the interior structures of organic cells (nucleus, mitochondria...etc.). This required 10,000x plus magnification which was not possible using light microscopes. The Transmission Electron Microscope (TEM) was the first type of Electron Microscope to be developed and is patterned exactly on the Light Transmission Microscope except that a focused beam of electrons is used instead of light to *see through* the specimen. It was developed by Max Knoll and Ernst Ruska in Germany in 1931. The first non-commercial Scanning Electron Microscope (SEM) debuted in 1942. The first commercial instruments came on the market around 1965. Its late development was due to the sophisticated electronics needed for scanning the beam of electrons across the sample.

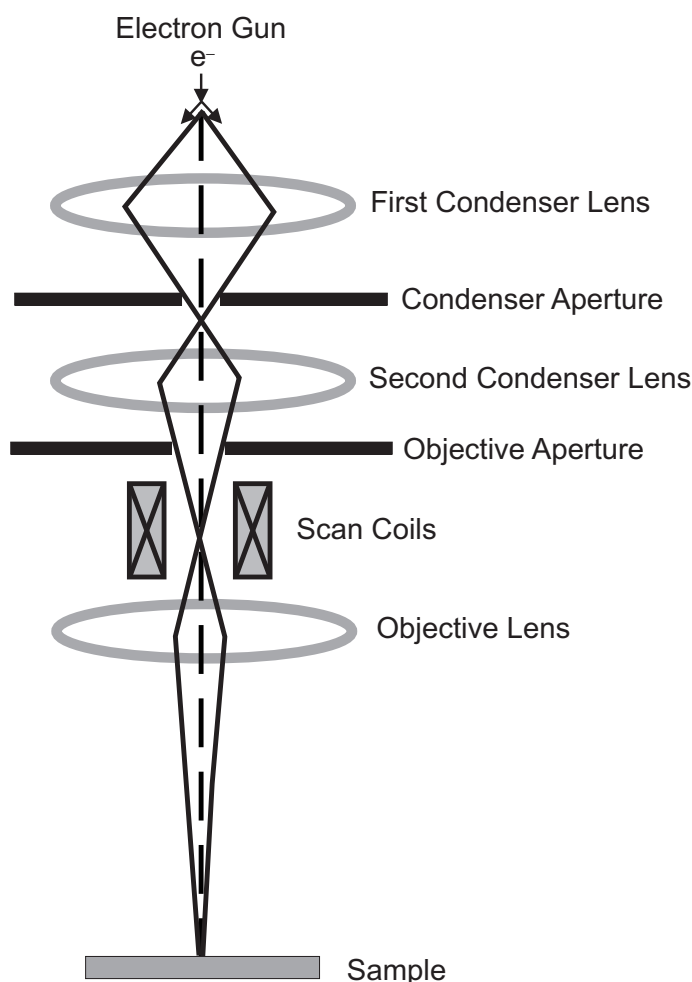


**Figure 6.2:** The principle arrangement of condenser lenses, apertures, scan coils and the resulting path of the electron beam of an SEM.

The electron gun in a scanning electron microscope is the source for the electron beam used to probe the sample. The gun consists of a tungsten filament cathode or a  $LaB_6$  cathode, a Wehnelt cylinder and an anode. The electrons can be generated by thermal-

or field emission and are then accelerated to the anode by a defined acceleration voltage. The generated electron beam consists of monochromatic electrons and its path is sketched in Fig. 6.2. This beam is condensed by the first condenser lens. This lens is used to form the beam and limit the current in the beam. It works in conjunction with the condenser aperture to eliminate the high-angle electrons from the beam. The second condenser lens forms the electrons into a thin, tight, coherent beam. A user selectable objective aperture further eliminates high-angle electrons from the beam. A set of coils then scans or sweeps the beam in a grid fashion, dwelling on points for a period of time determined by the scan speed (usually in the microsecond range). The final lens, the objective lens, focuses the scanning beam onto the desired part of the specimen. When the beam strikes the sample (and dwells for a few microseconds) interactions occur inside the sample and are detected with various instruments. Before the beam moves to its next dwell point these instruments count the number of interactions and display a pixel on a CRT (cathode ray tube) whose intensity is determined by this number (the more reactions the brighter the pixel). This process is repeated until the grid scan is finished.

The interaction between the electron beam and the specimen is the basis of electron microscopy. The energetic electrons in the microscope strike the sample and various reactions can occur as shown below in Fig. 6.3. The reactions noted on the top side of the diagram are utilized when examining thick or bulk specimens (SEM) while the reactions on the bottom side are those examined in thin or foil specimens (TEM).

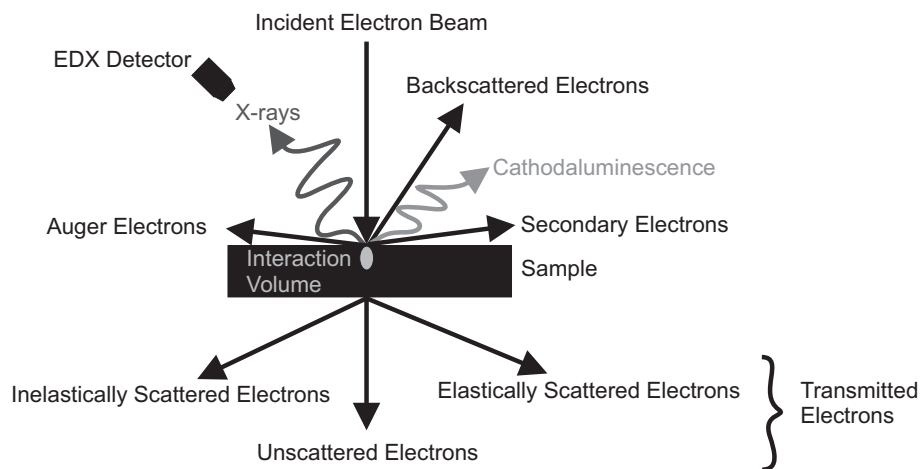


**Figure 6.3:** The possible interactions of an incident electron beam and a sample.

The interaction volume depends strongly on the applied acceleration voltage and the atomic number(s) of the element(s) the specimen consists of. The penetration depth of the electrons increases with increasing acceleration voltage and decreases with increasing atomic number. One differentiates between bulk specimen and thin specimen interactions.

## Bulk specimen interactions

Backscattered electrons:

They are caused by an incident electron colliding with an atom in the specimen which is positioned in the normal of the incident electron beam. The incident electron is then scattered backward by  $180^\circ$ .

The generation of backscattered electrons varies directly with the specimen's atomic number. This differing rate causes higher atomic number elements to appear brighter than lower atomic number elements. This interaction is utilized to distinguish parts of the specimen that have a different average atomic number.

Secondary electrons:

An incident electron that passes near an atom in the specimen can impart some of its energy to a lower energy electron (usually in the K-shell). This causes a slight energy loss and path change in the incident electron and the excitation of the electron in the specimen atom. This excited electron then leaves the atom with a very small kinetic energy ( $\approx 5\text{eV}$ ) and is then termed a *secondary electron*. Each incident electron can produce several secondary electrons (see Fig. 6.4).

Generation of secondary electrons is related strongly to the topography of the specimen. Due to their low energy only secondaries that are very near to the surface ( $\leq 10\text{ nm}$ ) can leave the sample and be detected. Any changes in topography in the sample that are larger than this sampling depth will change the yield of secondaries due to collection efficiencies. Collection of these electrons is aided by using a collector in conjunction with the secondary electron detector. The collector is a grid or mesh with a  $+100\text{ V}$  potential applied to it which is placed in front of the detector, attracting the negatively charged secondary electrons which then pass through the grid-holes and into the detector.

Auger electrons:

Since a lower (usually K-shell) electron was emitted from the atom during the secondary electron process an inner (lower energy) shell now has a vacancy. A higher energy electron from the same atom can drop to a lower energy level, filling the vacancy. This creates an energy surplus in the atom which can be compensated by emitting an outer (lower energy) electron: an Auger Electron.

Auger Electrons have a characteristic energy, unique to each element which it was emitted from. These electrons are collected and sorted according to energy to give compositional information about the specimen.

X-rays:

X-rays are caused after a secondary electron is produced. A lower (usually K-shell) electron was emitted from the atom during the secondary electron process and an inner (lower energy) shell now has a vacancy. A higher energy electron can drop into the lower energy shell, filling the vacancy. It emits energy, usually X-rays, to balance the total energy of the atom (see Fig. 6.4). The X-rays caused by the electron transitions can be used for energy

dispersive X-ray analysis described in 6.3.

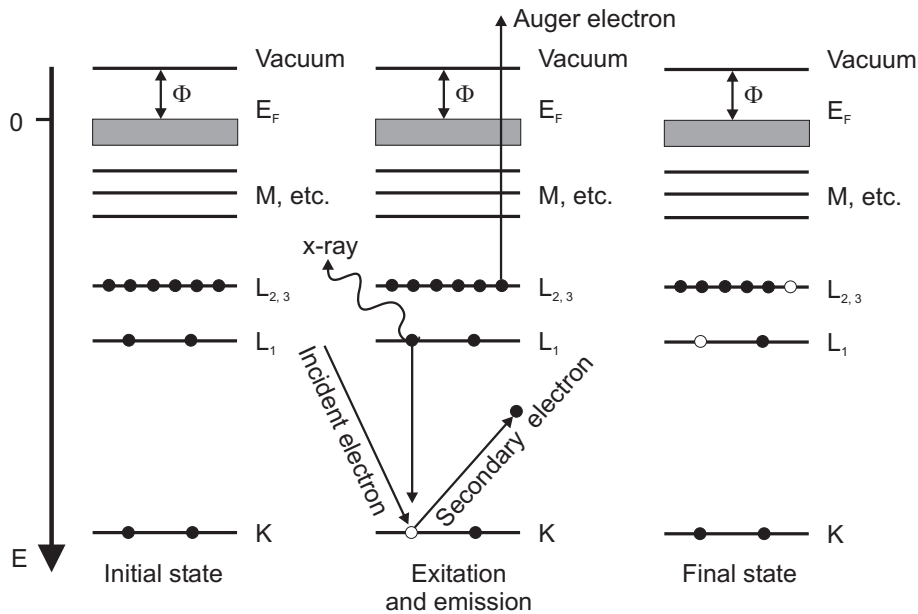


**Figure 6.4:** Schematic energy diagram to illustrate the generation of secondary electrons, X-rays and Auger electrons by an incident electron.

### Thin specimen interactions

Unscattered electrons:

Incident electrons which are transmitted through the thin specimen without any interaction inside the specimen. The transmission of unscattered electrons is inversely proportional to the specimen thickness. Areas of the specimen that are thicker will have fewer transmitted unscattered electrons and so will appear darker, conversely the thinner areas will have more electrons transmitted and thus will appear lighter.

Elastically scattered electrons:

Incident electrons that are scattered (deflected from their original path) by atoms in the specimen in an elastic process lose no energy. These scattered electrons are then transmitted through the remaining portions of the specimen. All electrons follow Bragg's Law and thus are scattered according to

$$n\lambda = 2d \sin \alpha \quad (6.2)$$

where  $n$  is the order of scattering,  $\lambda$  the wavelength of the incident electrons,  $d$  the space between the atoms and  $\alpha$  the angle of scattering.

All incident electrons have the same energy (thus wavelength) and enter the specimen normal to its surface. All incidents that are scattered by atoms with the same distance between each other will be scattered by the same angle. These scattered electrons can be collected using magnetic lenses to form a pattern of spots on a screen or detector. Each spot of the

pattern correspond to a specific atomic spacing (a plane). This pattern can then yield information about the orientation, atomic arrangements and phases present in the area being examined.

Inelastically scattered electrons:

The incident electrons that interact inelastically with specimen atoms lose energy during the interaction. These electrons are then transmitted through the rest of the specimen. Inelastically scattered electrons can be utilized in two ways. Electron Energy Loss Spectroscopy (EELS) is based on the inelastic loss of energy by the incident electrons which is characteristic of the elements that were interacted with. These energies are unique to each bonding state of each element and thus can be used to extract both compositional and bonding (i.e. oxidation state) information on the specimen region.

### **6.3 Energy dispersive X-ray analysis**

X-rays emitted from the atoms have a characteristic energy distribution which is unique to the element from which it is originated. These signals are collected and sorted according to the energy by a detector, giving a spectra of detected elements.

#### **Element line scans by using EDX**

The EDX line scan modus allows to perform element specific analysis along a certain direction. The electron beam scans along a user defined direction and a detector collects the X-rays emitted by the elements. In order to get a required signal intensity for element analysis the acceleration energy of the electrons has to be three times higher than the X-ray energy emitted by the electron transition of the relevant elements. The modus allows to detect signals of different elements and its spatial resolution is in the range of 10 to 100 nm, depending on the detected element.

## 6.4 Atomic force microscopy

After the invention of the STM (see chapter 6.1) the atomic force microscope (AFM) was the further development by G. Binnig, H. Rohrer and coworkers for insulating materials. The functionality is based on the interatomic force between a thin tip and the surface atoms, shown in Fig. 6.5. By scanning the tip over a defined area of the surface it is thus possible to receive detailed information about the surface topography. One differentiates generally between two operation modes where different force ratios prevail. The AFM can either be operated in contact mode where repulsive coulomb forces dominate or in non contact mode where attractive van der Waals forces prevail. The first case is termed static atomic force microscopy and the latter dynamic atomic force microscopy.

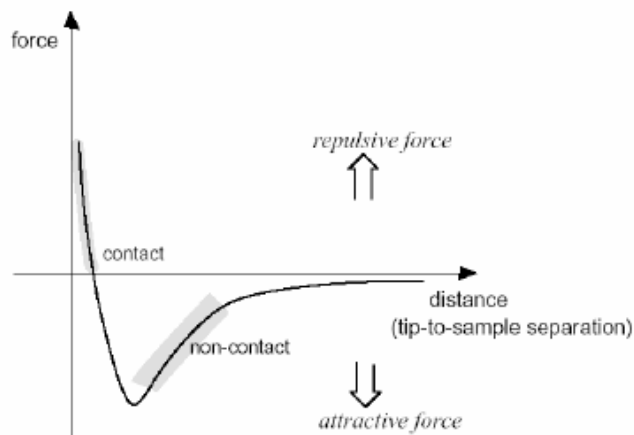


**Figure 6.5:** Dependence of the interatomic force between tip and sample atoms and its distance.

In contact mode AFM, depicted in Fig. 6.6, interatomic van der Waals forces become repulsive and coulomb forces prevail as the AFM tip comes in close contact with the sample surface. The force exerted between the tip and the sample in contact mode is in the order of about 0.1...1000 nN. Under ambient conditions two other forces besides van der Waals interactions are also generally present. These forces include the capillary force from a thin layer of water in the atmosphere, and the mechanical force from the cantilever itself. The capillary force is due to the fact that water can wet the area around the tip, causing the AFM tip to stick to the sample surface. The magnitude of the capillary force varies with the distance between the tip and the sample. The mechanical force  $F$  resulting from the cantilever is similar to the force of a compressed spring and its magnitude and sign (repulsive or attractive) is dependent on the cantilever deflection  $\Delta z$  and the cantilever spring constant  $k_c$ . It can be described by Hooke's law

$$\Delta z = \frac{\Delta F}{k_c} \quad (6.3)$$

with the root-mean-square amplitude deviation  $(\Delta z)_{rms}$  of the cantilever caused by thermal vibrations:

$$(\Delta z)_{rms} = \sqrt{\frac{k_B T}{k_c}} \quad (6.4)$$

where  $T$  is the temperature and  $k_B$  the Boltzmann constant.

The deflection of the cantilever is measured by a deflection sensor. Therefore, a laser beam is focused on top of the cantilever. The reflection of the laser is detected by photodiodes generating a photo voltage. The change of the measured photo signal is a rate for the cantilever deflection and by monitoring these changes an image representing the surface topography can be obtained. Consequently, in contact mode AFM, the repulsive van der Waals forces and coulomb forces arising for the AFM tip to sample interaction must balance the sum of the forces arising from the capillary force plus the mechanical force from the cantilever.

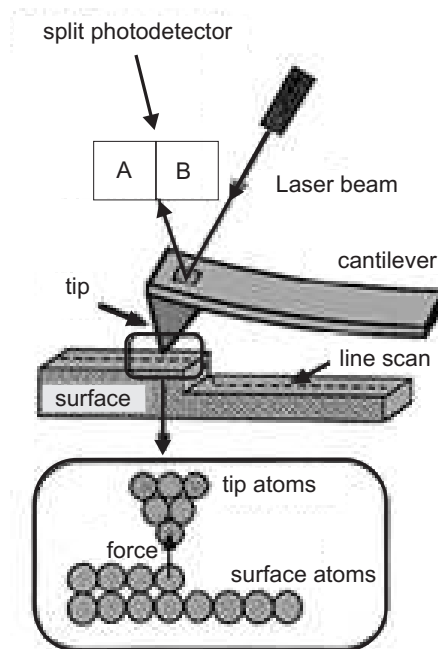


**Figure 6.6:** The principle setup of the contact mode. The cantilever is deflected by interatomic forces. A photodetector measures the cantilever deflection.

The thin layer of water present on many surfaces in air exerts an attractive capillary force and holds the tip in contact with the surface. Thus, when the scanner pulls the tip away from the surface, the cantilever bends strongly towards the surface and the scanner has to retract further so that the tip can snap off the surface. The cantilever returns to its original unbent status as the scanner moves the tip away from the surface beyond the snap-out point.

Contact mode AFM is unfavorable for samples that are either weakly bound or soft, because the tip can simply move or damage surface features. The resulting images are generally not highly resolved. AC mode AFM, which operates in the intermittent contact regime or in the non-contact regime, solves this problem.

In AC mode the cantilever with the mass  $m$  oscillates near its resonant frequency  $\omega_0$  given by the equation



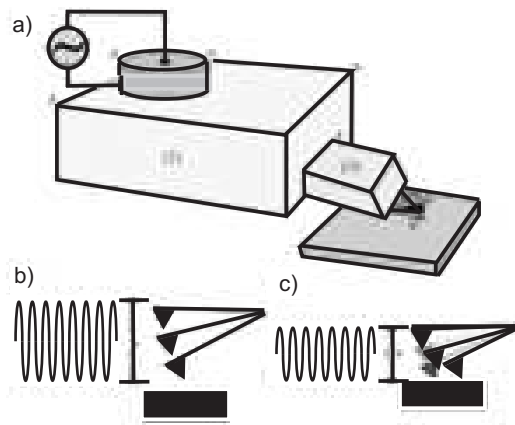


**Figure 6.7:** Acoustic AC mode: a) a transducer attached to a cantilever housing is used to excite a cantilever into oscillation; b) the amplitude of oscillation when the tip is far from the surface; c) reduced amplitude as the tip approaches the surface.

$$\omega_0 = \sqrt{\frac{k_c}{m}} \quad (6.5)$$

AC mode AFM can be classified into two categories, intermittent contact mode and non contact mode.

In the intermittent contact mode the tip is closer to the sample and the the amplitude of the oscillation is bigger than in the non contact mode. The interaction between the tip and the sample is predominately vertical, thus negligible lateral forces are encountered. Consequently, AC mode AFM does not suffer from the tip or sample degradation effects that are sometimes observed after many scans in contact mode AFM, and it is a technique for imaging soft samples. In AC mode, tip-sample interactions cause changes in amplitude, phase and the resonant frequency of the oscillating cantilever. The spatial variation of the change can be presented in height (topography) or interaction (amplitude or phase) images that can be collected simultaneously. The system monitors the resonant frequency or amplitude of the cantilever and keeps it constant by a feedback loop that moves the scanner up and down. The motion of the scanner at each probe location is used to generate a topographic data set. The amplitude change at each probe location forms the amplitude image. The phase data is the result of the phase lag between the AC drive input and the cantilever oscillation output at each probe location.

There are two ways to drive the cantilever into oscillation. One way is accomplished by indirect vibration, in which the cantilever is excited by high frequency acoustic vibration from a piezoelectric transducer attached to the cantilever holder (see figure 6.7). This is called the Acoustic AC mode (AAC). Another, more favored method is a direct vibration method where the cantilever is excited directly without having to vibrate the cantilever housing or other parts. This is called Magnetic AC mode (MAC mode). To achieve MAC mode imaging, a cantilever coated with a magnetic material is driven into oscillation by an AC magnetic field generated by a solenoid positioned close to the cantilever housing. The result of MAC mode is a gentle, clean cantilever response that has no spurious background signals like other AC modes can have. MAC Mode has even greater advantages when the

cantilever is vibrated in liquid. For each mode the lateral resolution is limited by the tip geometry. Broad AFM tips can not resolve structures (defects, dips, clusters etc.) smaller than the tip diameter as depicted in Fig. 6.8. One has to concern this when scanning surfaces with small structures.

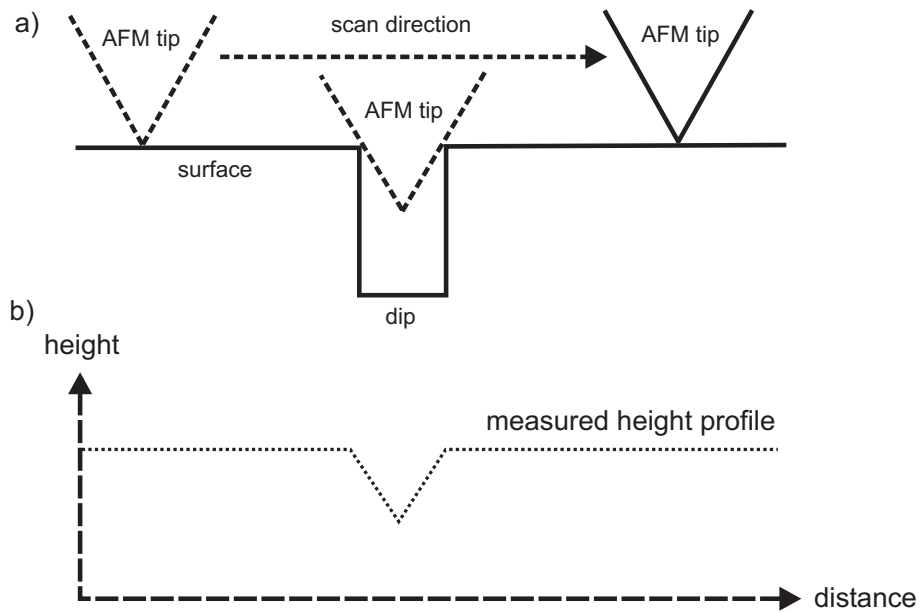


**Figure 6.8:** a) Schematic illustration of an AFM tip scanning over a surface with a dip.  
b) The measured height profile of the surface.

## 6.5 The UHV deposition system

In order to avoid effects by air contamination e.g. of the unprepared crystal substrates it was necessary to construct and realize a UHV deposition system, sketched in Fig. 6.9. The system allows generally to prepare samples under ultra high vacuum conditions.

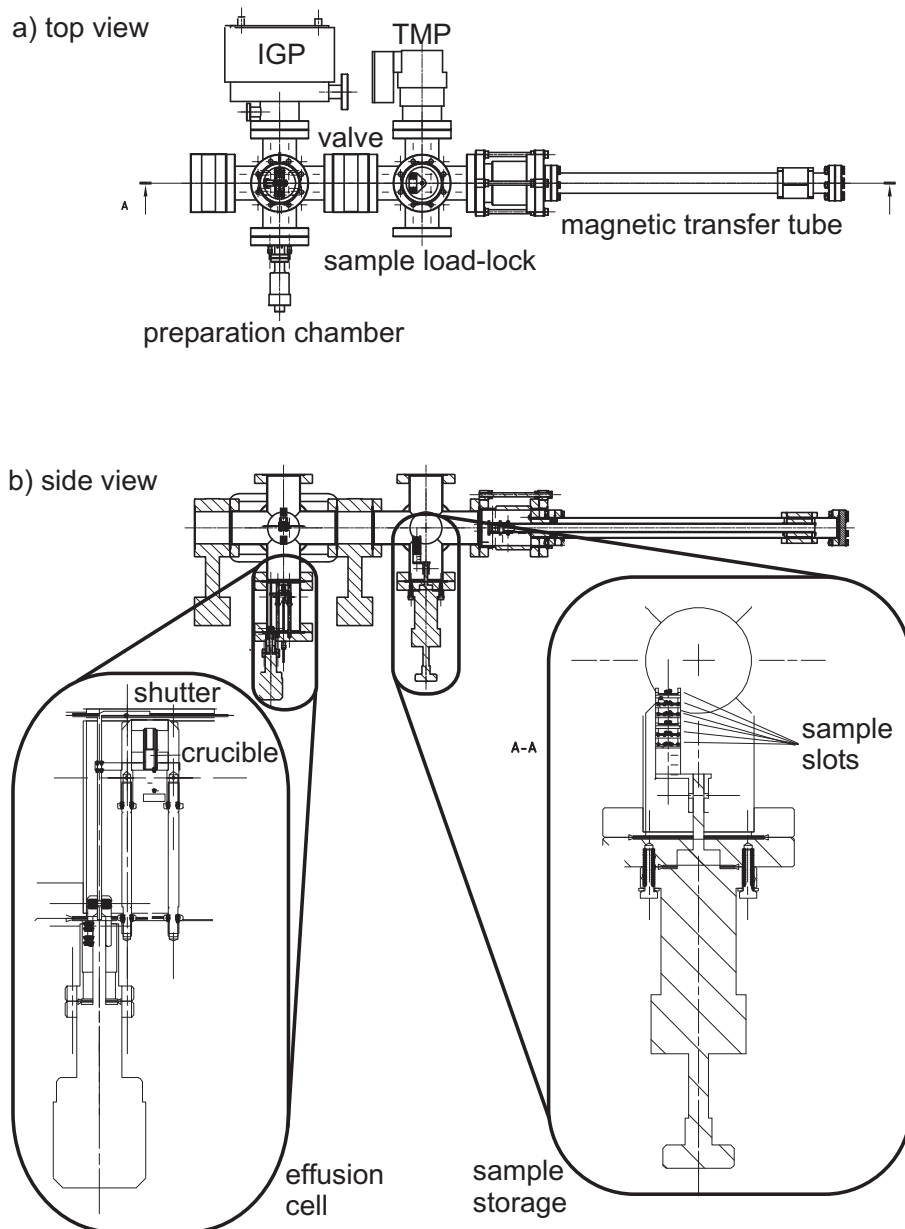


**Figure 6.9:** a) Top view of the system with the preparation chamber and the sample load-lock, separated by a valve. The samples can be transferred by a magnetic transfer tube. b) Side view of the UHV deposition system with scaled up effusion cell and sample storage.

The system consists of a sample load-lock and a preparation chamber with a thermal effusion cell. The chambers can be separated by a valve. The vacuum is generated by a turbo molecular pump (TMP) and an ion getter pump (IGP). A magnetic transfer system

is used to change the samples.

The sample load-lock is equipped with a sample storage which possesses slots for six sample holders.

It is possible to assemble different sample holders in the preparation chamber. There were two different sample holder in use, one for cooling down and one for heating up the substrate (sample). The temperature of the samples can be measured by a thermocouple. Depending on the assembled sample holder the substrate (sample) can be cooled down to  $-100^{\circ}\text{C}$  or heated up to  $400^{\circ}\text{C}$ . So the effect of the substrate (sample) temperature on the growth behavior of deposited material can be studied. After each preparation, the sample can be removed by the magnetic transfer tube, stored in the sample load-lock and the next sample can be prepared under the same conditions without leaving the UHV. The whole system can be baked out at a temperature of  $T_{system} \approx 120^{\circ}\text{C}$  and reaches a base pressure in the range of  $p_{system} \approx 10^{-10}$  mbar. The sample storage allows to prepare six samples under UHV conditions with only one baking out process being necessary. Due to the valve between the two chambers the preparation chamber stays under UHV conditions, while venting the sample load-lock in order to exchange samples.

## 7 Surface structures obtained after metal deposition

In chapter 2 different growth models already established in the literature were discussed. These growth models help to categorize the occurring growth phenomena and give an indication on the underlying basic mechanism. The influence of mechanical stress during film growth is discussed in chapter 3.

For the extremely flat TMDC crystals, one might intuitively expect a simple structure formation after metal deposition like cluster or thin film growth due to the van der Waals termination of the surface. Moreover, due to the similarity in the surface structure one might expect that the structure formation for all different chemical compositions of the layered crystals is similar. The very surface is in all cases (as explained in chapter 4) of hexagonal structure and does not exhibit open bonds or pronounced ionic character. This pronounced inertness is a special property of this material class which is different from commonly used crystals like, e.g., III/IV compounds *GaAs*, *InAs* or *InP*. At the surfaces of these crystals, unsaturated covalent bonds occur and result in different surface properties.

Surprisingly, various and very different structures can be found. In this chapter an overview is given over several examples for usual growth, that can be described with the standard growth models, and unusual growth on TMDC surfaces and edges. The structures found range from micron scale buckles in the form of tubes to large fractal islands. In other cases a collective cluster organization on the micrometer scale can be observed. The experiments were performed with different metals as adsorbates and TMDCs as substrate with metallic or semiconducting character and the geometric polytypes 1T and 2H (see chapter 4). All experiments in this chapter were performed on substrates at room temperature. The current chapter is dedicated to the introduction and categorization of the various structures and effects that occur upon evaporation of different metals on TMDC substrates.

A systematic variation of different parameters like e.g. deposition amount, substrate temperature will be demonstrated in the following chapter 8. There, the selected categories of surface phenomena will be put into the context of shape determining growth parameters.

Table 7.1 gives an overview of the different structures that are shown and discussed in this and the next chapter.

As explained in chapter 6.2 scanning electron microscopy (SEM) is an appropriate tool for material science analysis and it is especially suited for the kind of structures that will be investigated in the following. On a hierarchical scale one observes structures with differences in size from 5 nm up to 500  $\mu\text{m}$ . A further very useful tool for material science is the energy dispersive X-ray analysis (EDX, chapter 6.3) as a byproduct of the SEM. EDX is perfectly suited for the detection of chemical elements.

Complementary to SEM we used atomic force microscopy (AFM) in order to investigate the adsorbate topography on our samples. AFM possesses an extreme height sensitivity and therefore it is possible to detect structures on a smaller scale that would remain invisible for SEM. Furthermore, a second measurement technique always gives greater confidence in the reality of observed structures and excludes measurement artefacts as origin of the observed phenomena.

$T_{sub}$	Metal	WSe <sub>2</sub>	TaS <sub>2</sub>	TiS <sub>2</sub>	TiTe <sub>2</sub>	VSe <sub>2</sub>	HfS <sub>2</sub>
(RT)	Silver	X	X	dewetting film	X	X	X
	Chromium	X	cluster	cluster	X	X	X
	Copper	thin film	wires tunnel DLA growth	cluster	cluster	wires	cluster
100°C	copper	thin film	thin film	cluster	wires	wires	wires
-120°C	copper	thin film	wires tunnels	cluster	cluster	wires	cluster

**Table 7.1:** Table of observed structures after metal deposition.  $T_{sub}$  is the substrate temperature. RT means room temperature. X are not performed experiments.

On the other hand the height sensitivity makes AFM inadequate for samples with very large differences in height or with a jagged surface.

## 7.1 Homogeneous thin film growth

In this chapter only such systems of adsorbate and substrate are shown with no reconfiguration of adsorbate and substrate. That means neither the adsorbate shows any discernible structures nor the substrate. One can only observe a homogeneous thin film growth of the adsorbate.

### 7.1.1 WSe<sub>2</sub>

The semiconducting WSe<sub>2</sub> (band gap = 1.2 eV, Ref. [39]) exhibits no detectable reconfiguration of the substrate and adsorbate after copper evaporation as depicted in Fig. 7.1. The SEM image shows a typical surface of a cleaved crystal. The typical large defect free areas of several 10000  $\mu\text{m}^2$  are observed, which are limited by big step edges far above the atomic scale observable as bright lines due to the different topographic contrast. As the step edges appear bright, the remaining surface possesses the same topographic contrast. Even in higher magnification, no clusters can be observed, so the cluster size has to be below the contrast or resolution limit ( $\sim 5$  nm) of the SEM. In addition, there is no formation of structures at step edges observable like it is on other surfaces. That means step edges have in this case no influence on diffusion length and nucleation probability. This points to a homogeneous thin film growth as the most common growth on a defect free surface or a surface with a low defect density.

An EDX spectra (Fig. 7.2) was measured to exclude the complete desorption of copper and to ensure that a copper deposition takes place. A distinct copper signal can be observed which shows that the surface is covered with copper.

In Fig. 7.3 an EDX line scan of the copper L signal is shown that confirms the homogeneous distribution of the copper on the surface. The signal noise is a statistical and device effect. For comparison the inset shows an inhomogeneous copper signal as it can be achieved for e.g. copper on TaS<sub>2</sub>.

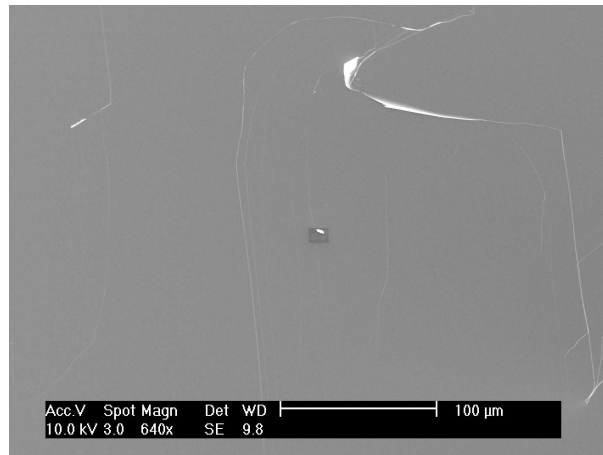


**Figure 7.1:** The SEM image shows a  $WSe_2$  surface after copper evaporation. Step edges are observed, but no further structures of adsorbate or substrate.

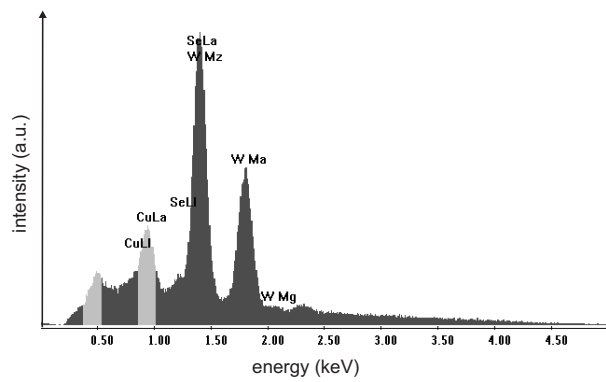


**Figure 7.2:** EDX spectra of a  $WSe_2$  surface after copper evaporation.

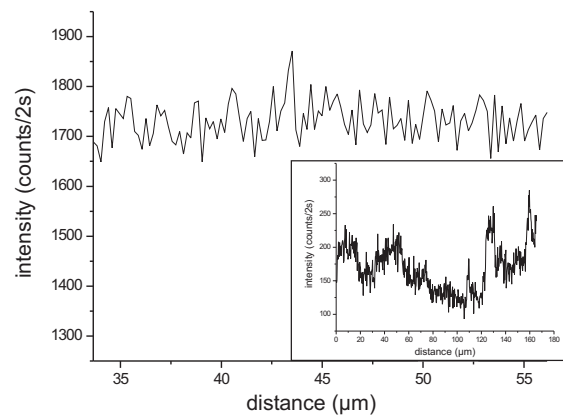


**Figure 7.3:** EDX line scan of the homogeneous copper L signal on a  $WSe_2$  surface after copper evaporation. In the inset you can see a line scan of an inhomogeneous copper signal (copper on  $TaS_2$ ).

In Fig. 7.4 an AFM image and a line scan profile of the  $\text{WSe}_2$  surface after copper evaporation is shown. The cluster diameter is about 200 nm but may be effected by the tip curvature. It is a well known effect that small lateral structures can not be resolved by scanning with a broad STM or AFM tip (see chapter 6.4). The line scan profile shows that the cluster height varies from 5 to 30 nm. A SEM can not resolve the clusters although they are larger than the resolution limit of the SEM due to the very low topographic contrast and the absence of any material contrast.

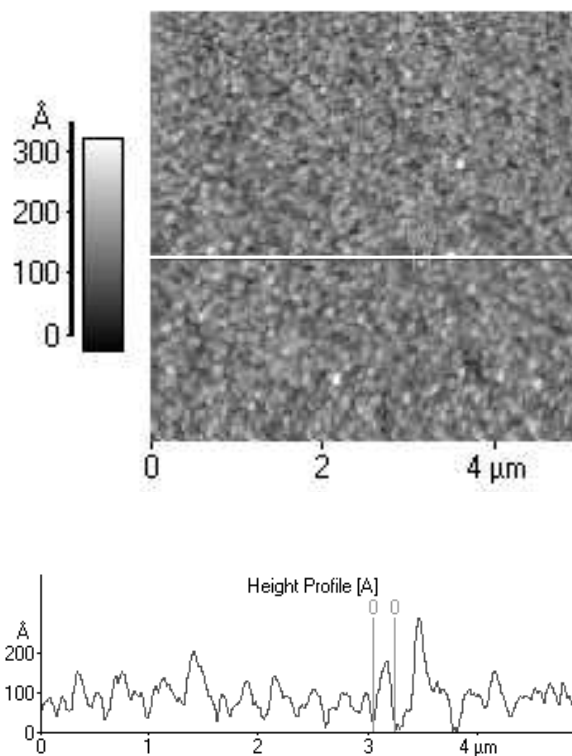


**Figure 7.4:** AFM image (contact-mode) of  $\text{WSe}_2$  and height profile along the white line after copper evaporation.

## 7.2 Adsorbate structures

This chapter shows complex adsorbate patterns obtained after metal deposition in contrast to the homogeneous adsorbate film growth introduced before.

### 7.2.1 $\text{TaS}_2$

Complex adsorbate patterns can be observed after chromium deposition on  $\text{TaS}_2$ . Chromium is used, e.g., to improve the adhesion between different materials because of its fast oxidation behavior on the one hand and its metallic bonding on the other (Ref. [40,41]). So it increases the adhesion between non-metallic and metallic interfaces. Chromium is often used for coating of ceramics to generate membranes for gas separation or detection (Ref. [42]).



In Fig. 7.5 the adsorbate structure of thermally evaporated chromium is shown. The thermally evaporated chromium leads to a needle like cluster growth on the metallic TaS<sub>2</sub>.

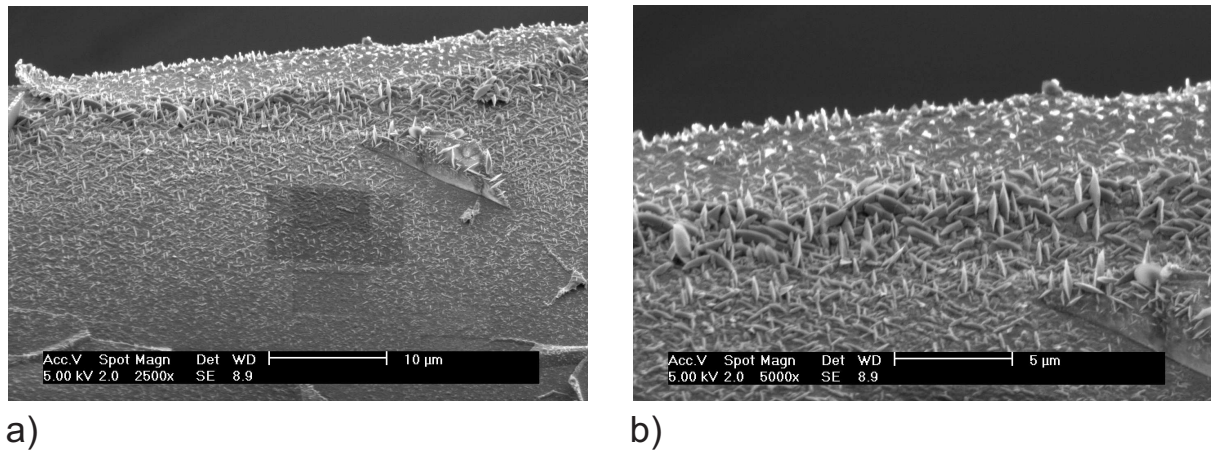


**Figure 7.5:** SEM images of a) low and b) higher magnification of a thermally evaporated chromium film on TaS<sub>2</sub>. Needle shaped structures appear on the crystal surface.

The clusters vary in size and orientation. The needle like clusters follow the trigonal in plane crystal symmetry of the [0001] crystal direction. They are orientated in three angles and each orientation differs from the other by an angle of 120°.

A completely different appearance can be found on the TaS<sub>2</sub> crystal surface after copper evaporation (Fig. 7.6). Copper is of high interest as it is used, e.g., as contact and conductor path material in electronic devices. On the TaS<sub>2</sub> surface we find an area that is masked by other crystal layers. This area is of special interest since it cannot be reached by evaporated copper atoms on a direct way but only by diffusing from the surrounding area. The diffusing copper atoms nucleate at the edge of the masked area and form fractal shaped structures that are characteristic for a DLA (diffusion limited aggregation) like growth mode (see chapter 2.5). In Fig. 7.6 d) a calculated DLA aggregate for a line attractor after [12] is depicted. In this case, the edges of the masked area and the line attractor act as comparable nucleation centers for the DLA aggregate. The morphology of the observed and calculated aggregates are quite well comparable. Such a growth mode denotes a relatively high diffusion length of the adsorbate atoms.

## 7.2.2 TiTe<sub>2</sub>

Even more complex structures can be found on some surfaces of the metallic TiTe<sub>2</sub> after thermal evaporation of copper under certain conditions. An example is shown in Fig. 7.7. One can observe cluster free areas surrounded by cluster fields in triangular or trapezoid shape and the inverted arrangement of the cluster formation. The cluster density is observed to vary on the same surface. Defects like step edges as a reason for such a cluster growth could not be found by SEM. Moreover, there is no indication of any defects of the surface. The structures can change their appearance from cluster to cluster free area within small distances and neighboring areas show the inverted cluster formation on the same surface (Fig. 7.8, 7.9).

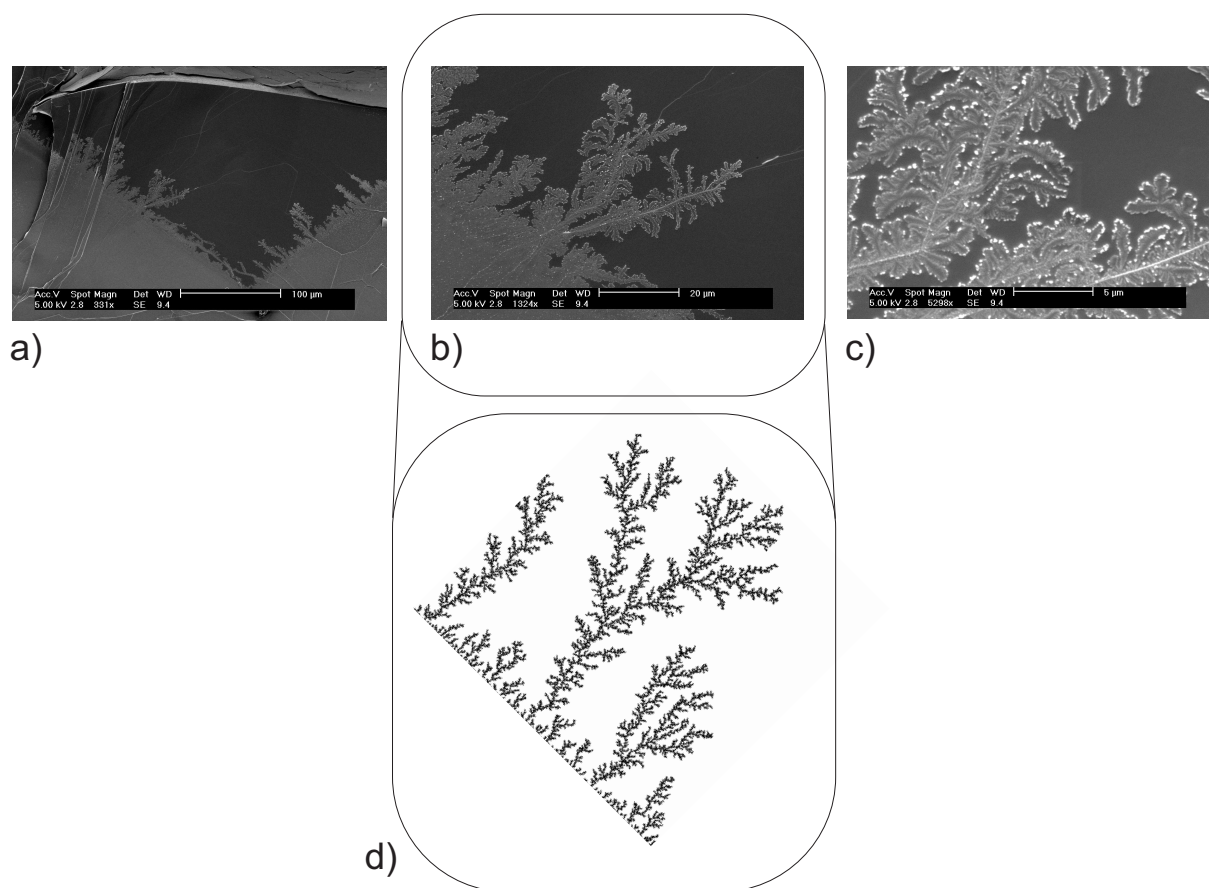


**Figure 7.6:** SEM image of a  $\text{TaS}_2$  crystal after copper evaporation. Image a) shows an area masked by other crystal layers. In the masked area fractal shaped structures can be observed. Image b) and c) show a DLA like growth mode of the adsorbate structures. d) is a calculated DLA aggregate for a line attractor.

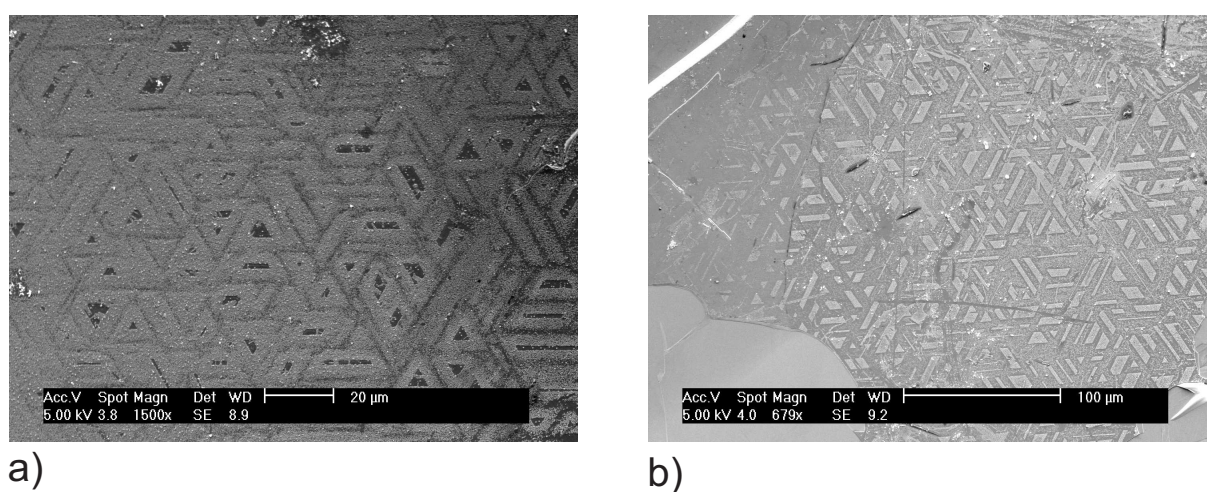


**Figure 7.7:** These SEM images show two adsorbate structures. In a) triangular and trapezoid shapes of cluster free areas b) clusters in triangular or trapezoid arrangement. These structures seem to be inverted with respect to the structures shown in a).

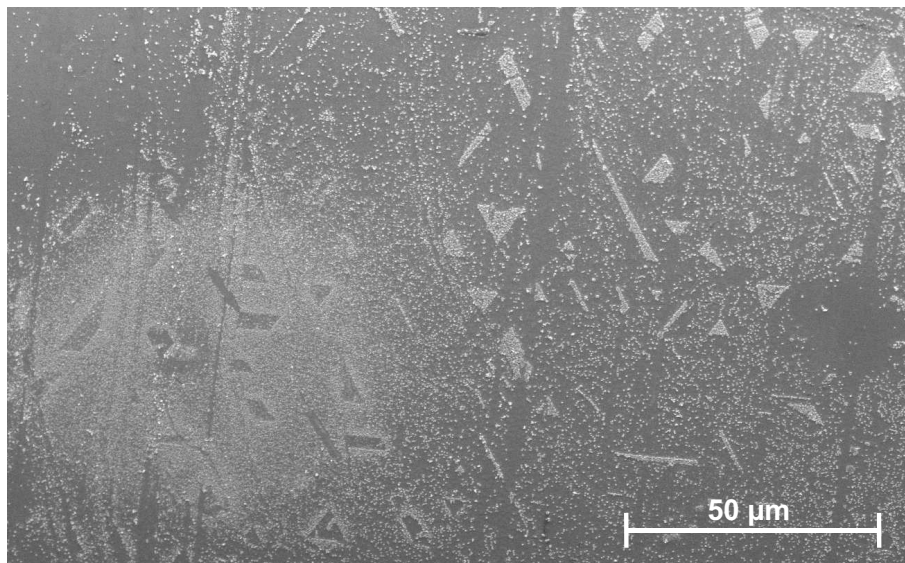


**Figure 7.8:** SEM image of the inversion of the copper cluster arrangement.

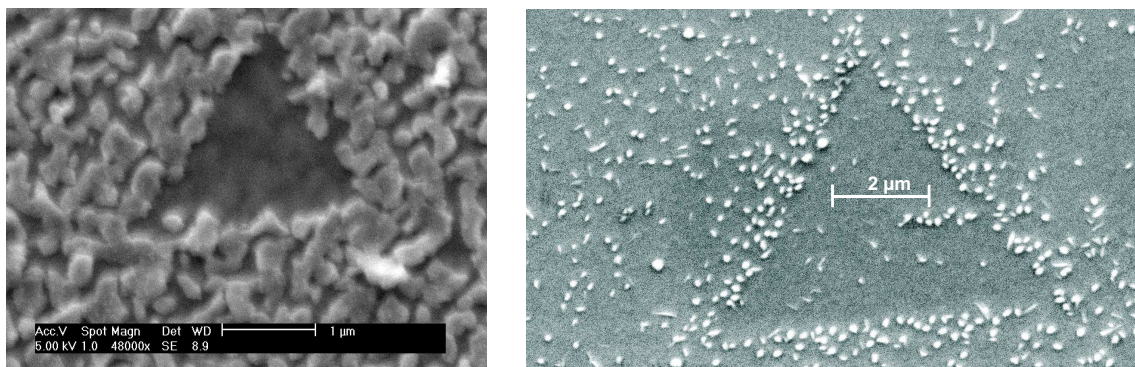


**Figure 7.9:** The SEM images show small triangular shaped free space, surrounded by copper clusters. In the left image the surrounding cluster density is constant. In the right picture a cluster density gradient is observable increasing from the the edge of the cluster free space.

This experiment was repeated several times with different crystals, there is no hint on step edges or other surface defects leading to the observed structures. The cluster arrangement appears to be aligned in accordance to the hexagonal crystal symmetry. The alignment of the structures is perfectly maintained over the whole crystal surface.

### 7.2.3 $\text{HfS}_2$

Contrarily to the metallic properties of the TMDC crystals  $\text{TaS}_2$  and  $\text{TiTe}_2$  that were investigated before, the following  $\text{HfS}_2$  exhibits semiconducting behavior (band gap  $\approx 2.1$  eV, Ref. [43]). After the evaporation of copper onto its surface one finds again a different growth mode. One can observe copper clusters as shown in Fig. 7.10, some build a discontinuous copper wire. The cluster density on the surface is varying. The cluster growth takes place

on a nearly defect free surface, there are no indications of step edges or other defects that could act as a nucleation center for the clusters.

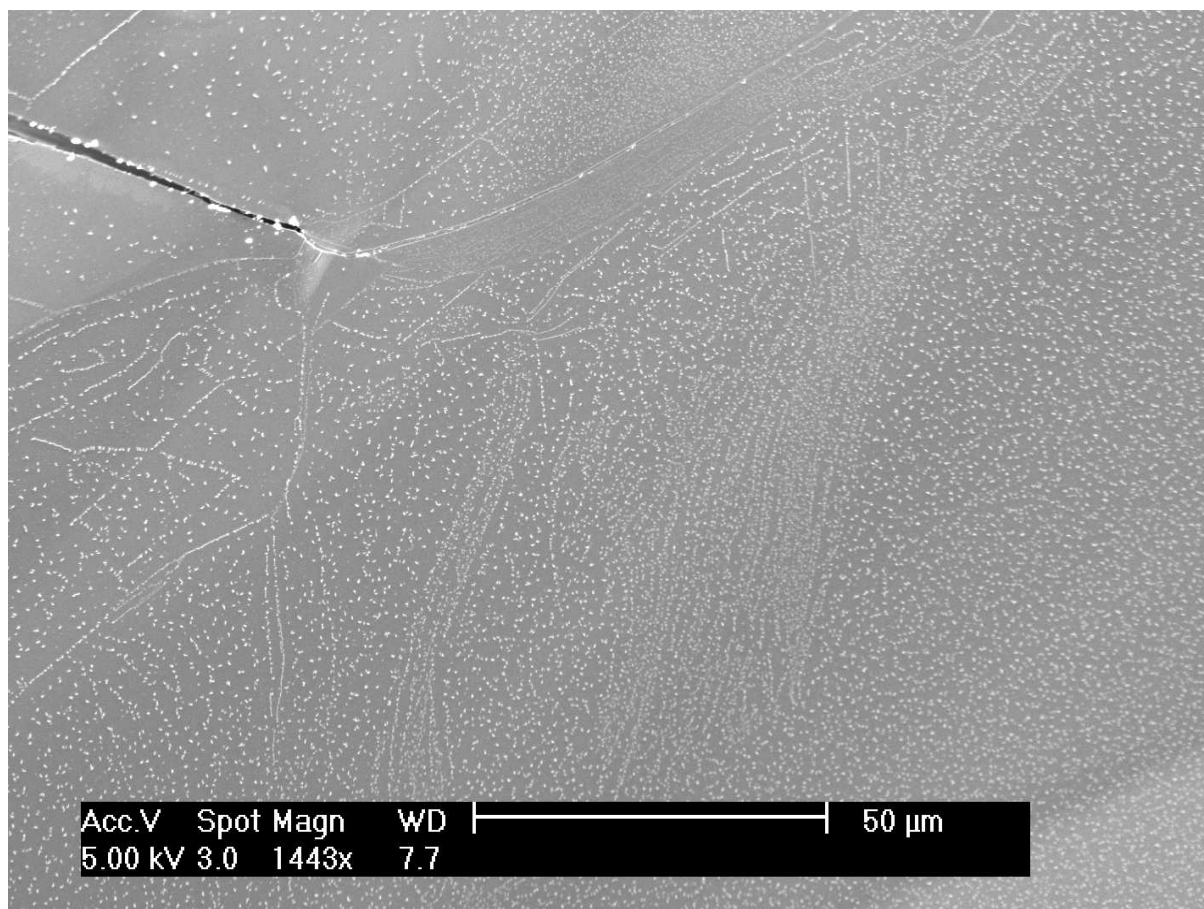


**Figure 7.10:** SEM image of copper clusters on  $\text{HfS}_2$ . In the image the copper clusters seem to form a discontinuous copper wire.

#### 7.2.4 $\text{TiS}_2$

$\text{TiS}_2$  is one of the most studied and best known TMDC in literature. In [44] and [45] it was used as a substrate for the epitaxy of PbS and turned out to be perfectly suited for this purpose. Here, the  $\text{TiS}_2$  is very reluctant to interact with the adsorbate. Sputtered silver leads to a remarkable dewetting effect of the silver film on the surface, see Fig. 7.11.

At step edges of  $\text{TiS}_2$  the interaction between adsorbate and substrate gets more interesting as shown in Fig. 7.12. On this sample not only the plane surface can be observed. We also get a view from the sample side. At the crystal side nanostructures with distances much larger than the triple layer thickness can be observed.

The complex structures nucleate at the step edges of the crystal nearly perpendicular to the edges. Some of the triangular structures exhibit a hole with a diameter of approximately 100 - 200 nm. It is possible that the dangling bonds of the edges might generate an anisotropic growth of deposited metal, observed in this case.

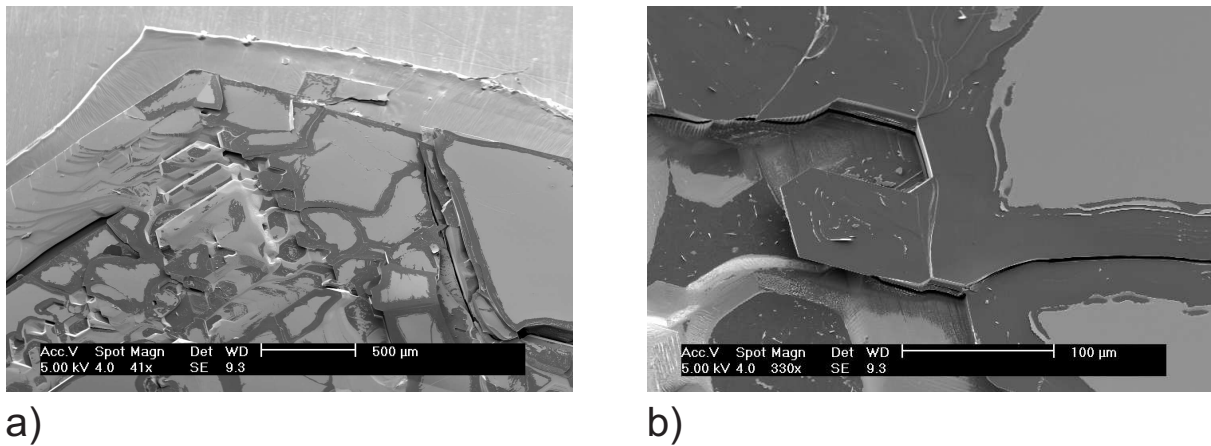


**Figure 7.11:** SEM image of  $\text{TiS}_2$  after silver sputtering. The silver film appears brighter than the crystal surface. Images a) and b) show a dewetting effect of the silver film.

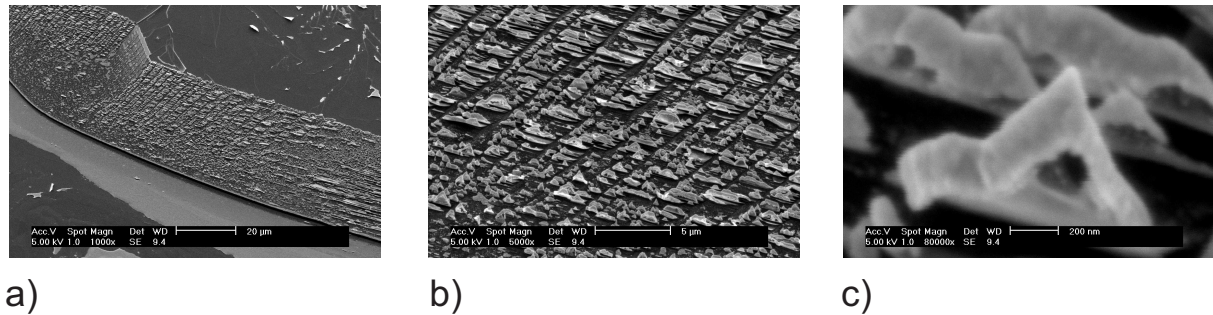


**Figure 7.12:** SEM image of  $\text{TiS}_2$  after silver sputtering. Image a) shows structures at step edges of the crystal. A higher magnification in image b) shows triangular structures. In image c) the structures appear complex.

### 7.3 Adsorbate-Substrate structure reconfiguration

In the preceding chapters 7.2 and 7.1 adsorbate structures were described that exhibited different shapes ranging from simple structures like thin films or homogeneous cluster growth or fractal shapes to more complex structures like the strict geometrical fields of clusters in the form of triangles and trapezoids.

However, these structures have in common that they do not significantly alter the geometrical structure of the underlying substrate. It appears that the film stays flat and no structures of mechanical failure can be observed.

In the following chapter the emphasis is laid exactly on this kind of structural changes.

#### 7.3.1 $\text{TaS}_2$

One of the pronounced examples for the complex interplay between adsorbate and substrate is given by the system  $\text{TaS}_2$ /copper.

After copper deposition the surface layers of the crystal begin to buckle and one can observe a buckle network of different sizes. The first one is a fine buckle network following the threefold crystal symmetry. The buckles possess sharp defined edges. The width of the

buckle is about one  $\mu\text{m}$  with a typical mesh with of 50 to 100  $\mu\text{m}$ . With increasing amount of evaporated copper the buckles become larger (Fig. 7.13) but their width is still in the range of several  $\mu\text{m}$ . The mesh width is in some regions reduced and varies from 10 to 100  $\mu\text{m}$ . Finally, the network will end up in tubes with roundly edges that are formed from the uppermost substrate layers. The tubes possess a typical width of about 5 to 20  $\mu\text{m}$  and the mesh width is in the range of 10  $\mu\text{m}$ .

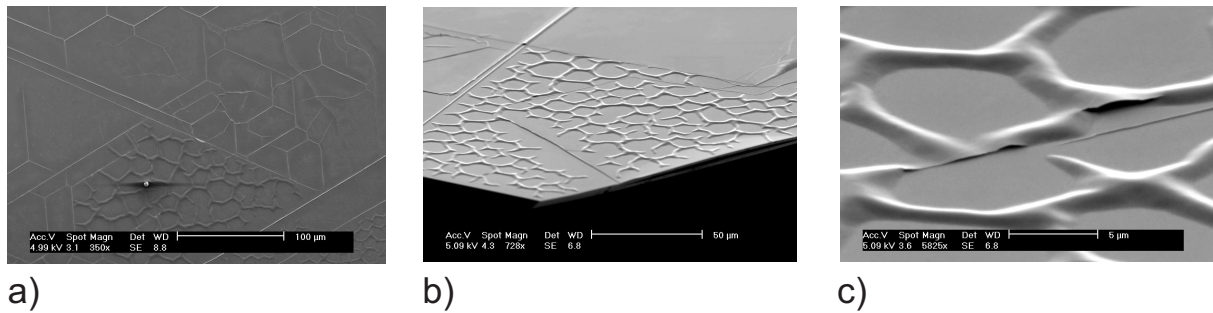


**Figure 7.13:** SEM images of the  $\text{TaS}_2$  surface after thermal evaporation of copper. Image a) shows a tunnel and buckle network. Image b) shows buckles of surface crystal layers. In image c) cracks in the buckles can be observed.

In Fig. 7.14 the different buckle networks are schematically depicted in order to obtain a better understanding of their structures and differences. The lean network can be considered as by a certain angle, e.g  $\alpha$ , upfolded surface layers with straight sides. Their orientation follows the hexagonal crystal symmetry. The larger tube network possesses no sharp edges or straight sides. The buckles have a round shape. As one can see in Fig. 7.13 c) there are cracks in the tubes and inside the tubes are concave. Also the tubes seem to consist of several upfolded surface layers. The orientation of the tubes follows still a weak threefold symmetry.

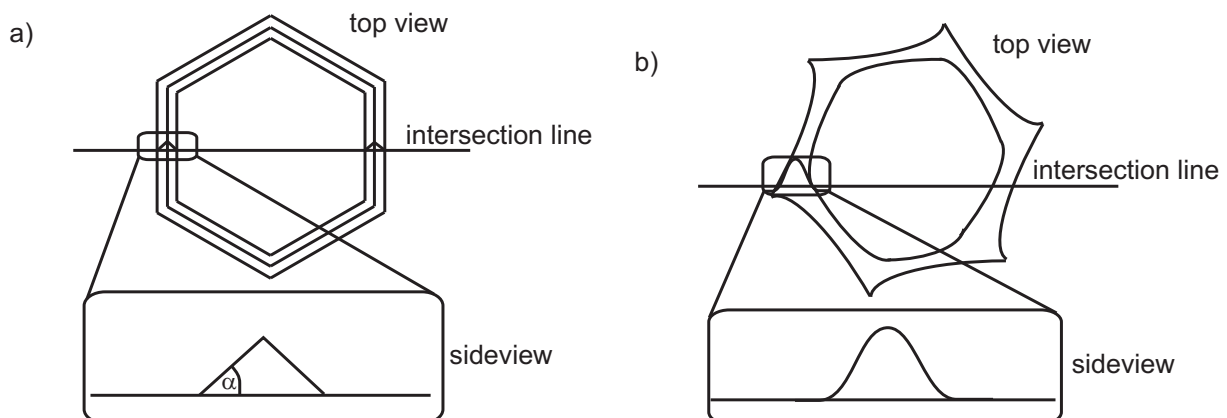


**Figure 7.14:** Schematic top view of the buckle networks and cross sections a) of the lean buckle network and b) of the tube network.

These buckling phenomena appears similar to the theoretical aspects of thin film cracking and debonding described in chapter 3.3 and 3.4, see Fig. 3.1 and Fig. 3.3.

### Aspect of in situ relaxation of a surface by charge or temperature insertion

Even SEM imaging of TaS<sub>2</sub> after copper deposition can change the surface. This is shown in Fig. 7.15. The same area was scanned several times. The impinging electrons lead to buckles by electronically or thermally induced changes of the surface. The imaging leads to the observed structures within a few minutes.

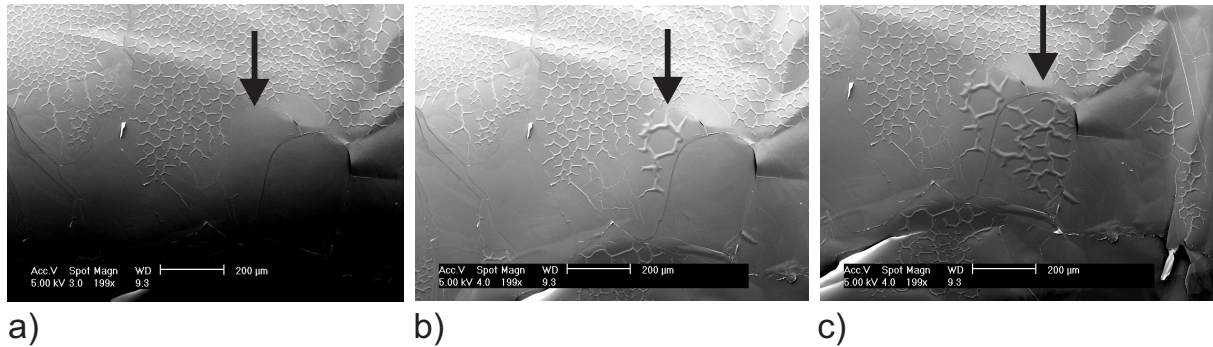


**Figure 7.15:** SEM image series of a TaS<sub>2</sub> surface after copper evaporation. In figure a) the tunnel network is shown. The black arrow shows the region of interest. Figure b) is an image of the same region shortly taken after the image in figure a). Big buckles (black arrow) appear. Figure c) shows further buckles (black arrow) of the surface.

### 7.3.2 VSe<sub>2</sub>

A structure network similar to the observed network on TaS<sub>2</sub>, but on a different length scale, will be also created on VSe<sub>2</sub> surfaces upon the deposition of copper. An example is shown in Fig. 7.16.

The structures have different sizes up to several  $\mu\text{m}$ . In the left part of the image one can observe elevated crystal layers. The network is distributed over the whole crystal surface, even in corrugated surface areas. At junctions the structures meet under angles of about  $120^\circ$ . The structures are thinner than the structures observed on TaS<sub>2</sub> but they seem to be analogical. It is obvious that the crystal surface layers are cracked in some areas.

The typical network sizes are shown in Fig. 7.17. The AFM image shows the microstructure network and the line scans below the image visualize the height and diameter of the structures within the network. The diameter ranges from 100 nm up to 500 nm with heights between 10 nm and 80 nm.

In Fig. 7.18 STM images of the nanostructure network are shown. Scanning tunneling microscopy has an even higher lateral and height resolution than atomic force microscopy. STM offers the possibility to resolve the microstructures that are located in between the larger meshes of the network that were visible by AFM (Fig. 7.17). The width of the microstructures is in the range of  $\approx 50$  nm. The upper picture shows a STM picture of a sample region after only a few movements of the scanning tip over the surface. The lower picture was taken after several scanning sequences.

It is observable that the interaction between tip and surface has led to the removal of the adsorbed material and the microstructure has become discontinuous. Below the removed material a crack can be observed.

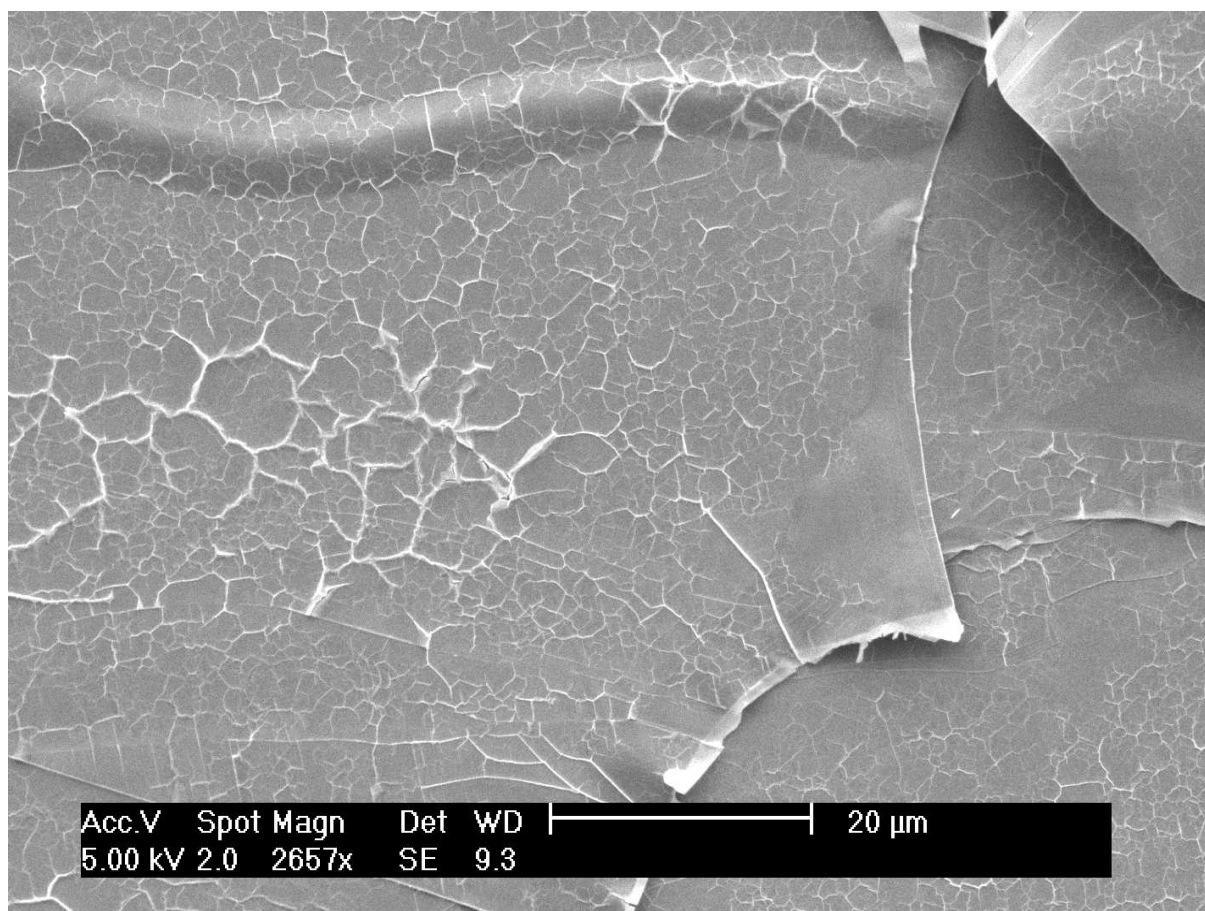


**Figure 7.16:** SEM image of the wire and tunnel network on  $VSe_2$  after copper evaporation.

In summary, a whole bunch of different structures could be found that are formed on the surface of TMDC crystals after deposition of different adsorbate materials.

In some cases the occurring structures do not affect the substrate surface in a significant way but form just differently shaped clusters that arrange either arbitrarily as thin films (chapter 7.1) or along substrate crystal symmetry lines (chapter 7.2).

Finally, for occurring network structures a distinct influence of the adsorbed species on the underlying substrate could be observed resulting in a modification of the surface in the form of buckles, tubes and cracks (chapter 7.3).



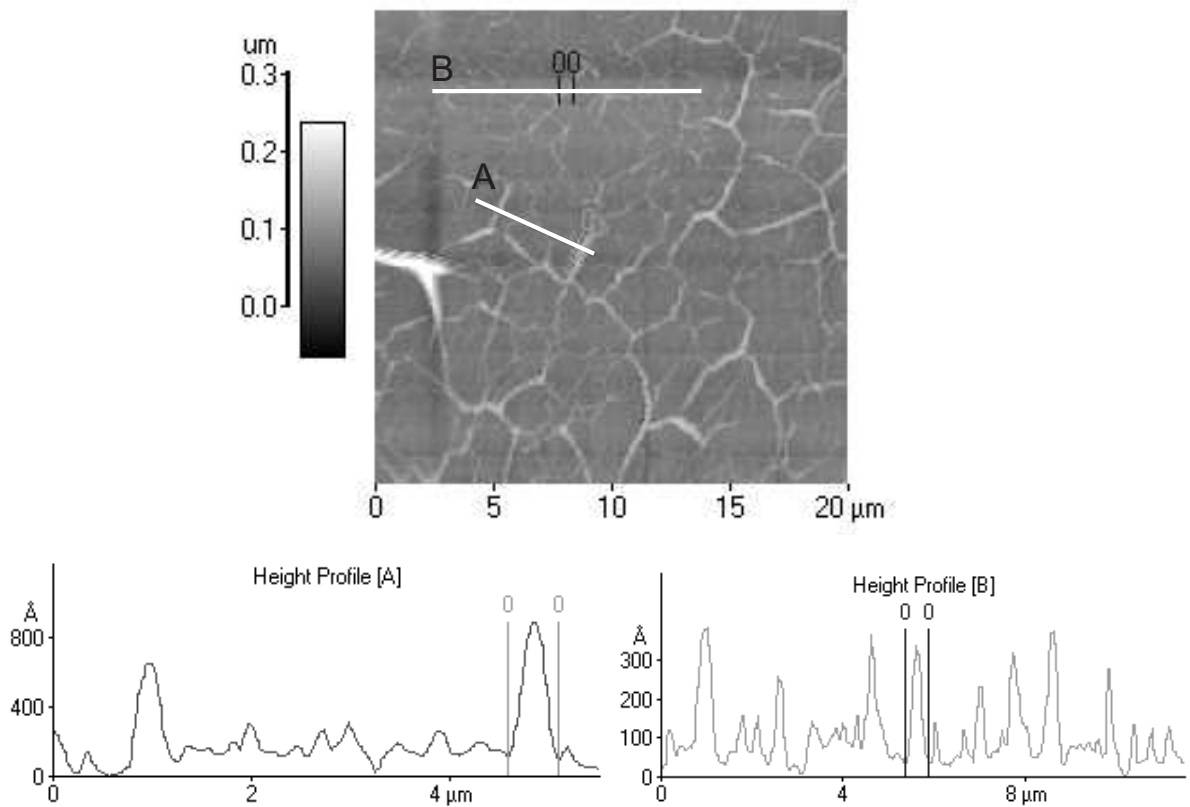


**Figure 7.17:** AFM image (contact-mode) of the wire and tunnel network on  $VSe_2$  after copper evaporation. Below the image two line scans along the white line A and B of different network sizes are depicted.

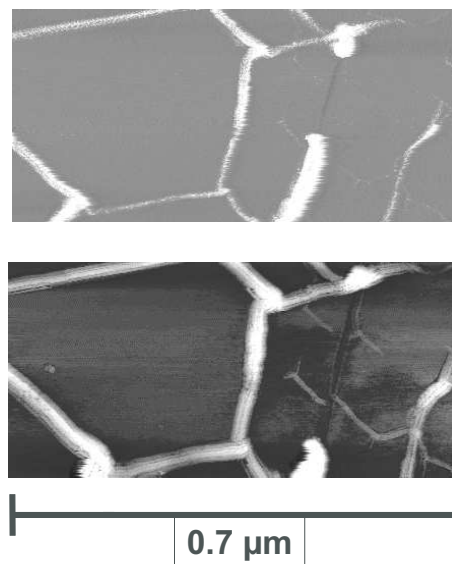


**Figure 7.18:** STM images of the wire and tunnel network on  $VSe_2$  after copper evaporation.

## 8 Variation of the deposition parameters

The experiments of the preceding chapter 7 have shown that various structures can be found on TMDC surfaces after the deposition of different metals. This large variety leads to the question why such different structures can occur on physically and chemically similar surfaces. The growth mode is strongly influenced by the following parameters:

System parameters are

- the substrate
- the adsorbate

Deposition parameters are

- the deposition amount
- the deposition rate
- the substrate temperature

Growth parameters are

- the adsorption probability
- the desorption probability
- the nucleation probability
- the diffusion length

In order to investigate the influence of the above mentioned parameters on the growth behavior some parameters were held constant. This is the deposited metal, which is copper in all cases. The evaporation method was not varied; the copper was always evaporated thermally under UHV conditions.

The parameters that were varied include the substrate, so different TMDC crystals were used. The substrate temperature was systematically altered, thus growth parameters like adsorption and desorption probability and diffusion length could be changed. They are inherently depending on the substrate temperature.

The deposited amount of evaporated metal was also varied to affect the nucleation probability.

### 8.1 Deposition amount and rate

In this chapter the influence of the film thickness of the evaporated copper on the occurring structures will be described. The amount of deposited material on a surface may have a (large) influence on the growth. As explained in chapter 2, in standard growth models, in the first stadium, when only a little amount of material is deposited, single atoms can diffuse freely over the surface. The deposited atoms will nucleate at positions (e.g. defects) where a minimum of the relative free energy in relation to the different particle positions

with respect to the underlying surface atoms is reached (extrinsic nucleation). Such a nucleation center will trap more diffusing atoms and a cluster growth can take place (intrinsic nucleation by extrinsic nucleation). The deposition rate has an influence on such a process because a higher deposition rate leads to a higher concentration of diffusing atoms. A change of the relative free energy in relation to the different particle positions with respect to the underlying surface atoms will follow. The probability of intrinsic nucleation of the evaporated material increases. Cluster growth can take place without any defects (Ref. [6]). The cluster growth may induce a complex stress field into the substrate that leads to the mechanical failure of the substrate surface layers (Ref. [22]). New defects for further extrinsic and intrinsic nucleation are generated.

### TaS<sub>2</sub>

The evaporation of copper generates a microstructure network on the TaS<sub>2</sub> surface, produced by buckling of several crystal surface layers. If the substrate temperature is at room temperature the occurring network depends strongly on the film thickness of the evaporated metal. Fig. 8.1 shows the structure formation on TaS<sub>2</sub> after the deposition of an increasing amount of copper. The nominal film thickness of the deposited copper is varied from 5 nm to 20 nm. One can observe different tunnel networks, already described in chapter 7.3.1. The first one, shown in Fig. 8.1 a) is a fine tunnel network, following the crystal symmetry. In Fig. 8.1 b) the fine tunnel network can be observed and parallel to it a thicker tunnel network still following the crystal symmetry appears. In Fig. 8.1 c) large tunnels appear next to the the lean tunnel network. With increasing amount of evaporated copper the network density increases as well.

It is not possible to understand such a phenomenon only by diffusion processes of the adsorbate material. There are other mechanisms one must consider.

### TiTe<sub>2</sub>

Evaporation of copper on TiTe<sub>2</sub> at room temperature does not lead to a microstructure network, except for the cluster formation described in chapter 7.2.2. In Fig. 8.2 one can find a thin film growth different from the cluster formation shown in the mentioned chapter. The nominal film thickness of the deposited copper is varied from 5 nm to 20 nm, but no structures occur in the SEM images. There is only the cleaved crystal surface observable. Nevertheless, EDX measurements verify the increasing amount of deposited copper.

## 8.2 Substrate temperature

In this chapter the influence of the substrate temperature on the occurring structures will be investigated, the results will be shown and discussed.

### TaS<sub>2</sub>

Fig. 8.3 a) depicts the surface after the evaporation of copper at room temperature. Again it shows the resulting network of differently sized microstructures. Increasing the substrate temperature to 100 °C leads to a completely different appearance of the surface after

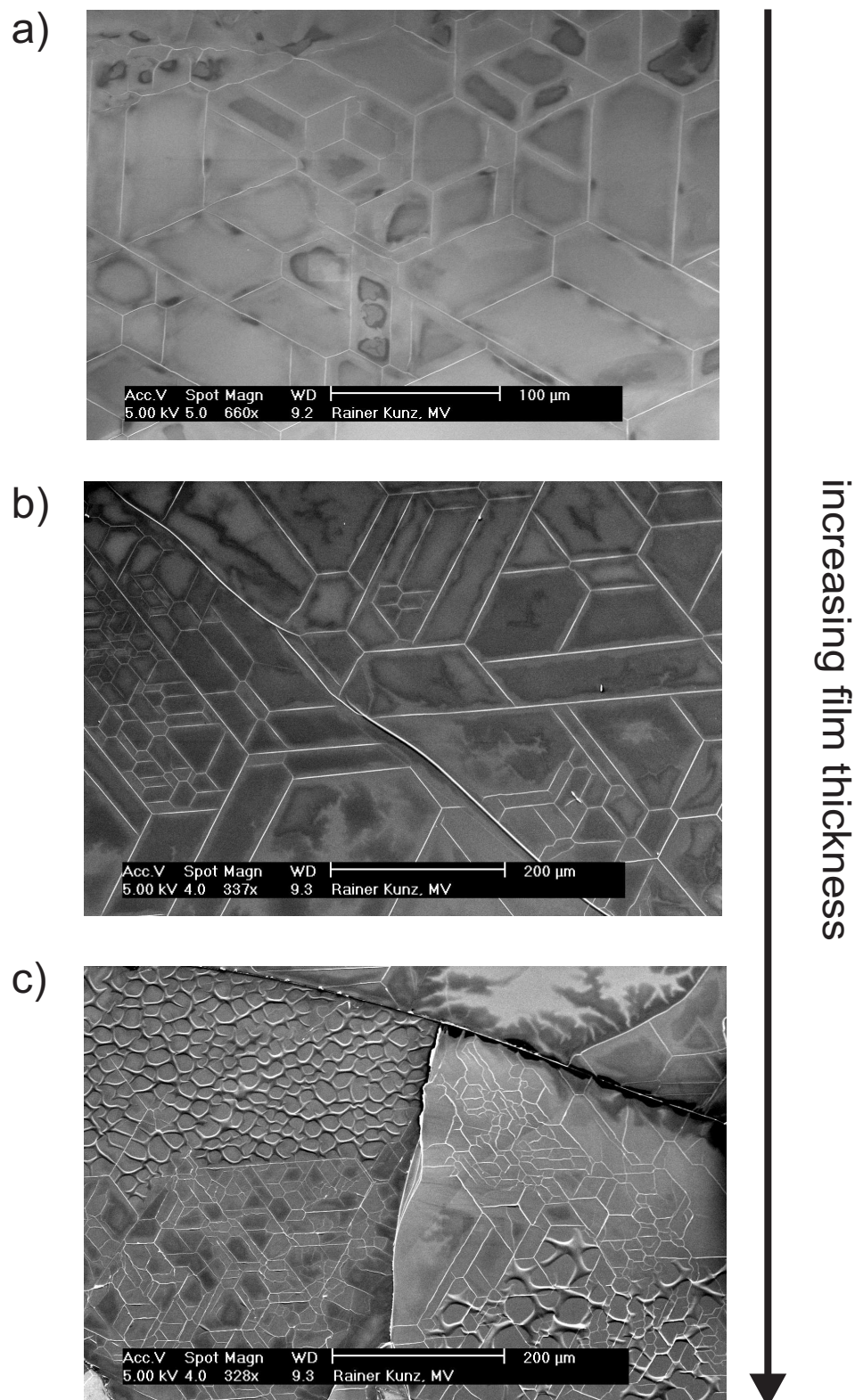


**Figure 8.1:** SEM images of a TaS<sub>2</sub> surface after copper evaporation at RT. The images show an increasing nominal copper film thickness of a) 5nm, b) 10nm and c) 20nm.

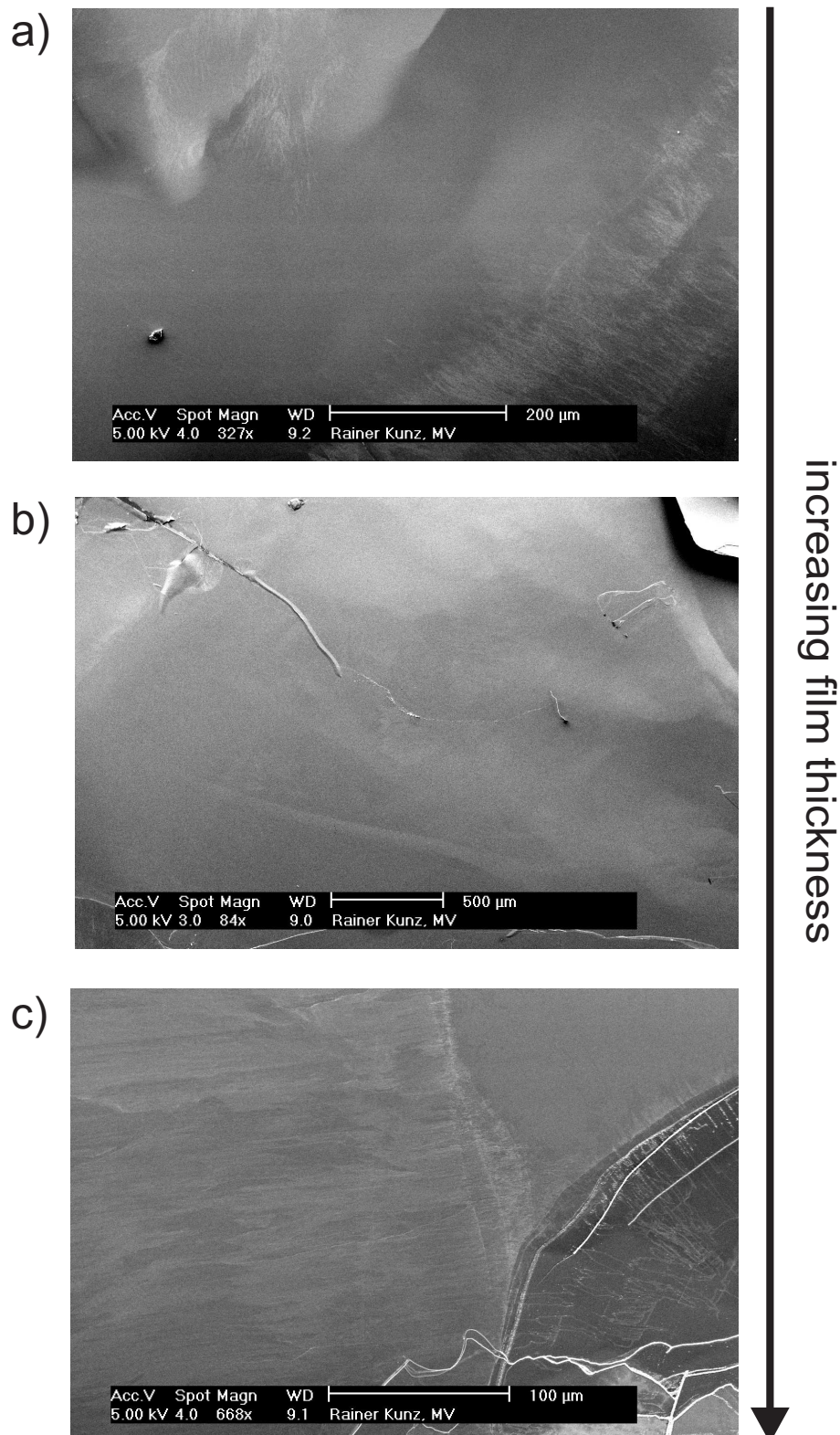


**Figure 8.2:** SEM images of a TiTe<sub>2</sub> surface after copper evaporation at RT. The images show an increasing nominal copper film thickness of a) 5nm, b) 10nm and c) 20nm.

evaporation as it is shown in Fig. 8.3 b). Here, no distinct structures can be observed. It seems a thin film growth of the copper takes place.

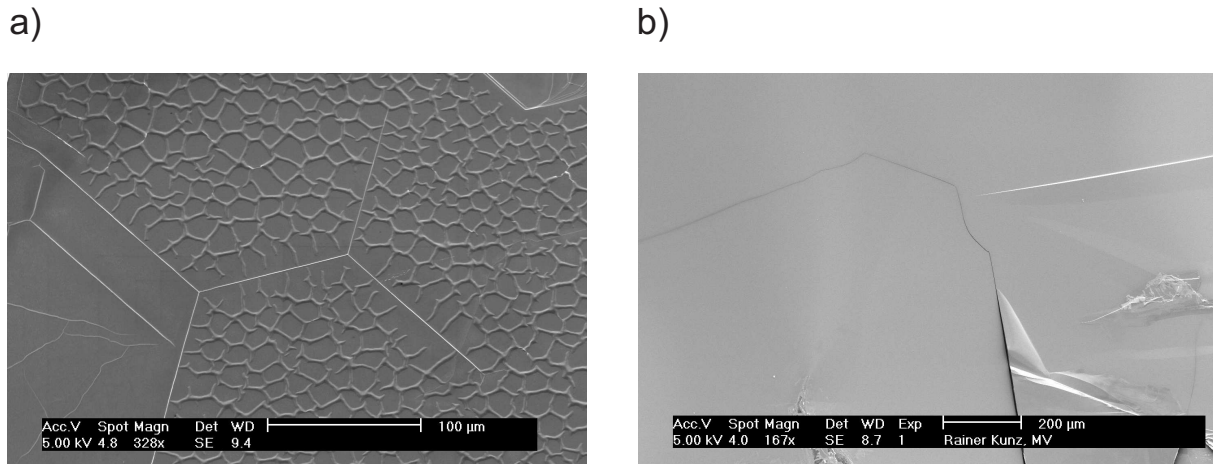


**Figure 8.3:** SEM images of TaS<sub>2</sub> surface after copper evaporation at a) RT and b) 100 °C. The nominal film thickness is about 20 nm.

Decreasing the temperature of the substrate to  $-120\text{ }^{\circ}\text{C}$  during preparation on the other hand leads to a more randomly organized microstructure network and is depicted in Fig. 8.4. The tunnels possess no sharp edges and there is only a poor threefold symmetry. The smaller scale image on the right indicates that the microstructure distribution is comparable to the microstructures obtained after copper deposition at room temperature. The tunnel width and the mesh width are equal.

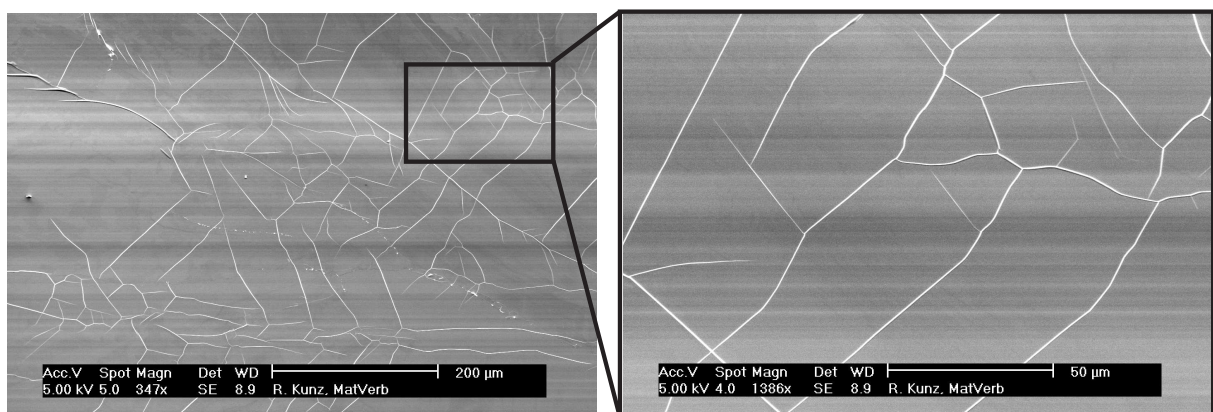


**Figure 8.4:** SEM images of TaS<sub>2</sub> surface after copper evaporation at  $-120\text{ }^{\circ}\text{C}$ . The nominal film thickness is about 10 nm.

## TiTe<sub>2</sub>

As already mentioned, the preparation of copper on TiTe<sub>2</sub> at room temperature does not lead to a microstructure network as can be seen in Fig. 8.5 a).

Increasing the substrate temperature to 100 °C leads to the formation of network structures (see Fig. 8.5 b)). The difference in the behavior of TaS<sub>2</sub> and TiTe<sub>2</sub> upon temperature

variation appears inverted: While the increase of temperature of TaS<sub>2</sub> results in the disappearance of a network that exists at room temperature, TiTe<sub>2</sub> shows the opposite behavior. The network only appears at elevated temperatures.

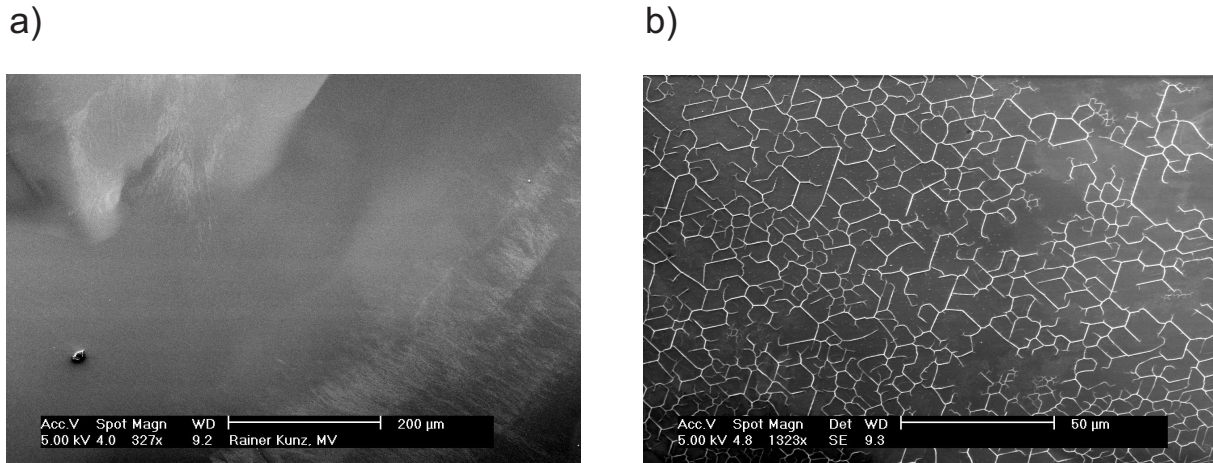


**Figure 8.5:** SEM images of TiTe<sub>2</sub> surface after copper evaporation at a) RT and b) 100 °C. The nominal film thickness is about 20 nm.

Additionally to the network copper clusters can be found decorating step edges on TiTe<sub>2</sub> (Fig. 8.6). In the left image one can observe copper clusters of a different size distribution. Some clusters nucleate at step edges and form a discontinuous copper wire. The right image shows a region with clusters around a step edge. A depletion zone in the order of 100 nm next to the step edge can be observed. In this area the nucleation probability has to be reduced. At the step edges the nucleation probability appears to be increased at elevated temperatures.

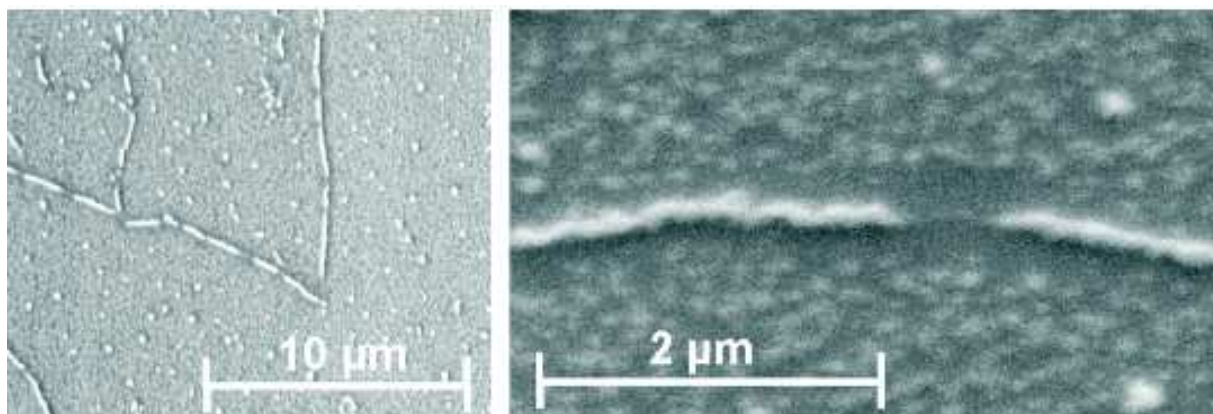


**Figure 8.6:** SEM images of TiTe<sub>2</sub> surface and copper clusters after copper evaporation at 100 °C. The nominal film thickness is about 20 nm.

In Fig. 8.7 a) copper preparation on TiTe<sub>2</sub> at a substrate temperature of −120 °C again does not lead to a microstructure network. The deposited copper forms a thin film. A new effect can be noticed here: Around step edges the SEM images show darker areas. Obviously, less adsorbate material is deposited here, i.e. a depletion zone is formed around

step edges on  $\text{TiTe}_2$  at low temperatures. The low amount of copper in the depletion zone is verified by the EDX line scan in Fig. 8.7 b) where a lower copper signal can be observed.

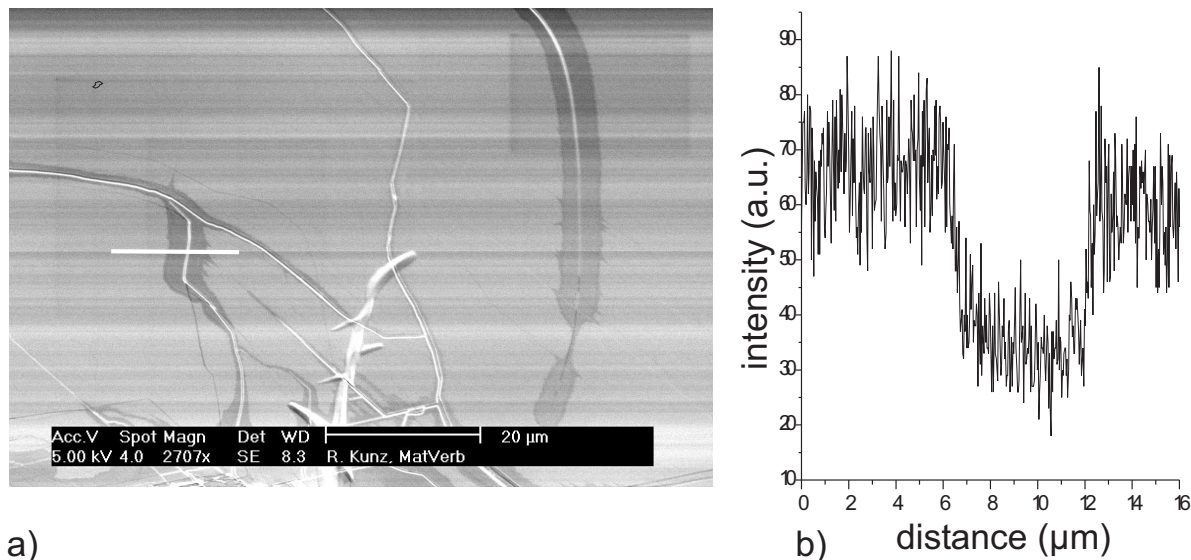


**Figure 8.7:** a) SEM images of  $\text{TiTe}_2$  surface after copper evaporation at  $-120^\circ\text{C}$ . The nominal film thickness is about 10 nm. b) EDX line scan of the copper L signal along the white line in image a).

## $\text{HfS}_2$

As a semiconducting substrate for the study of temperature variation,  $\text{HfS}_2$  was chosen. The copper deposition took place at room temperature and at  $100^\circ\text{C}$ , respectively. During this preparation the surface was masked with a TEM grid (a small copper grid used for investigations in a TEM). This was done for other reasons as are explained in chapter 8.2.2 but should not be taken into account here. The respective SEM images are shown in Fig. 8.8. In both cases the evaporation of copper results in cluster formation on the surface. For higher temperatures the morphology changes, the clusters become bigger and more flaked. Furthermore, more detailed investigations show a microstructure network in between the clusters (Fig. 8.9). It is comparable with the temperature dependence of the growth mode on  $\text{TiTe}_2$  where a formation of a microstructure network is only observed for elevated temperatures (see Fig. 8.5).

The EDX overview spectra in Fig. 8.9 shows that a deposition of copper took place. The EDX spectra of an area with a high cluster density clearly indicates that the clusters consist mainly or completely of copper. The cluster free area shows only a small copper EDX signal.

In Fig. 8.10  $\text{HfS}_2$  surface after copper preparation at  $-120^\circ\text{C}$  is shown. In this case no microstructures or clusters can be observed, a thin film growth of copper takes place. The bright lines in the image represent step edges. The copper is distributed evenly over the surface. The density does not change in the vicinity of the step edges like it does in other cases (see e.g. Fig. 8.7).



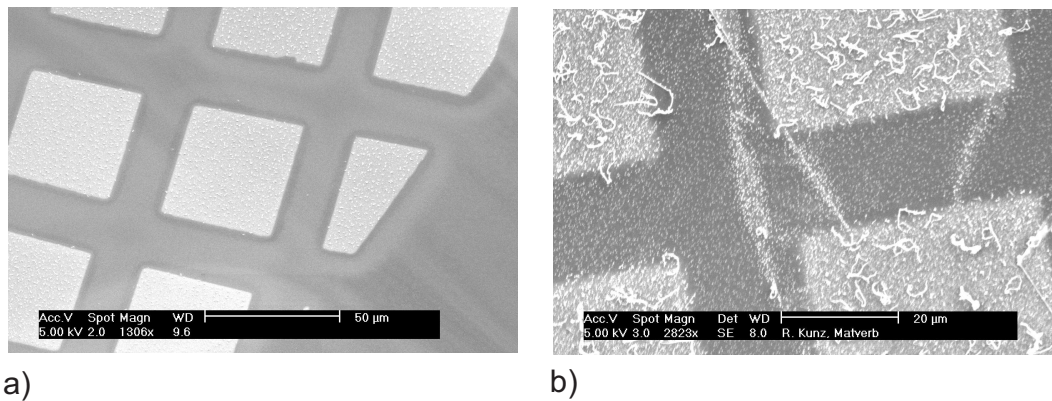


**Figure 8.8:** SEM images of  $\text{HfS}_2$  surface after copper evaporation at a) RT and b) 100 °C. The nominal film thickness is about 20 nm.

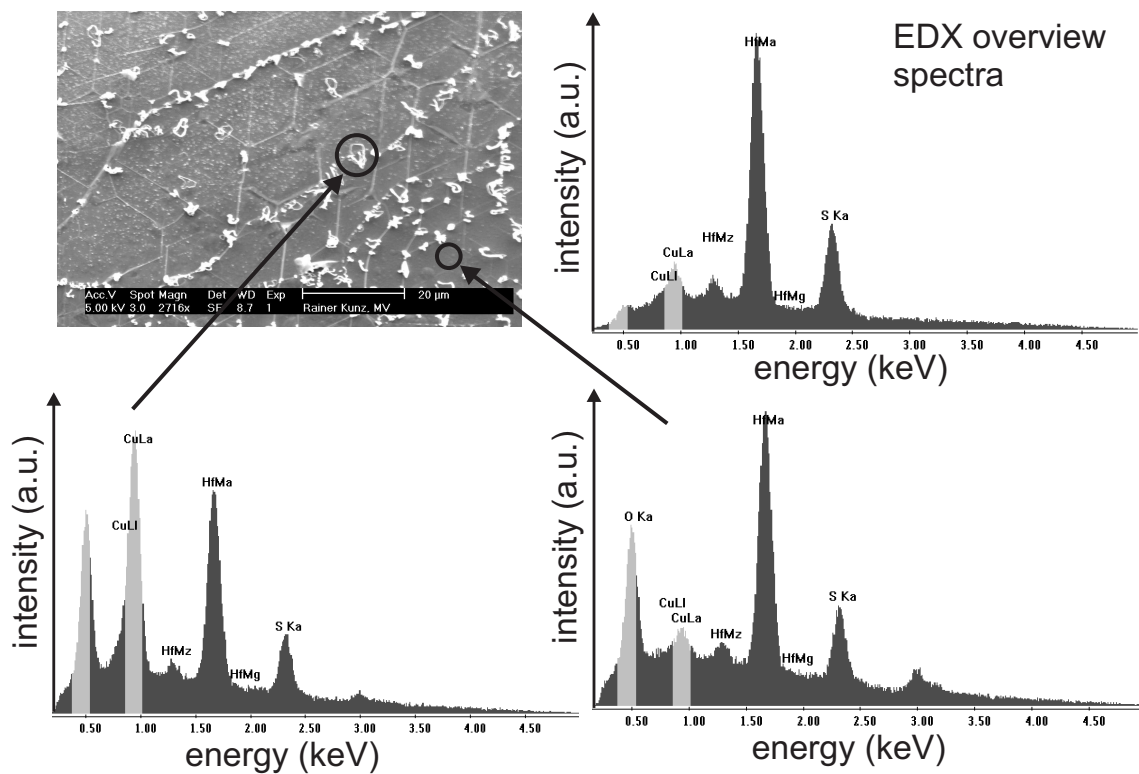


**Figure 8.9:** SEM image of  $\text{HfS}_2$  surface after copper evaporation at 100 °C. The nominal film thickness is about 10 nm. In addition, EDX spectra measured over the whole surface area (top right), over an area with high cluster density (bottom left) and over a cluster free area (bottom right) are shown.

## $\text{WSe}_2$

For comparison, Fig. 8.11 shows a preparation of copper at a) room temperature and at b) 100 °C in this case on  $\text{WSe}_2$ . The two SEM images look different but that is an effect due to contrast and brightness. As already mentioned  $\text{WSe}_2$  does not show discernible structures at all, even at different deposition parameters. Only step edges can be observed.

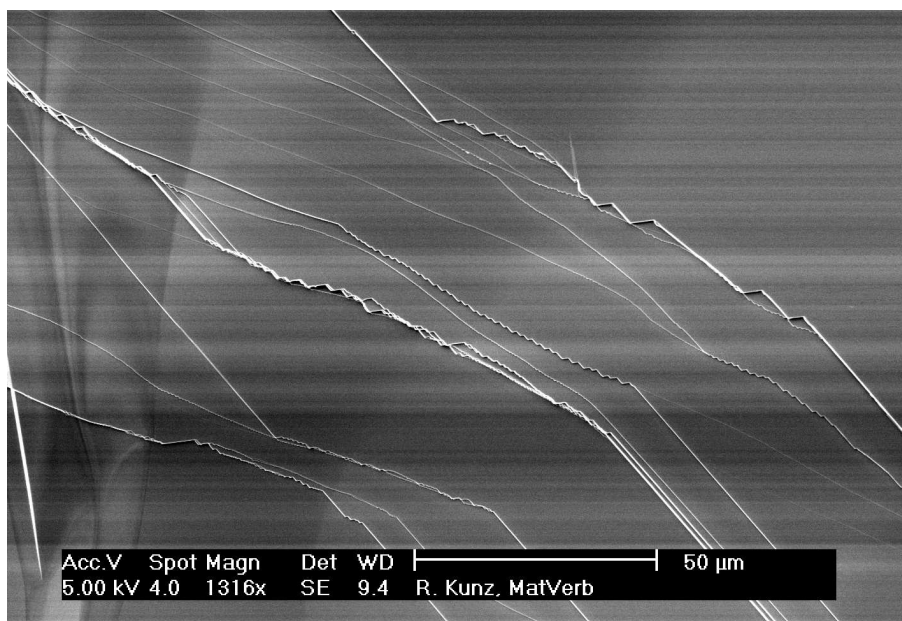


**Figure 8.10:** SEM images of  $\text{HfS}_2$  surface after copper evaporation at  $-120^\circ\text{C}$ . The nominal film thickness is about 10 nm.

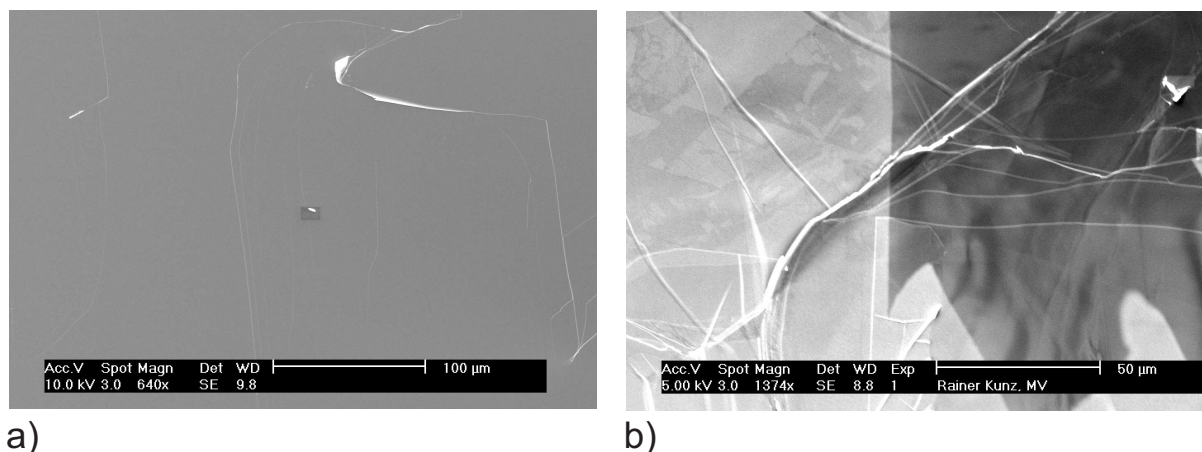


**Figure 8.11:** SEM images of  $\text{WSe}_2$  surface after copper evaporation at a) RT and b)  $100^\circ\text{C}$ . The nominal film thickness is about 20 nm.

The same applies to the preparation of copper on  $\text{WSe}_2$  at  $-120^\circ\text{C}$  as is depicted in Fig. 8.12. No distinct structures occur except step edges as an effect of the crystal cleavage.

### $\text{VSe}_2$

The evaporation of copper on  $\text{VSe}_2$  has a similar effect as copper evaporation on  $\text{TaS}_2$ : The surface layers begin to buckle. There are also large differences. In the case of copper on  $\text{VSe}_2$  the structures are several orders of magnitude smaller compared to the structures on  $\text{TaS}_2$ . The size of the microstructure network is distributed from several nm up to the  $\mu\text{m}$  scale. The structure alignment is also different as it follows only to a minor degree the

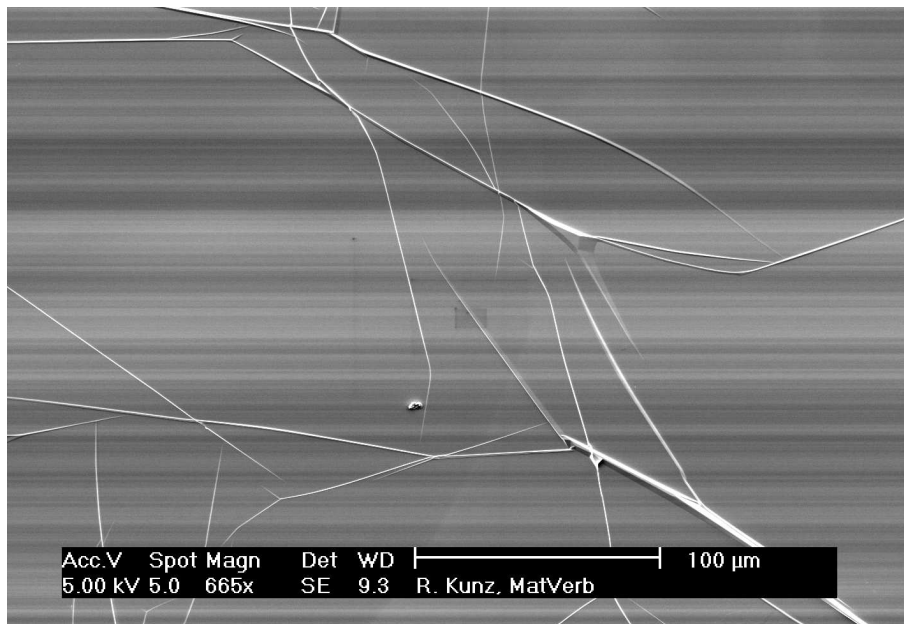


**Figure 8.12:** SEM images of  $\text{WSe}_2$  surface after copper evaporation at  $-120^\circ\text{C}$ . The nominal film thickness is about 10 nm.

hexagonal crystal symmetry.

In Fig. 8.13 copper evaporation a) at room temperature and b) at  $100^\circ\text{C}$  is depicted. One can observe a large microstructure network with cracks in the surface layers. There are no differences of the structures with respect to the substrate temperature.

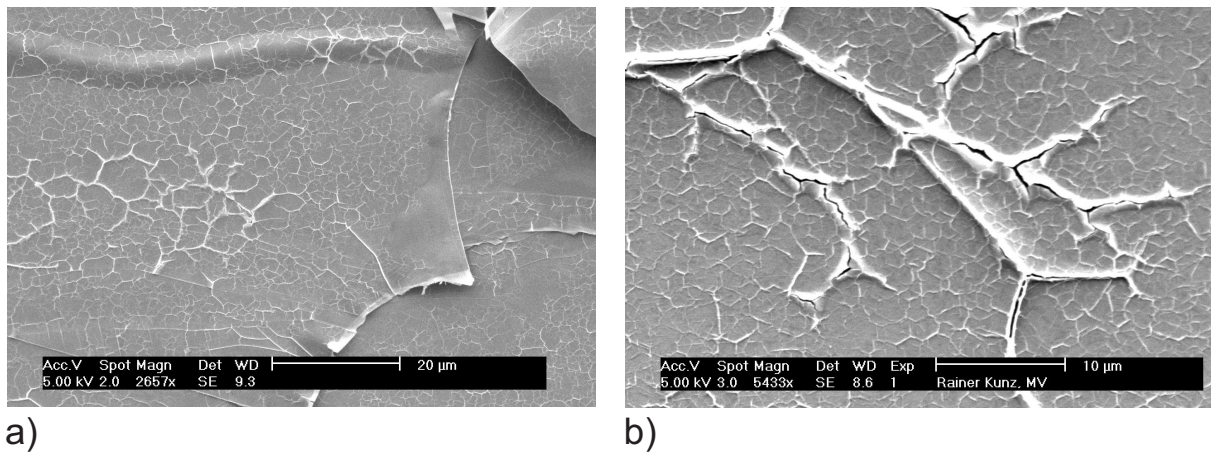


**Figure 8.13:** SEM images of  $\text{VSe}_2$  surface after copper evaporation at a) RT and b)  $100^\circ\text{C}$ . The nominal film thickness is about 20 nm.

A SEM image with a higher magnification of a preparation of copper on  $\text{VSe}_2$  at  $100^\circ\text{C}$  is shown in Fig. 8.14. In this case the crystal surface was masked with a TEM grid (chapter 8.2.2). After removing the grid two different growth modes can be observed. This can be seen in the image with a higher magnification on the right hand side of the figure. The evaporated copper forms simultaneously a microstructure network (on the left) and an area with enhanced cluster growth (on the right). Between both areas the copper density is

decreased forming a depletion zone. All these features indicate a competing growth of the network and the clusters on the account of the intermediate depletion zone.

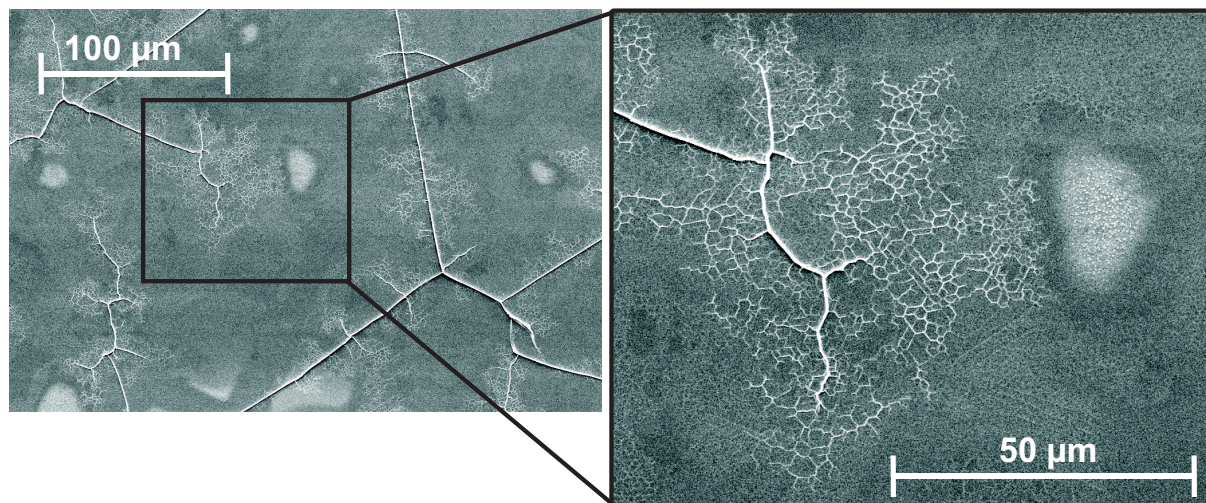


**Figure 8.14:** SEM images of  $VSe_2$  surface after copper evaporation at  $100\text{ }^\circ\text{C}$ . The nominal film thickness is about 20 nm.

Fig. 8.15 gives a more detailed view and a height profile of the edge of a depletion zone, measured by AFM. One can observe the fading out of the microstructure network until only the flat substrate is visible in the height profile.

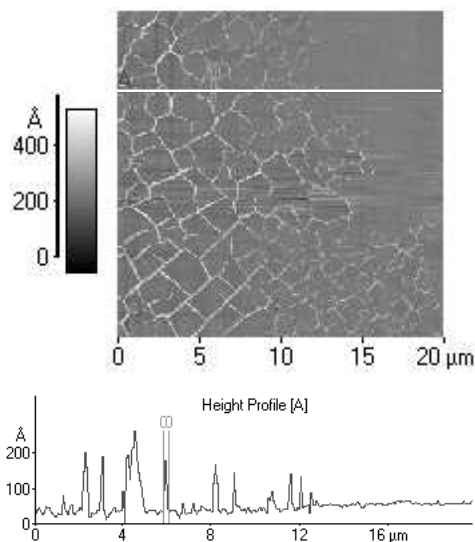


**Figure 8.15:** AFM image (contact-mode) of  $VSe_2$  surface after copper evaporation at  $100\text{ }^\circ\text{C}$ . The nominal film thickness is about 10 nm. Below the picture the height profile along the white line is depicted.

Even at a low temperature of  $-120\text{ }^\circ\text{C}$  the growth of a microstructure network takes place (Fig. 8.16). From a) to c) the magnification increases. The network is observable and

between the network the same buckles of the surface layers as in the case of TaS<sub>2</sub> appear (b) and c)).

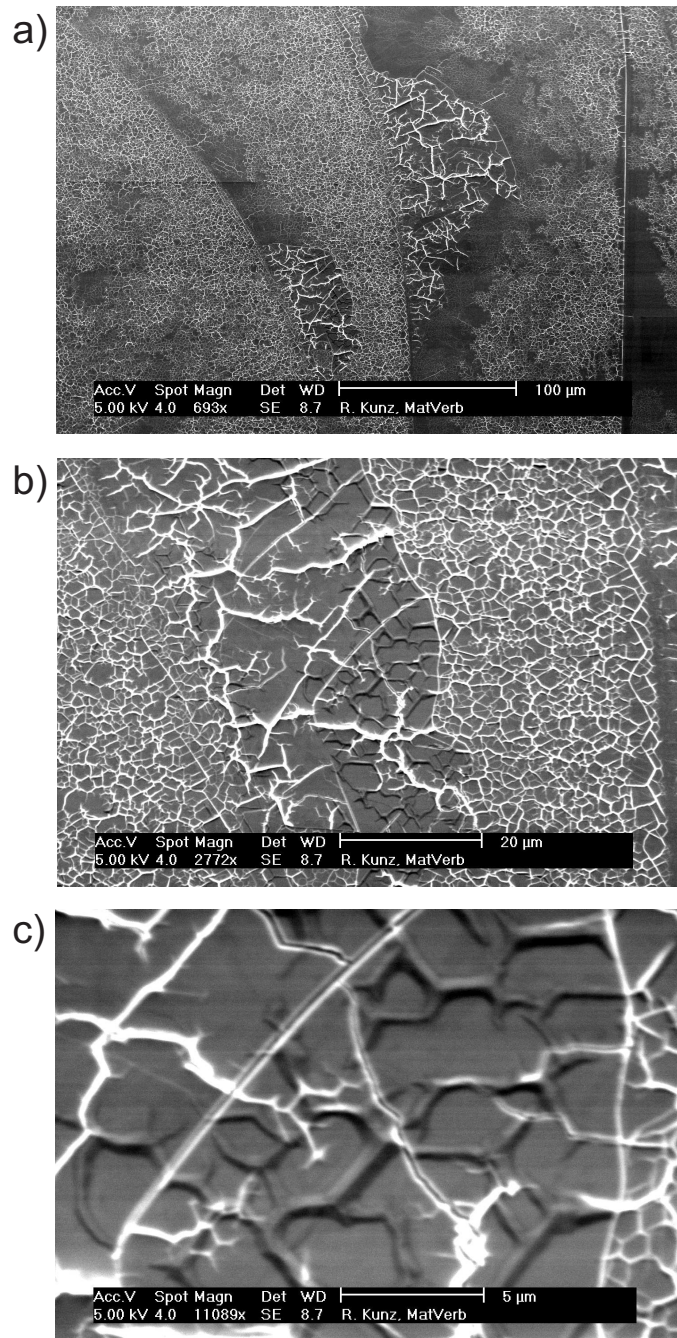


**Figure 8.16:** SEM images of VSe<sub>2</sub> surface after copper evaporation at  $-120^{\circ}\text{C}$ . The nominal film thickness is about 10 nm.

## TiS<sub>2</sub>

Fig. 8.17 shows the preparation of copper on TiS<sub>2</sub> at room temperature a) and at 100 °C b). In both cases a copper cluster growth can be found. In the case of preparation at room temperature the clusters are smaller than in the case of a substrate temperature of 100 °C. Also a depletion zone around step edges can be found like in the case of a preparation of copper on TiTe<sub>2</sub> at low temperature (see Fig. 8.7).

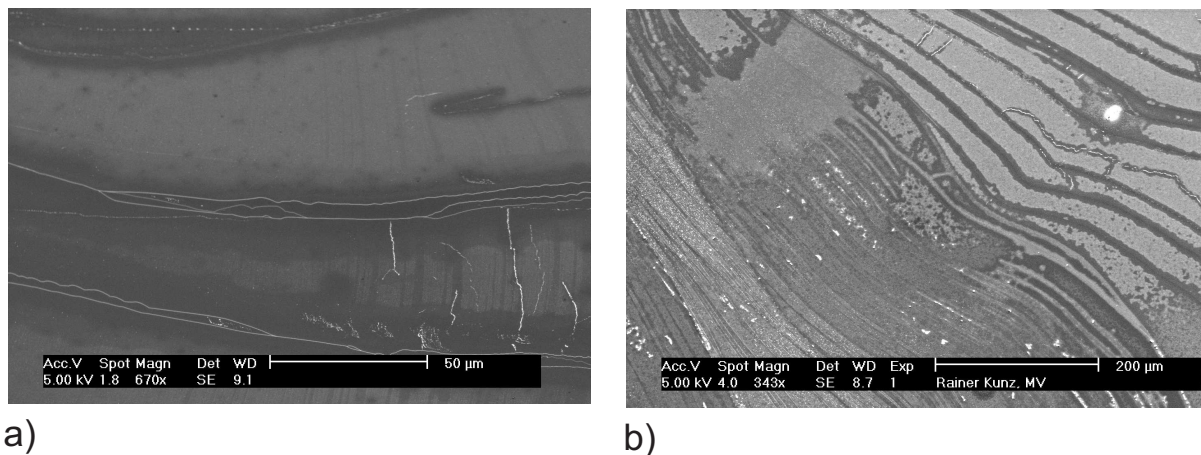


**Figure 8.17:** SEM images of TiS<sub>2</sub> surface after copper evaporation at a) RT and b) 100 °C. The film thickness is about 20 nm.

### 8.2.1 Subsequent annealing after copper deposition

As shown in chapter 8.2 the substrate temperature during the preparation has a big influence on the occurring structures. To exclude the effect of temperature changes on the occurring structures after copper deposition TiTe<sub>2</sub> and TaS<sub>2</sub> were chosen as substrates. The crystals were prepared with copper at room temperature and then annealed twice. The annealing temperature was 100 °C. The first annealing takes place for two minutes without interruption the UHV conditions after preparation. After the first annealing the samples were investigated by SEM. Then they were transferred into the preparation chamber again and annealed for 15 more minutes. SEM images of the same surface areas of the samples after the first annealing and the second one were compared.

While the substrate temperature has a big influence on the occurring structures during the preparation, especially in the case of TaS<sub>2</sub> and TiTe<sub>2</sub>, it turns out that a subsequent annealing has no effect on the once established structures. As a copper deposition on TaS<sub>2</sub> at room temperature leads to the already known microstructure network it is not observable for a preparation during substrate temperatures of 100 °C. In contrast a subsequent annealing has no effect on the already formed network which is still present after annealing as shown in Fig. 8.18. The same behavior can be observed in the case of TiTe<sub>2</sub>, where only at elevated substrate temperatures a microstructure network is observable. At room temperature no microstructure occurs as in the case of the subsequent annealing (Fig. 8.19).

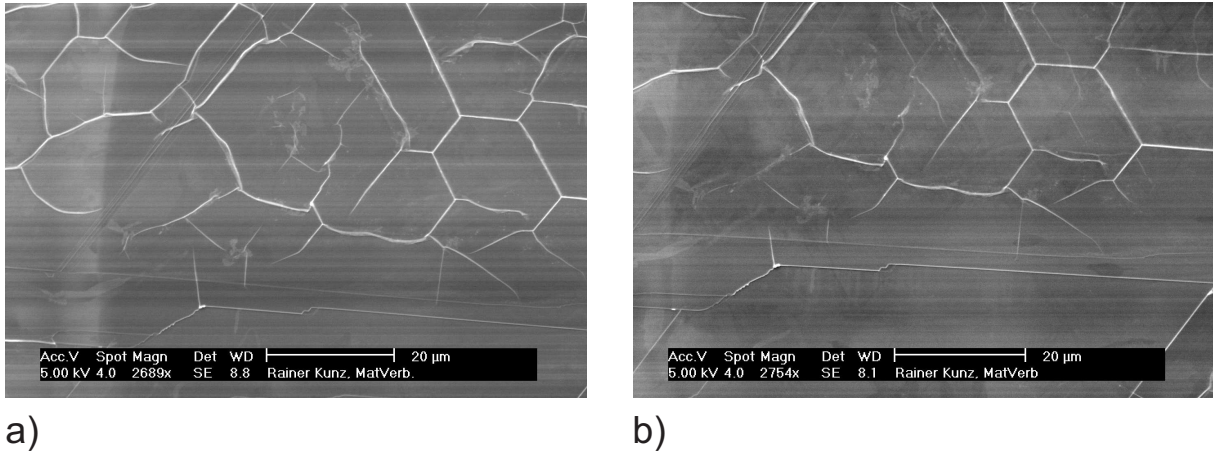


**Figure 8.18:** SEM images of TaS<sub>2</sub> surface after copper evaporation and annealing at 100 °C for a) 2 min. and b) 15 min. The nominal film thickness is about 20 nm.

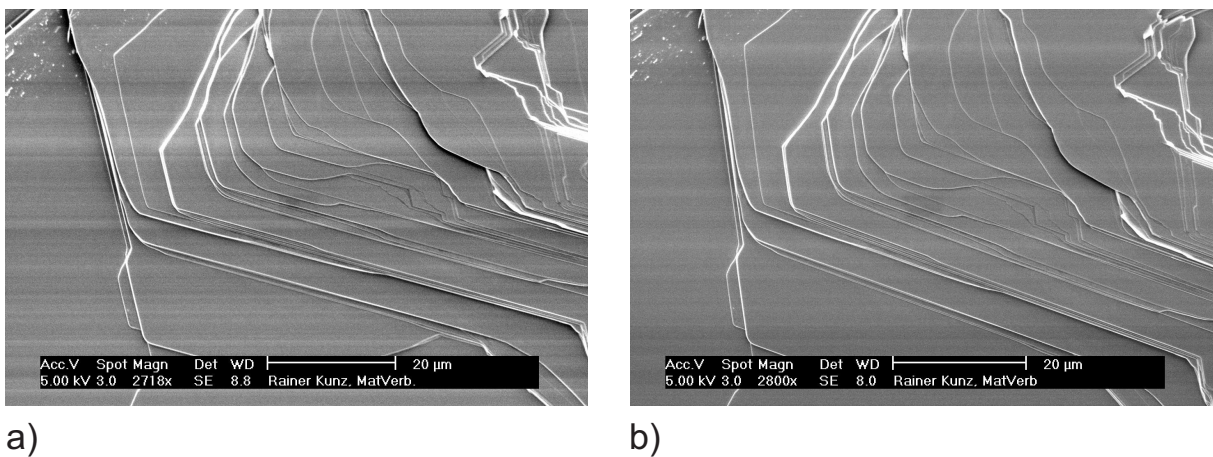


**Figure 8.19:** SEM images of TiTe<sub>2</sub> surface after copper evaporation and annealing at 100 °C for a) 2 min. and b) 15 min. The nominal film thickness is about 20 nm.

### 8.2.2 Diffusion length

The diffusion length is one of the key parameters for the understanding of the large variety of growth phenomena on different TMDC surfaces at differing conditions. Therefore, a new method for measuring the diffusion length of impinging adsorbate atoms has been established in this thesis: Air cleaved crystals were masked with copper TEM grids as shown in Fig. 8.20. The masked crystals were transferred into the UHV chamber where the copper deposition takes place. Afterwards the crystals were removed out of the preparation chamber. After the grid removal areas with deposited copper on the crystal surface are obtained. The prepared crystals can be investigated by SEM and AFM and EDX line scans can be performed. The technique of EDX line scans is a very good tool to measure the characteristic signal of deposited metal on such surfaces along certain directions. From a position where material is deposited the metal signal is measured into masked regions where no metal is directly deposited. The shapes of the masked edges are quite sharp, a shadow area can exist where metal will be deposited too. The shadow area depends on the distance between TEM grid and crystal surface. This shadow area depends on the experimental set up. Therefore, several tests on gold coated silicon wafers were performed. Since the diffusion length of copper on gold is almost zero the shadow area could be measured. The influence of this shadow area on the results is negligible as the experiments demonstrate.

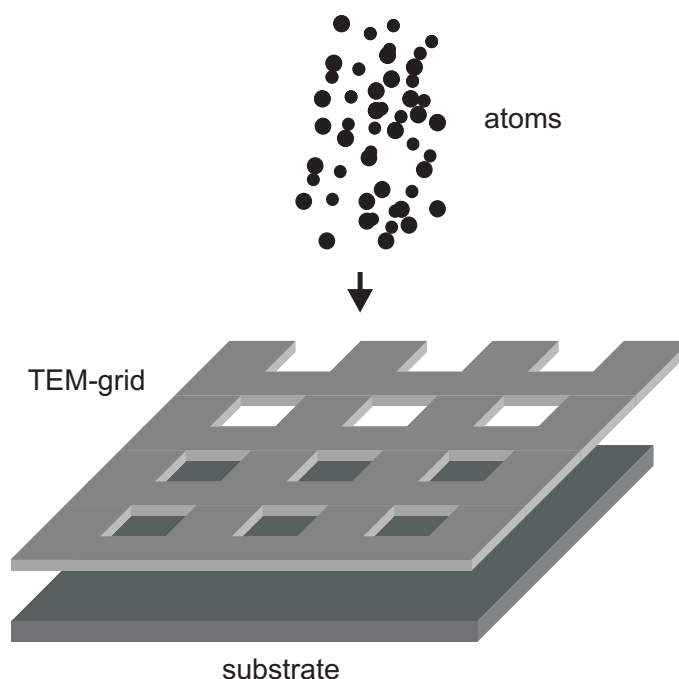


**Figure 8.20:** The masking procedure for the diffusion measurement experiments. The TEM grid can be removed after metal deposition.

The investigation of copper diffusion is shown for  $\text{WSe}_2$  as the case of homogenous thin film growth. Fig. 8.21 a) exhibits very clearly the sharp edges of the copper film next to the masked surface areas. In Fig. 8.21 b) the EDX copper signal depicted. The copper signal drops steeply at the edge of the masked area. This is an evidence for a low copper diffusion on the  $\text{WSe}_2$  surface.

The constancy of the copper signal points to the very homogenous film morphology. This



is a very good accordance to the results introduced in chapter 7.1. Here the very small copper clusters could not be resolved by SEM but they could be identified by the superior height resolution of the AFM (Fig. 7.4).

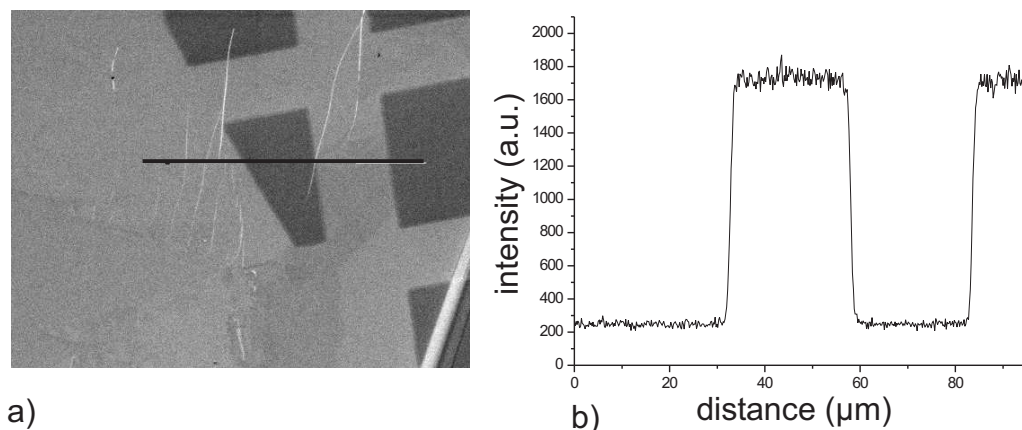


**Figure 8.21:** a) SEM image of a prepared  $\text{WSe}_2$  surface after removal of the TEM grid. b) EDX line scan of the copper L signal on  $\text{WSe}_2$  (acc.V = 5 kV) along the black line.

A similar result with respect to the diffusion length was obtained on  $\text{HfS}_2$ . In Fig. 8.22 b) the copper EDX signal possesses sharp edges and is defined as it was for  $\text{WSe}_2$ . So one can expect a low copper diffusion on  $\text{HfS}_2$  as well.

In Fig. 8.22 a) the SEM image shows that the copper cluster in the unmasked are larger than on  $\text{WSe}_2$  and their size distribution exhibits a wider variation in accordance to chapter 7.2. The more inhomogeneous copper film on  $\text{HfS}_2$  is also visible in the EDX spectra and its variability of the copper signal intensity.

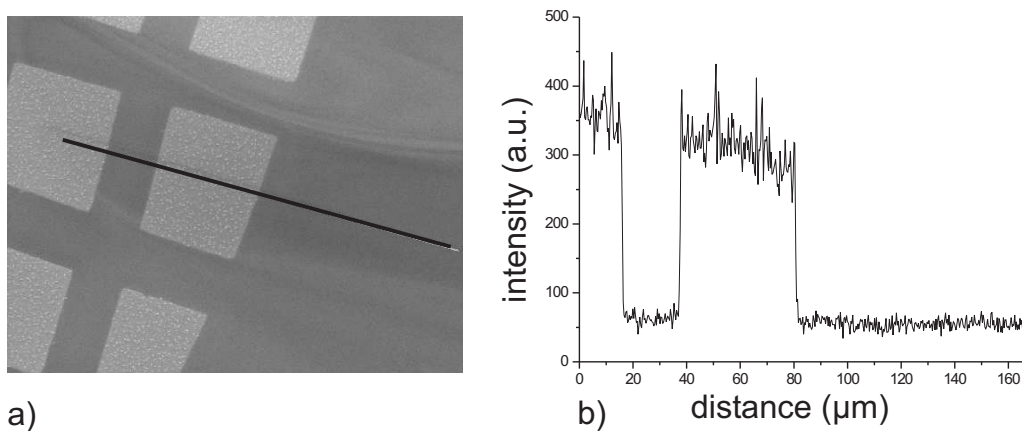


**Figure 8.22:** a) SEM image of a prepared  $\text{HfS}_2$  surface after removal of the TEM grid. b) EDX line scan of the copper L signal on  $\text{HfS}_2$  (acc.V = 5 kV) along the black line.

A completely different behavior of the copper is found on TaS<sub>2</sub> surfaces. In Fig. 8.23 a) the SEM image shows a very low material contrast between masked and unmasked areas. This can be explained by the following consideration. Different elements with a comparable atomic number have only a minor material contrast in electron microscopy (see chapter 6.2). It can be excluded in this case by the big difference of the atomic number of copper and tantalum. Thus the low material contrast must be ascribed to the copper distribution in the masked areas. Taking the preceding measurements on WSe<sub>2</sub> and HfS<sub>2</sub> into account one can state that the copper has not directly been deposited into the masked areas. The copper had to diffuse into the masked area. The requirement for such a process is a higher diffusion length of copper on TaS<sub>2</sub> in comparison to the other investigated crystal surfaces. The described effect is explicitly visible in the EDX line scan in Fig. 8.23. Contrarily to the EDX line scans on WSe<sub>2</sub> and HfS<sub>2</sub> the edges of the signal are blurred over the whole interspace of approximately 50 μm between two neighboring unmasked areas.

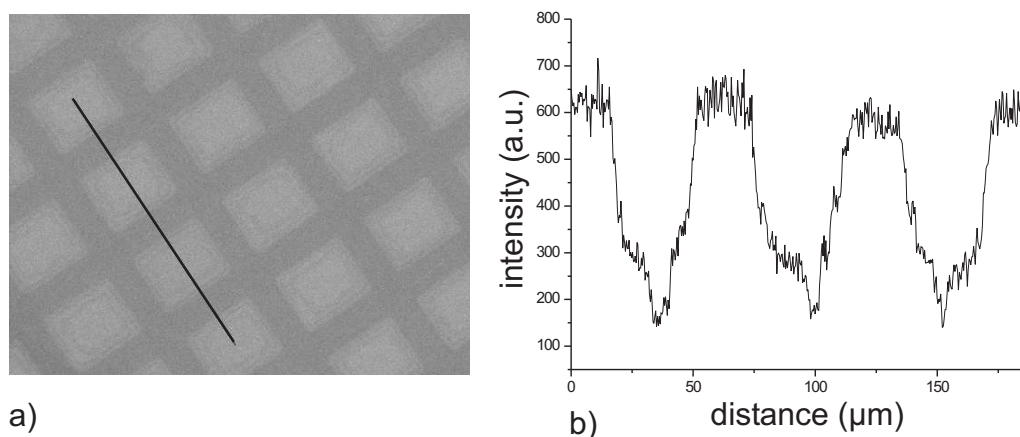


**Figure 8.23:** a) SEM image of a prepared TaS<sub>2</sub> surface after removal of the TEM grid. b) EDX line scan of the copper L signal on TaS<sub>2</sub> (acc.V = 5 kV) along the black line.

This result conforms to the measurements of the preceding chapter 7.2 where a DLA like growth of copper on TaS<sub>2</sub> at room temperature could be found. Such a growth mode requires a high diffusion length of the adsorbate atoms on the substrate. In the case mentioned here the surface was masked by other crystal layers just in the same manner as for the diffusion experiments of this chapter.

### 8.3 Substrate pre-modification by ion beam

The possibility to manipulate the surface before preparation was interesting because a growth control of the mostly self-organized structures may be adaptive for technical applications. For this experiment, TaS<sub>2</sub> was chosen as it shows the largest variety of structures. For the pre-modification of the substrate the method of material ablation by a focused ion beam (FIB) was applied. The ion beam experiments were performed at the Fraunhofer Institut für Werkstoffmechanik in Halle. The ion beam generates small butterfly structures of 2 μm diameter in the surface (Fig. 8.25 a)).

In more detail, the procedure of preparation and subsequent investigation was as follows: The crystals were prepared with a cleavage bar and then cleaved at the Fraunhofer Institut prior to prestructuring. During the whole FIB experiment the surface was monitored by SEM simultaneously.

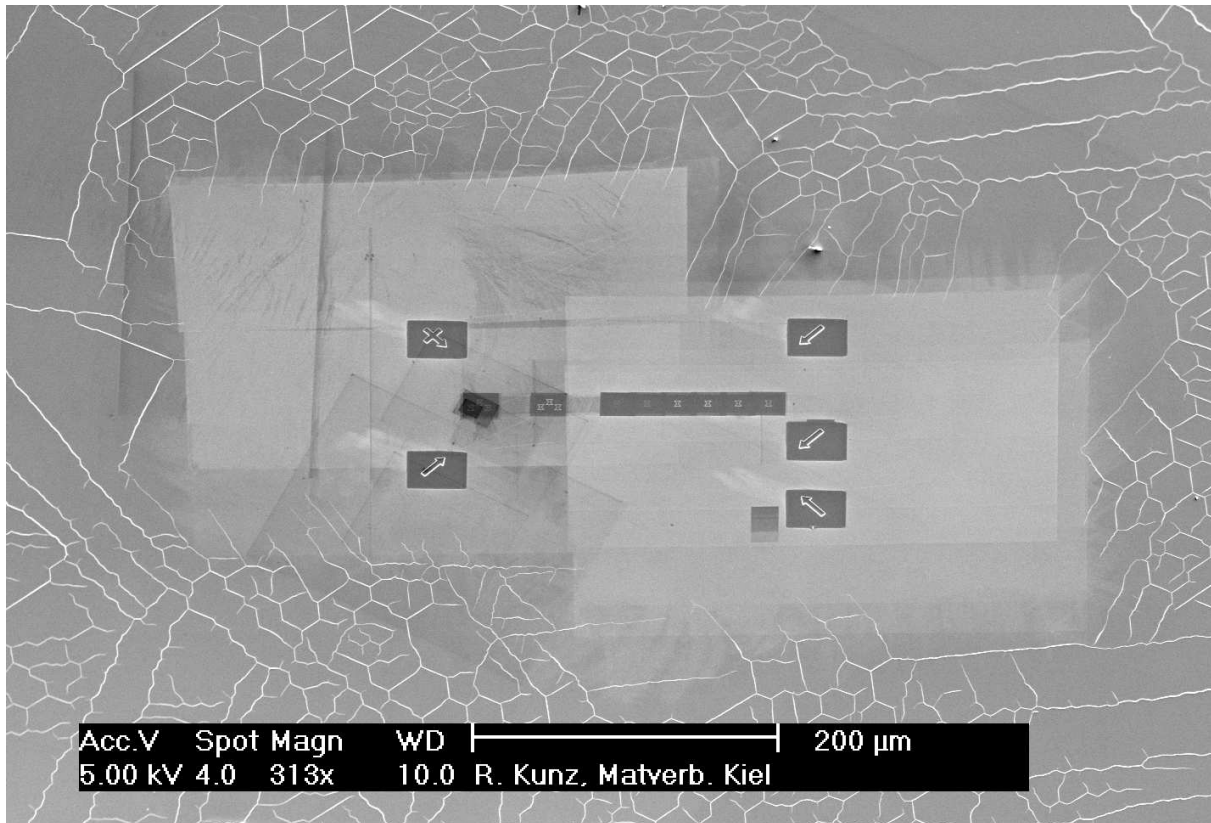


**Figure 8.24:** Overview image of the sample area. In the SEM scanned region no microstructures occur after copper deposition with a nominal film thickness of 10 nm.

The applied butterfly structures differ by their depth in the surface because the ablation time was varied from one structure to the other. The whole prepared area was marked with arrows that were applied by the same method. Finally, large scale overview SEM images were taken in order to retrieve the modified area when the samples were sent back to Kiel. The copper deposition was carried out immediately after return and the resulting surface was investigated by SEM.

Fig. 8.24 shows an overview image of the sample surface after copper deposition. Two large rectangular areas with a different image contrast can be identified as the scan region of the SEM in Halle after FIB preparation. The five smaller and darker rectangular regions contain the above mentioned arrows that point to the middle of the prepared area with the butterfly structures. Outside the modified surface regions the well known microstructure network on TaS<sub>2</sub> after copper deposition is discernable. As there are not any copper induced structures in the modified region observable the question has to be clarified whether the deposited copper remains in the FIB structured area. Fig. 8.25 b) shows an EDX spectra of the FIB structured site on the surface that is seen in Fig. 8.25 a). The copper L signal

can be identified and verifies the remaining of the copper despite the absence of discernible copper induced structures.

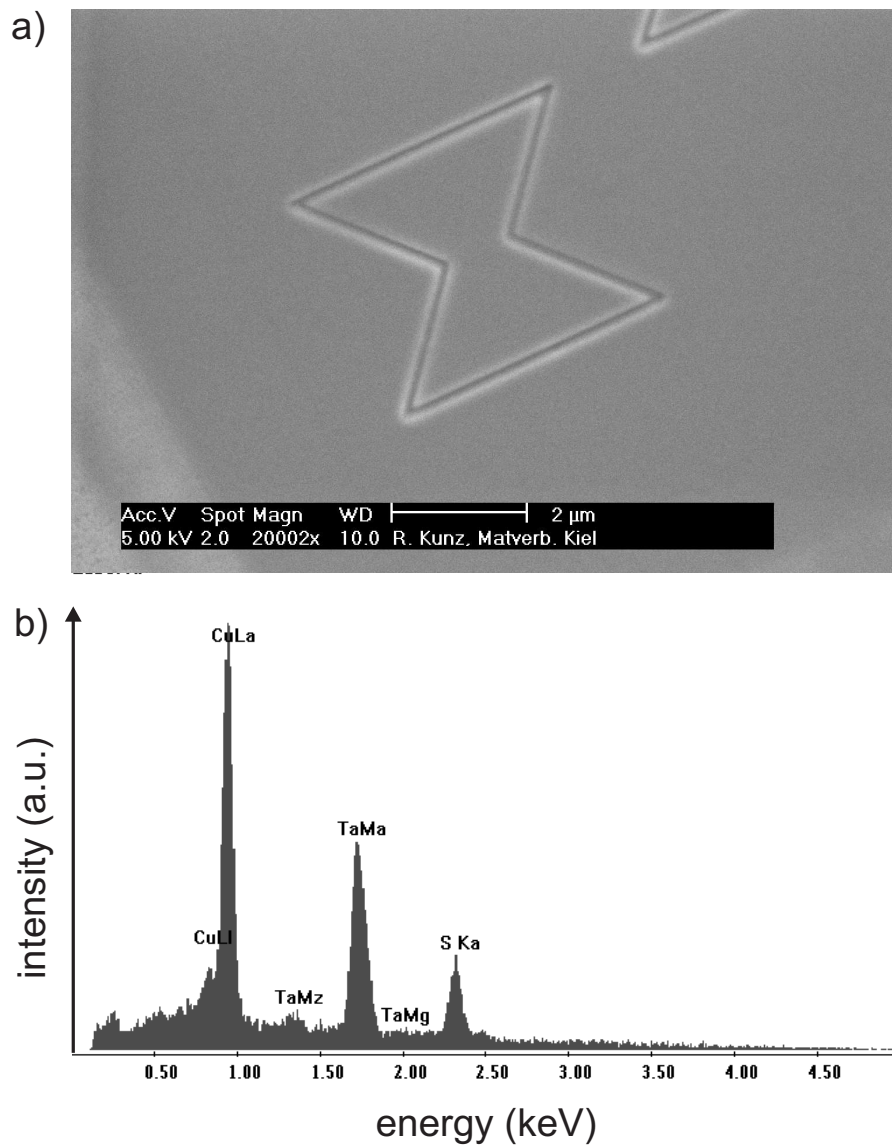


**Figure 8.25:** a) Zoom view of a butterfly structure. b) EDX-spectra of this area (acc.V = 5 kV).

In order to clarify the distribution of the copper density on the modified and unmodified area of the surface EDX line scans were performed. Fig. 8.26 a) shows the network area and next to it the modified region with one of the mentioned arrows with a darker material contrast. The white line in the image shows the EDX line scan direction. The EDX line scan of the copper L signal is shown in Fig. 8.26 b). One can observe a nearly constant copper signal in the network region that steeply increases in the darker area with the arrow. The signal decreases again just as steep when the electron beam of the SEM leaves the dark region. The noticeable fluctuation of the increased copper signal is a measurement artifact due to edge effects of the FIB structure.

The here observed growth of copper on the prestructured TaS<sub>2</sub> surface points to a contam-

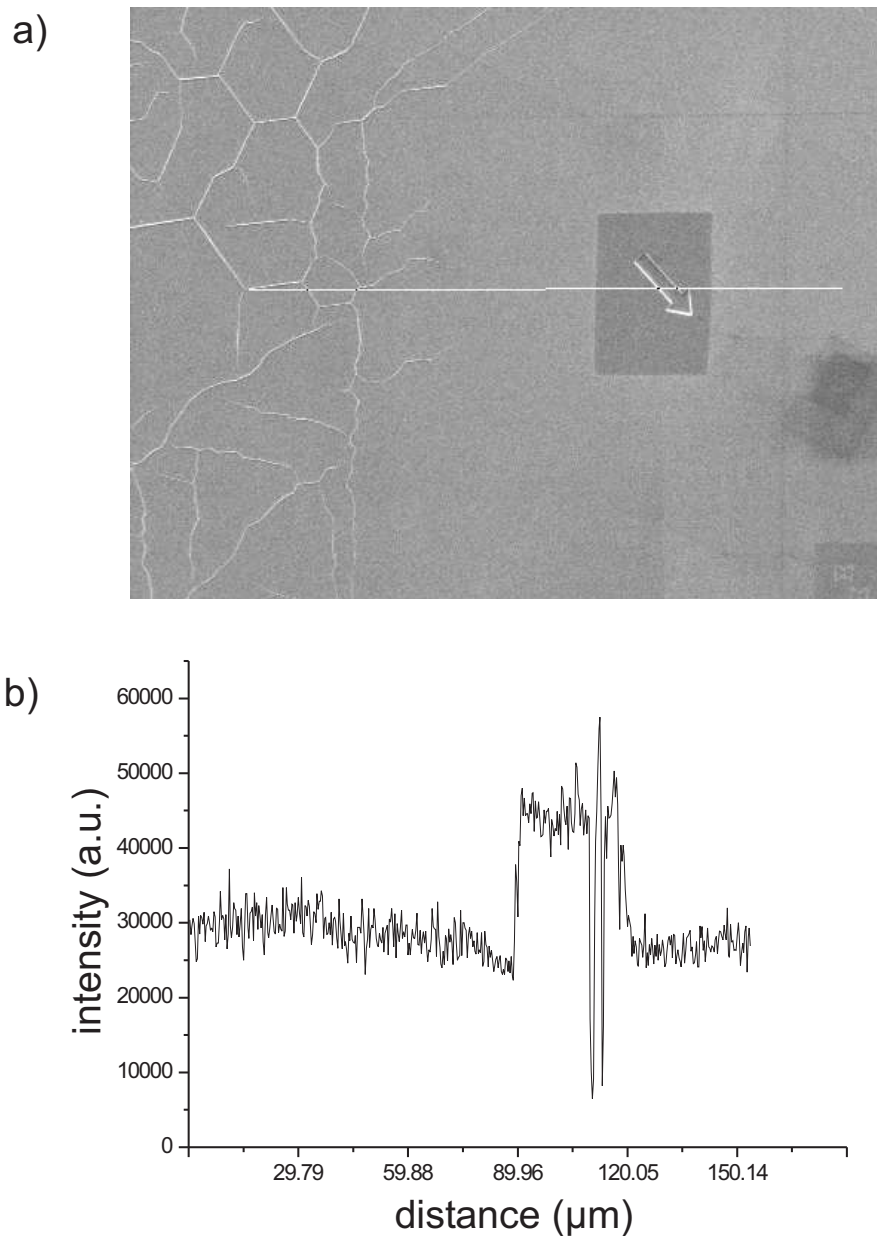


**Figure 8.26:** a) Zoom view of the border area. Along the white line in the image an EDX-linescan was performed. b) Line scan signal of the copper distribution (acc.V. = 5 kV).

ination of the surface during the FIB preparation. It is well known that the electron beam of the SEM can crack hydrocarbon molecules of the residual gas in the combined SEM/FIB chamber. The arising carbonaceous material will be deposited on top of the investigated surface (Ref. [46]). The effect of this surface deposit is generally observed as a scan rectangle. In this case the FIB preparation was monitored by SEM. The scanning area of the electron beam has a rectangular shape. One observes this shape in the here presented images. So one can expect a carbon contamination in the SEM scanned areas. The deposited copper forms the shown microstructure network in contamination free regions. In the SEM

---

monitored areas no microstructures occur. Here we have the growth of copper on a thin carbon film. The carbon signal in the EDX scan (Fig. 8.25 b) can not be resolved due to the low atomic number of carbon in respect to the high atomic numbers of copper, tantalum or sulfur. The carbon film passivates the TaS<sub>2</sub> surface for further interactions with other adsorbates. A thin film growth of copper in the contaminated areas on the TaS<sub>2</sub> surface takes place. The higher intensity of the copper L signal (Fig. 8.26 b)) in the contaminated regions with respect to the uncontaminated areas points to a higher adsorption probability of copper on the carbon film compared with the pure TaS<sub>2</sub> surface.

## 9 Discussion and conclusion

Chapter 7 and 8 have shown a large variety of structures on TMDC after metal deposition. This thesis shows that the structure formation after metal desposition is a quite more complex process than former works figured out. The entire process of structure formation on TMDC is a function of the parameters like

- the substrate
- the adsorbate
- the deposition amount
- the deposition rate
- the substrate temperature
- the adsorption probability
- the desorption probability
- the nucleation probability
- the diffusion length

and nearly always of

- the electronic (and the resulting mechanical) interaction between substrate and adsorbate

To make the whole process of structure formation more complicated, some parameter can influence each other, as depicted in Fig. 9.1.

The well defined parameters like substrate, adsorbate, substrate temperature and deposition rate can be chosen before the preparation takes place. Although the deposition rate and the substrate temperature during the preparation is kept constant, a complex interaction of substrate and adsorbate will occur. The resulting interactions of the mentioned parameters are unpredictable. Thus, the change of only one single parameter will have an influence on the other parameters and on the observable structures. Therefore, it is impossible to classify the observed structures. The system of TMDC and deposited metal varies over the whole spectra of a physically stable, indifferent or unstable system (see Fig. 9.2).

After disturbance a stable system will return to the initial state, a unstable system will switch to another state and an indifferent system will remain in its new state (Ref. [47]). This is a model to understand the complex variety of the structures occuring on TMDC after metal deposition, particularly of copper. The system TMDC and copper shows often the characteristics of a stable, a unstable and an indifferent system at the same time. Thus, a completely different growth behavior of structures can be found on only one crystal surface. Figure 9.3 shows a VSe<sub>2</sub> crystal after copper deposition through a pinhole mask. On one surface three different growth behaviors can be observed: from a network formation (region A) to a DLA like copper cluster growth (region B) up to the common growth of copper clusters (region C). The aperture of the pinhole mask was in region (A). Thus, the most

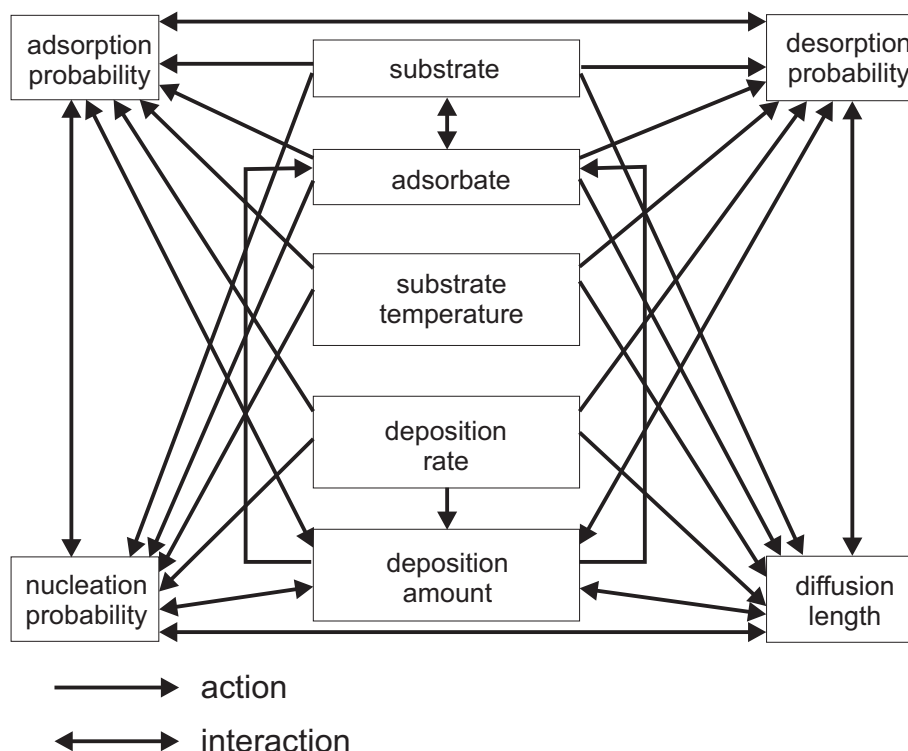


**Figure 9.1:** The possible actions and interactions of the parameters leading to structure formation during material deposition on TMDC. The schematic diagram shows the complex dependence on minor changes of single parameters.

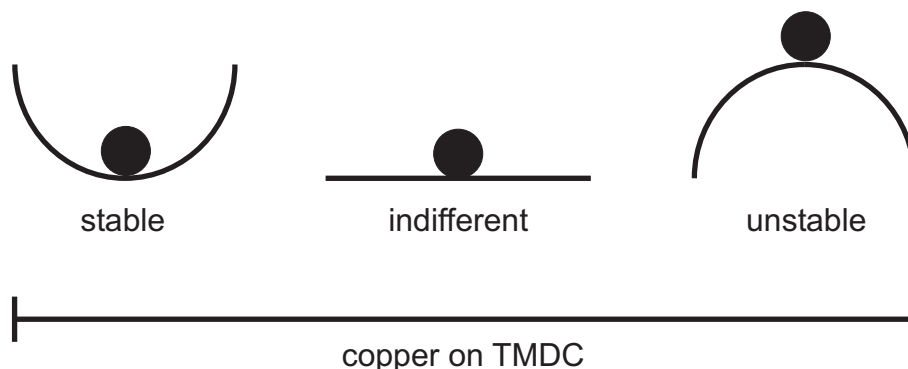


**Figure 9.2:** Schematic of a stable, indifferent and unstable system. The System TMDC/copper can not be assigned to a single system.

material was deposited in this region and a decrease of deposited material from region (A) to (C) was observed. This decrease of deposited material generates completely different structure formations on the surface.

The pure TMDC crystals seem to be situated at a transition point. An induced disturbance, e.g. the deposition of metal on the surface layers leads to a series of mechanisms which are not completely understood yet. An experimental implementation of ab initio studies of the growth phenomena is quite hard to realize. Often, it was also not possible to investigate the prepared crystals by STM or AFM. The aspect ratio of the structures or



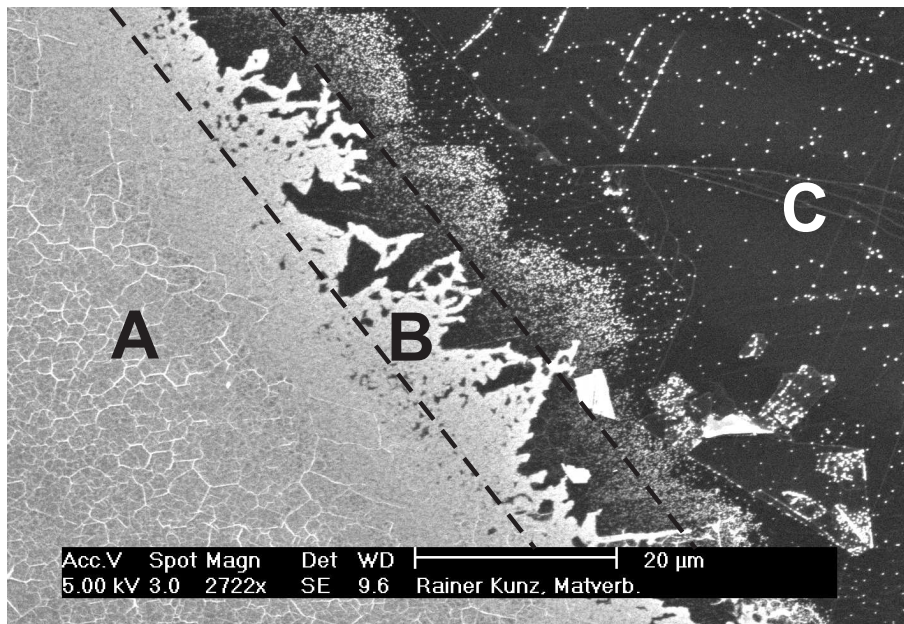


**Figure 9.3:** Structure formation on  $\text{VSe}_2$  after copper deposition. In region (A) a microstructure network, in region (B) a DLA like growth of copper clusters and in region (C) a common growth of copper clusters is observed.

of the modified crystal surface layers was above the working range of the devices. For investigations with the SEM a minimum amount of deposited copper is necessary in order to get a detectable copper signal (material contrast) for the analysis. This minimum amount (5 nm nominal film thickness) is a compromise between the minimalization of immediately intrinsic nucleation of copper atoms and the copper amount necessary for SEM investigations. Nevertheless, this nominal film thickness is still huge compared to the thickness of a single surface (triple) layer. Thus, the difference between the copper film thickness and the thickness of a triple layer is in the range of one order of magnitude. An epitaxial copper film of 5 nm thickness would consist of nearly 14 unit cells (cubic closed packed). Taking into account that each triple layer is separated by a van der Waals gap, the deposited film is more likely to show bulk character than the surface layer. In this case, the surface will be influenced by the deposited film and not vice versa. Here, the disadvantage of TMDC crystals becomes apparent. Due to the weak bondings between the triple layers the whole crystal surface is mechanically quite unstable. The advantage for investigations of diffusion processes on atomically flat van der Waals surfaces is now a disadvantage for systematic studies of adsorbate growth phenomena. Therefore, the investigation of structures obtained after metal deposition on TMDC crystals is also an investigation of the spontaneous and unpredictable mechanical failure of the substrate. In Fig. 9.4 the different kinds of mechanical failure of the crystal surface after copper deposition are depicted. The observations in this thesis have shown that the mechanical failure is caused by the interaction of substrate and adsorbate. In case (A) the surface layer can buckle, in case (B) a crack can be generated in the surface and in case (C) a crack can be formed in the buckle. The appearance of one of these defects can result in the formation of the others.

Often investigations of the sample could only be performed by SEM. In order to receive a surface sensitivity of the SEM a low acceleration voltage (5 kV) of the electron beam

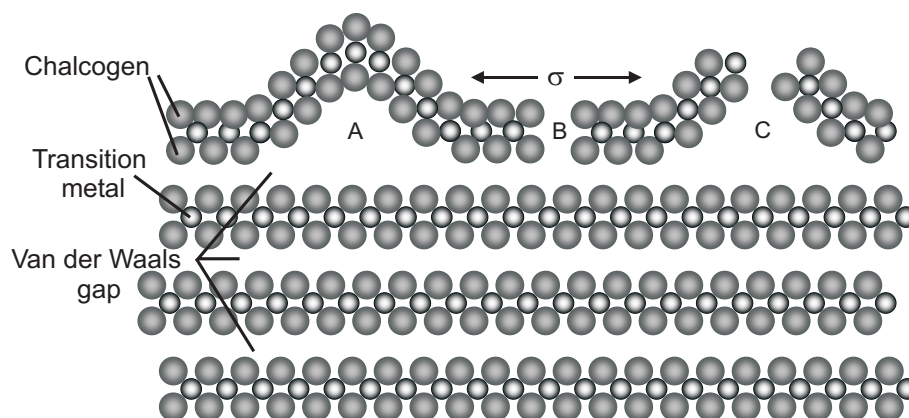


**Figure 9.4:** Schematic sketch of the surface layer failure after copper deposition and induced stress  $\sigma$ . (A) buckle, (B) crack and (C) crack in buckle.

was chosen. The low acceleration voltage leads to the disadvantage of a decreasing lateral resolution.

Among these problems, this chapter will try to discuss why the structures occur and propose some explanations. In order to discuss the structure formation on TMDC crystal surfaces after metal deposition Fig. 2.2, chapter 2, is adopted to illustrate the structure of the crystals and the processes that can occur on TMDC surfaces, shown in Fig. 9.5.

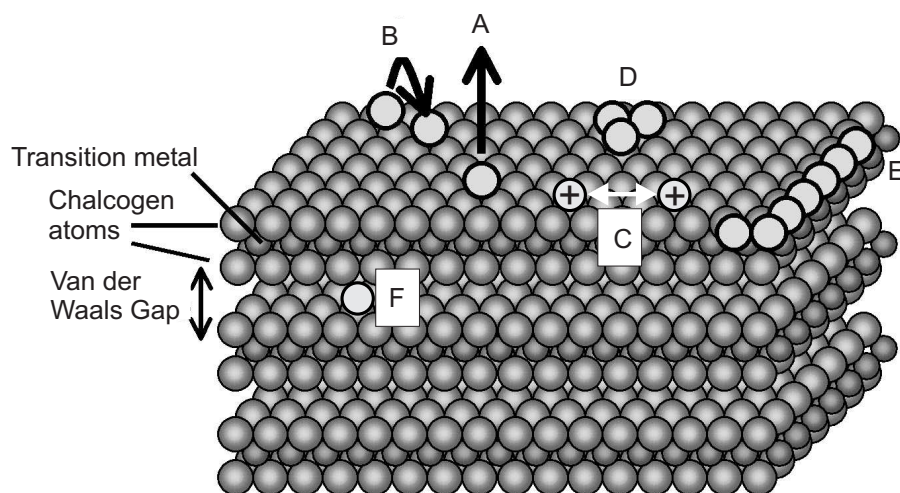


**Figure 9.5:** Structure of a layered transition-metal dichalcogenide (TMDC) crystal and possible kinetics of adsorbate atoms. The crystal consists of triple layers, each composed of transition metal atoms in the middle and chalcogen atoms on top and below. The layers are held together by weak van der Waals forces. Surface processes of the adsorbate atoms are: (A) Desorption, (B) hopping from one position to another on the surface, (C) repulsive interaction of charged adsorbate atoms, (D) intrinsic nucleation of several adsorbate atoms to a cluster, (E) extrinsic nucleation on a step edge where unsaturated bonds are and (F) intercalation into the van der Waals gap.

Atoms can move around (B) by overcoming the diffusion barrier  $E_d$  on the surface, which are typically small (meV range) so that there is a high mobility at room temperature [48]. Diffusion is limited by at least three different processes: One is desorption (A) as there is a finite probability for the atom to leave the sample. The other processes are intrinsic nucleation of copper atoms (D) and extrinsic nucleation (E) at step edges or crystal defects. Calculations done in the framework of the DFG Forschergruppe FOR 353, *Chalkogenid Schichtstrukturen: Wachstum und Grenzflächenphänomene*, contained information about the energetic processes of alkali metal diffusion and intercalation on TMDC crystals. The direct intercalation (F) of alkali metal atoms into the van der Waals gap without any defects is not very probable due to the high energy barriers [49]. A charge transfer from the adatoms into the surface layers of the TMDC crystal can generate a dipole (C) of diffusing metal adatoms.

In order to explain the observed structures the influence of the

- defect density of the substrate surface
- interaction of adsorbate and substrate
- substrate temperature on the received structures

will be discussed. Here, the focal point is on the different growth phenomena. Due to the large interconnection of every single parameter (see first listing in this chapter) the limits of single aspects, e.g. defect density of the substrate surface, overlaps with nearly every other aspect.

### Defect density of the substrate surface

The low defect density of the cleaved crystals does hardly provide any nucleation centers for the adsorbants and can not explain any structure reconfiguration except for structures at step edges. On the defect free surface one would expect a thin film growth of clusters in a Volmer-Weber mode. We observed such a growth of copper on  $\text{WSe}_2$ . The copper clusters are distributed homogeneously over the surface.

Step edges will serve as nucleation centers for diffusing adatoms. Often a depletion zone of the copper cluster density around step edges can be observed. Step edges offer access to the van der Waals gap for diffusing adatoms (see Fig. 9.5). Calculations [50] for lithium on  $\text{TiSe}_2$  point out stable structures for Li at the octahedral site in the van der Waals gap. So diffusing adatoms will nucleate either with other diffusing adatoms or at step edges. The width of the depletion zone can serve as an appraisalment of the diffusion length. For a deposition of copper on  $\text{TiTe}_2$  at  $T_{sub} = 100^\circ\text{C}$  one finds depletion zones in the range of 200 nm.

Silver sputtering on  $\text{TiS}_2$  generates triangular structures decorating step edges while the surface shows a dewetting effect of the silver film. This points out the different character of surface and step edge. In this case at step edges crystalline structures following the crystal symmetry of the substrate can be observed while the surface of the crystal shows a "silverphobic" character.

Crystalline adsorbate structures can also be observed for evaporated chromium on  $\text{TaS}_2$ . Needle shaped structures orientated in three angles grow on the crystal surface. Defects

of the surface as a motivation of the needle growth can be excluded as investigations have shown no hints on any defects. In this case the crystal symmetry can be the presetting for the growth mode.

On  $\text{TiTe}_2$  geometrically arranged clusters can be observed after copper deposition. These structures are quite difficult to explain. Though a Volmer-Weber like growth mode takes place, the cluster arrangement is of a high order over large areas of the crystal (several 100  $\mu\text{m}$ ) and follows the crystal symmetry. There are no step edges or other defects on the surface that could explain the structures. Defects in the bulk layers like stacking faults etc. are difficult to detect experimentally.

Copper deposition on  $\text{TaS}_2$  generates fractal shaped structures characteristic for a DLA like growth mode requiring a large diffusion length and a low nucleation probability. Dendritic growth of crystals is a rather common phenomenon in nature, but it is an exception in UHV vapor deposition experiments. Anton et al. found a dendritic growth for Au particles on highly pyrolytic oriented graphite and estimated the mean diffusion length of adatoms to about 400 nm (Ref. [51, 52]). Till now, larger diffusion lengths in the range of several 100  $\mu\text{m}$  are only observed in liquid films under vapor deposition (Ref. [53]). Thus, the large diffusion length of copper atoms on  $\text{TaS}_2$  is extraordinary.

### Interaction of adsorbate and substrate

Further experimental (Ref. [54–59]) and theoretical works (Ref. [49, 60]) studied the adsorption and intercalation of alkali metals on TMDC surfaces. The intercalation into the van der Waals gap was one aspect as well as the possibility to change the electronic and geometric properties of the substrate. Calculations have shown that the intercalation perpendicular through the surface of a TMDC into the van der Waals gap requires several eV. A deposited atom does not possess the required energy. The high value of the intercalation barrier suggests that the most probable path of intercalation is through the edges or defects of the crystal. So other mechanisms must take place on the surface after metal evaporation. In Ref. [54] the occurring structures were presented, problems and models were suggested according to the calculations in Ref. [49]. As a result of these studies the diffusion of adsorbants was found to be one of the most important points. For a diffusion process the adsorbate atom has to overcome the diffusion barrier  $E_d$ . The diffusion barrier  $E_d$  is the difference in energies between to different sites on top of a TMDC surface. Calculations for alkali metals on  $\text{TaSe}_2$  (by Ramírez) yields typical values for diffusion barriers as shown in Table 9.1

Alkali Metal	$E_d$ in meV	Atomic Radius in pm
Li	260	152
Na	120	186
Rb	60	248
Cs	10	265

**Table 9.1:** Typical values for the calculated diffusion barriers  $E_d$  for different alkali metal atoms on  $\text{TiSe}_2$  [49]. The atomic radius of the different alkali atoms is also given.

The diffusion barrier depends also on the atomic radius of the adsorbed alkali metal. With decreasing atomic radius the diffusion barrier increases. The ion radius for the alkali metals

and copper are given in Table 9.2

Charge	Radius in pm
Li <sup>+</sup>	68
Na <sup>+</sup>	97
Rb <sup>+</sup>	147
Cs <sup>+</sup>	167
Cu	128
Cu <sup>+</sup>	96
Cu <sup>2+</sup>	72

**Table 9.2:** The radius of the different alkali ions and of copper.

Lithium has the smallest atomic and ion radius and the highest diffusion barrier on TaSe<sub>2</sub> compared with the other alkali metals. The atomic radius of copper (128 pm) is smaller than the atomic radius of lithium (152 pm) so one could expect a higher diffusion barrier for copper. Calculations of the diffusion barrier for copper on TMDC are quite difficult because of the number of valence electrons. Therefore, alkali metals were chosen for the experiments and calculations in Ref. [54], Ref. [61] and Ref. [49]. The high reactivity of alkali metals exposed to air makes investigations at surrounding conditions impossible. Copper will not react like alkali metals and is of much more interest for technical applications. The calculations for the alkali metals will serve as a model for the diffusion behavior of copper. In chapter 7 and 8 we observed large diffusion lengths of copper on TMDC. In the case of copper on WSe<sub>2</sub> and HfS<sub>2</sub> the grid masked crystal surfaces possess sharp edges. The most extreme example for diffusion of copper on TMDC is TaS<sub>2</sub>. In chapter 8 the diffusion length was measured by masking the crystal with TEM grids. For copper a diffusion length of 50  $\mu\text{m}$  at room temperature was measured on the TaS<sub>2</sub> surface (Fig 8.23). The large diffusion length of copper on TaS<sub>2</sub> points at a very low diffusion barrier and nucleation probability compared with the diffusion of copper on other TMDC surfaces. In order to understand this phenomenon we want to take other properties of the adsorbate metals into account.

Metal	Electronegativity
Cu	1,90
Li	0,98
Na	0,93
Rb	0,82
Cs	0,79

**Table 9.3:** Electronegativity of the different alkali metals and of copper.

In Table 9.3 the electronegativity of alkali metals and copper are depicted. The electronegativity and an occurring dipole of the adsorbed metal are of interest. So it is much more probable for alkali metals to donate the valence electron to the substrate than for copper. The donation of electrons to the TMDC crystal induces a lattice distortion of the first surface triple layer. The ionic adsorbate metal reacts as a dipole. A repulsive interaction with other single metal ions will follow. If the amount of deposited metal atoms reaches a

critical value the accumulated metal atoms will exhibit a metallic behavior and electrons from the substrate will be transferred back to the adsorbed metal. The surface triple layer will contract and its surface will buckle or crack by the stress (see chapter 3). The cracks are nucleation centers for diffusing adatoms and one can observe a microstructure network growth of metal adatoms building clusters. The formation of a microstructure network always coincides with the destruction of the surface layers. One can observe this behavior at very low and at room temperature for copper on  $\text{TaS}_2$  and  $\text{VSe}_2$ . Often TMDC possess a charge density wave (CDW) which is a periodic modulation of the electron density. The CDW is always associated with a periodic lattice distortion with the same wave vector. Especially two dimensional systems are susceptible for this kind of lattice instability. Among the TMDC  $\text{TaS}_2$  and  $\text{VSe}_2$  exhibit a transition to the CDW phase at or relatively close to room temperature ( $\text{VSe}_2$ :  $T_{CDW} = 110 \text{ K}$ , [62]). This is a further example for the instability of the geometric structure of the TMDC substrates upon changes of the electronic structure.

Copper preparation at elevated temperatures shows that the network vanishes completely on  $\text{TaS}_2$ . It can still be observed on  $\text{VSe}_2$ . New is the network formation during copper deposition at elevated temperatures on  $\text{HfS}_2$  and  $\text{TiTe}_2$ . So we want to take the substrate temperature as an new factor for the growth mechanism into account.

### Substrate temperature influence on the obtained structures

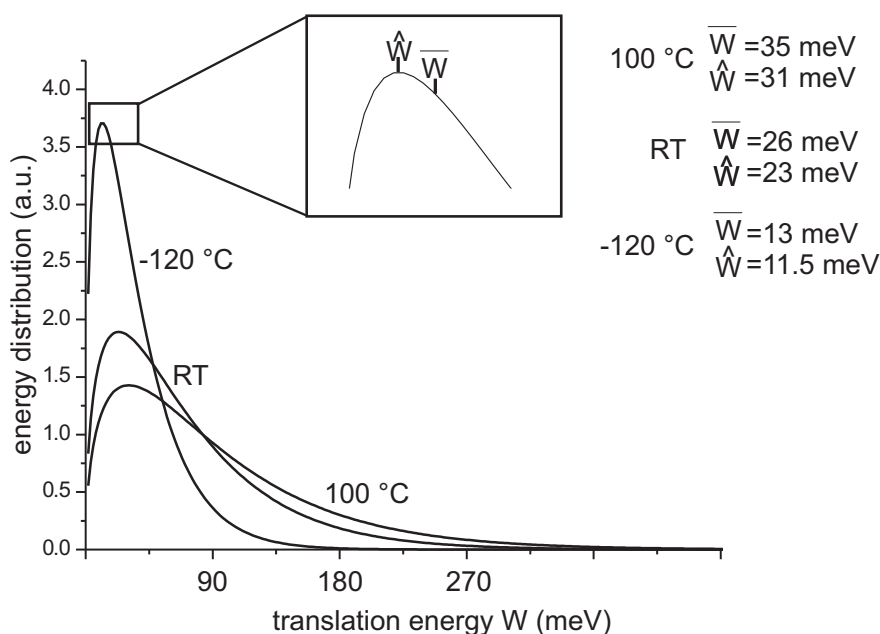


**Figure 9.6:** Maxwell-Boltzmann energy distribution at three different temperatures for a single particle with two degrees of freedom. For each temperature the medium  $\bar{W}$  and the most probable energy  $\hat{W}$  of the particle are listed.

In Fig. 9.6 the Maxwell-Boltzmann energy distribution is depicted. It was calculated assuming a single particle (e.g. an atom) with two degrees of freedom diffusing on top of a surface. The translation energy of the particle is provided by the temperature of the surface. We further presume that there is no interaction between the particle and the

substrate. For three different temperatures the most probable energy  $\hat{W}$  and the average energy  $\bar{W}$  of the particle are calculated. As one would expect the energies increase with elevated temperatures. The curve progressions for the energy distribution at 100 °C and room temperature (RT) are comparable in the energy range between 90 meV and 270 meV. Here the number of particles on this energy regime is still significantly high. On the other hand the energy distribution curve at -120 °C indicates a rapid decrease of the particle number with an energy of at least 90 meV. For -120 °C the most probable translation energy  $\hat{W}$  of the particle is 11.5 meV and the medium energy  $\bar{W}$  is 13 meV. The corresponding calculated values for RT and 100 °C are increased by a factor of two and three respectively. The progressions of the Maxwellian tails of the three curves show the largest difference. At -120 °C the Maxwellian tail shows a fast decrease of the translation energies ending at a maximum value of  $\approx 200$  meV. At elevated temperatures there is a large number of particles with higher translation energies. As one can see in the energy distribution for RT and for 100 °C, there is still a high number of atoms with a translation energy of 200 meV. This calculation is a simplification of the true circumstances. With respect to the two-dimensional character of the TMDC crystals it can give an idea of the energetic relationship of the diffusion process, e.g. diffusion barriers. If one compares the values for the diffusion barriers in Table 9.1 with the translation energies in Fig. 9.6 one finds that they are in the same range. So the substrate temperature during preparation will have a large influence on the diffusion length of adsorbed metal on the TMDC surface. As shown in chapter 8 for the TaS<sub>2</sub> and TiTe<sub>2</sub>, copper deposition at different temperatures leads to different structures. TaS<sub>2</sub> and TiTe<sub>2</sub> have shown an inverted behavior. At a substrate temperature of RT copper deposition on TaS<sub>2</sub> generates a microstructure network by mechanical failure of the crystal surface layers. As already mentioned this network can not be observed at elevated temperatures (100 °C) on TaS<sub>2</sub>. That yields to a change of the fracture mechanics of the crystal with regard to different temperatures. At elevated temperatures it has to come to a reduction of the stress in the surface layers which is induced by the adatoms. Even the stress (lattice distortion of the surface layers) between surface and bulk layers can be reduced. The surface layers can slide freely over the bulk layers. On the defect free surface a thin film growth of copper clusters (Volmer-Weber growth) can take place. For crystals like TiTe<sub>2</sub> and HfS<sub>2</sub> one can observe a microstructure network after metal deposition **only** at elevated temperatures. In this case the higher temperature has to degrade the structural stability of the surface layers. Just a little bit stress induced by the adatoms and the resulting lattice distortion can be sufficient to destroy the surface layers. Thereby the cracks and buckles follow the hexagonal crystal symmetry. It denotes that the binding along neighboring Wigner-Seitz-cells is not as stable as within the cell. Even though the energy insertion by the substrate temperature during the preparation at 100 °C is only in the range of  $\approx 10$  meV, the influence of the temperature on the occurring structure is enormous. A subsequent annealing has no effect on the once established structures. So the energy insertion by the temperature for a structure reconfiguration is too low.

## 10 Summary

The starting point of this thesis was the observation of a few unusual structures resulting from alkali metal deposited onto TMDC surfaces, see for example Ref. [54] and Ref. [61]. Until today, there is a lack of a systematic investigation and a categorization of the different structures, although this is a fundamental requirement for understanding the mechanisms standing behind these growth phenomena and thus making them eventually accessible for technology.

In order to contribute to overcome this deficiency, different self organization phenomena of various metallic adsorbates on transition metal dichalcogenide crystal surfaces were studied in a systematic manner, with the aim to describe the observed structures and to understand the basic organization mechanisms after metal deposition.

Besides the application of microscopy techniques for characterization of the geometry of the surfaces, it was necessary to investigate the material distribution on the surface. Therefore, EDX line scans recording the characteristic material signals were established as a powerful measurement technique. The energy insertion into the substrate and adsorbate due to varying substrate temperature was discussed in respect to the experimental observations and theoretical calculations.

TMDC crystals are a prominent material class due to their pronounced two-dimensionality, their very flat and inert surface and the large variety of different TMDC crystals. They all show the same set-up of stacked triple layers with van der Waals gaps between them. Nonetheless, they differ with respect to their electronic behavior (semiconducting and metallic), the lattice constants and the exact stacking of the layers. Thus, the substrate was the first parameter that could be varied over a large range of different TMDC crystals.

The second variation parameter for the examination is the adsorbed metal species. While former investigations were restricted more or less to alkali metals (Ref. [49, 54, 61]) the focus during this thesis was shifted to technological relevant materials like chromium, silver and copper.

In order to fulfill these targets it was essential to create an environment that allows reproducible evaporation of different metals in a well defined manner. Therefore, the exact control of the evaporation rate and the evaporated amount of material is as essential as an extremely pure environment. For this purpose an UHV preparation chamber was constructed which allows evaporation at rest gas pressures down to  $10^{-10}$  mbar, the simultaneous insertion of several samples and a sample storage under UHV conditions.

By varying only those two parameters (substrate and adsorbate) one already received an overwhelming variety of different surface structures ranging from thin film growth over cluster growth, diffusion limited aggregation to the formation of microstructure networks, oriented growth of needles and very complicated geometrical structures. Some of these structures, like the growth of metal clusters on the surface can be easily understood with well established surface growth models and can be observed in a similar manner on other crystals. Other structures, like e.g., nanostructure networks were not observed after metal evaporation on any other surface than on layered crystals. Regardless of the complexity of the structures the type of structure could always be reproduced when performing the



evaporation under the same conditions.

Due to this very large variety of different structures, it was necessary to restrict the further investigations to the most relevant metal which is copper. On the one hand copper is extensively used in semiconductor technology. On the other hand copper evaporation has created the most complex structures on TMDC crystals. The deposited amount of copper on different TMDC crystals was varied in order to understand the effect of the different film thicknesses on the occurring structures. It could be shown that the size of the nano- and microstructure networks increases with increasing film thickness.

The preparation chamber allowed the variation of the substrate temperature during metal deposition and the temperature dependence of the structures was investigated. It turned out that there is a big influence of the substrate temperature on the growth of copper on TMDC. For the same substrate and adsorbate materials completely different surface structures were observed for deposition at moderate temperatures as compared to structures formed at higher temperatures.

The possibility to control the structure growth by prestructuring of the surface was examined as a further new aspect. It was demonstrated that the contamination of the surface during the prestructuring process eliminates any characteristic growth modes resulting from the nature of the TMDC crystals.

The unusual variety of new growth phenomena on the layered crystals could be found to be based on mainly two effects. The first effect is caused by the large variation of the diffusion length for different substrates under the same growth parameters, which is ranging from a few nanometers to more than 50 micrometer. The second effect is the influence of the adsorbate on the substrate structure. Structures of mechanical failure in the surface layer indicate large stress differences between the surface and the bulk of the crystals after metal evaporation. With increasing film thickness, not only the complexity but also the degree of the surface destruction increases.

On the one hand, the two dimensional character and the inert surfaces of TMDC crystals are a good model system to investigate diffusion and growth processes. In this thesis it could be shown that there is even for non-alkali metals a large variety of structures that can form after metal deposition. Systematic experiments and investigations with different methods were performed by varying the deposition parameters and new measurement techniques were established. On the other hand, the interaction between adsorbate and substrate restructures the surface, leading to mechanical failure. These structures were determined to occur abrupt if a certain level of stress was reached. The relaxed surface structure might lead to a changed interaction between adsorbate and substrate, e.g., with respect to nucleation. These complex interactions make the examination of the layered crystals after metal evaporation more difficult than examination of conventional growth.

Nevertheless, from a technological point of view, the restructuring of thin films by mechanical failure has led to applications. By transferring mechanisms that occur on the layered crystal surface to thin films, it was possible to fabricate nanowire networks in a well controlled manner, see *Nat. Materials* (Ref. [63]).



## References

- [1] *The international roadmap for semiconductors, Edition 2003, executive summary, Internet document: <http://public.itrs.net/>.*
- [2] Y. Xia, P. Yang, Y. Sun, Y. Wu, B. Mayers, B. Gates, Y. Yin, F. Kim and H. Yan: *One-Dimensional Nanostructures: Synthesis, Characterization, and Applications*. Adv. Materials **15**, 353 (2003).
- [3] R. Adelung, R. Kunz, F. Ernst, L. Kipp, M. Skibowski: *Self-Organized Structures on Flat Crystals: Nanowire Networks Formed by Metal Evaporation*. Advances in Solid State Physics 43 (Ed. B. Kramer), Springer, Heidelberg (2003).
- [4] Scott A. Chambers: *Epitaxial growth and properties of thin film oxides*. Surface Science Report **39**, 105 (2000).
- [5] Adolf Fick: *Über Diffusion*. Annalen der Physik **1** (1855).
- [6] John A. Venables: *Atomic processes in crystal growth*. Surface Science **299/300**, 798 – 817 (1994).
- [7] E. Bauer: *Phänomenologische Theorie der Kristallabscheidung an Oberflächen*. Zeitschrift für Kristallographie (1958).
- [8] J. A. Venables: *Thin films: Heteroepitaxial Systems*. World Scientific, Singapore (1999).
- [9] E. Bauer and Jan H. van der Merwe: *Structure and growth of crystalline superlattices: From monolayer to superlattice*. Phys. Rev. B **33**, 3657 (1986).
- [10] T. A. Witten and L. M. Sander: *Diffusion limited aggregation, a kinetic critical phenomena*. Phys. Rev. Lett. **47**, 1400 (1981).
- [11] T. A. Witten and L. M. Sander. *Phys. Rev. B* **27**, 5686 (1983).
- [12] P. Bourke. <http://astronomy.swin.edu.au/pbourke/fractals/dla/> (2004).
- [13] T. A. Witten and P. Meakin. *Phys. Rev. B* **28**, 5632 (1983).
- [14] E.E. Krasovskii, Persönliche Mitteilungen.
- [15] M. Traving. *Ph.D. thesis, Inst. f. Exp. u. Ang. Phys. der CAU Kiel* (1999).
- [16] C. Kreis: *Epitaxie von  $HfS_2$  auf  $WSe_2$ : Wachstum und elektronische Struktur*. Diplomarbeit, IEAP CAU Kiel (1998).
- [17] A. G. Evans and J. W. Hutchinson: *The thermomechanical integrity of thin films and multilayers*. Acta Metall. Mater. **43**, 2507–2530 (1995).
- [18] V. K. Tolpygo, J. R. Dryden and D. R. Clarke: *Dermination of the growth stress and strain in  $\alpha - Al_2O_3$  scales during the oxidation of  $Fe - 22Cr - 4.8Al - 0.3Y$  alloy*. Acta Mater. **46**, 927–937 (1998).

- [19] W. D. Nix: *Mechanical properties of thin films*. Metall. Trans. **20A**, 2217–2245 (1989).
- [20] Q. Ma and D. R. Clarke: *Stress measurement in single-crystal and polycrystalline ceramics using their optical fluorescence*. J. Am. Ceram. Soc. **76**, 1433–1440 (1993).
- [21] H. Tada, P. C. Paris and G. W. Irwin: *The Stress Analysis of Cracks Handbook*. Del Research, St. Louis, Missouri (1985).
- [22] J. W. Hutchinson and Z. Suo: *Mixed-mode cracking in layered materials*. Advances in Applied Mechanics **29**, 63–191 (1992).
- [23] D. K. Leung, M. Y. He and A. G. Evans: *The cracking resistance of nanoscale layers and films*. J. Mater. Res. **10**, 1693–1699 (1995).
- [24] G. Gioai and M. Ortiz: *Delamination of compressed thin films*. Adv. Appl. Mech. **33**, 119–192 (1997).
- [25] T. Ye, Z. Suo and A. G. Evans: *Thin film cracking and the roles of substrate and interface*. Int. J. of Solid Structures **29**, 2639–2648 (1992).
- [26] M. D. Thouless, A. G. Evans, M. F. Ashby and J. W. Hutchinson: *The edge cracking and spalling of brittle plates*. Acta Met. **35**, 1333–1341 (1987).
- [27] J. L. Beuth and N. W. Klingbeil: *Cracking of thin films bonded to elastic-plastic substrates*. J. Mech. Phys. Solids **44**, 1411–1428 (1996).
- [28] M. S. Hu and A. G. Evans: *The cracking and decohesion of thin films on ductile substrate*. Acta Mater. **37**, 917–925 (1989).
- [29] Z. Suo, C. F. Shih and A. G. Varias: *A theory for cleavage cracking in the presence of plastic flow*. Acta Metall. Mater. **41**, 1551–1557 (1993).
- [30] J. W. Hutchinson and A. G. Evans: *Mechanics of Materials: Top-Down Approaches to Fracture*. Acta Materialia (2000).
- [31] Harm, S.: *Profilanalyse winkelaufgelöster Photoelektronenspektren im Rahmen eines Fermi-Flüssigkeits-Modells*. Inst. f. Exp. Phys. der CAU Kiel (1994).
- [32] J.A. Wilson and A.D. Yoffe: *The transition metal dichalcogenides. Discussion and interpretation of the observed optical, electrical and structural properties*. Adv. Phys. **18**, 193 (1969).
- [33] J. Rouxel: *Intercalated Layered Materials*. , ed. F. A. Lévy (D. Reidel, Dordrecht) (1979).
- [34] M. Inoue, H. P. Hughes und A. D. Yoffe: *The electronic and magnetic properties of the 3d transition metal intercalates of  $TiS_2$* . Advances in Physics **38**, 565 (1989).
- [35] G. V. Subba Rao and M. W. Shafer: *Intercalated Layered Materials*. , ed. F. A. Lévy (D. Reidel, Dordrecht) (1979).
- [36] G. Binnig and H. Rohrer: *Scanning tunneling microscopy*. Helvetica Physica Acta **55**, 726 (1982).

- [37] S. Woedtke: *Untersuchung der elektronischen Struktur von  $C_{60}$ -Filmen auf  $GaAs(001)$* . Diplomarbeit, Inst. f. Exp. u. Ang. Phys. der CAU Kiel (1998).
- [38] Tersoff, J. und D.R. Hamann: *Theory of the scanning tunneling microscope*. Phys. Rev. B **31**(2), 805 (1985).
- [39] M. Traving, M. Boehme, L. Kipp, M. Skibowski, F. Starrost, E.E. Krasovskii, A. Perlov and W. Schattke: *Electronic structure of  $WSe_2$ : A combined photoemission and inverse photoemission study*. Phys. Rev. B **55**(15), 10392 (1997).
- [40] E.A. Jarvis und E.A. Carter. *Phys. Rev. B* **6**, 100103 (2002).
- [41] G. Neumann, M. Pfündstein und P. Reimers. *Phys. Status Solidi A* **64**, 225 (1981).
- [42] Angela Büttner: *Beitrag zur Entwicklung eines Membranreaktors: Herstellung dünner metallischer Schichten auf porösen keramischen Supporten*. Dissertation, Technische Fakultät der Christian-Albrechts-Universität zu Kiel (2003).
- [43] D.L.Greenaway and R.Nitsche. *J.Phys.Chem.Solids* **26**, 1445 (1965).
- [44] R. Kunz: *Epitaxie von  $PbS$  auf  $TiS_2$ : Untersuchung der geometrischen und elektronischen Struktur*. Diplomarbeit, IEAP CAU Kiel (2002).
- [45] J. Brandt: *Geometric and electronic structure of misfit layered compounds and epitaxial thin films of  $PbS$  on transition metal dichalcogenides*. Dissertation, IEAP CAU Kiel (2003).
- [46] J. I. Goldstein: *Scanning Electron Microscopy and X-Ray Microanalysis*. Plenum Press, New York (1992).
- [47] Paul A. Tipler: *Physik*. Spektrum Akademischer Verlag, Heidelberg (1994).
- [48] C. Ramírez, W. Schattke: *Diffusion and intercalation of alkali atoms in transition metal dichalcogenides*. Surf. Sci. **482–485**, 424–429 (2001).
- [49] Claudia del Pilar Ramírez García: *Ab initio Study of Alkali Diffusion and Intercalation on Transition Metal Dichalcogenides*. Dissertation, ITAP CAU Kiel (2003).
- [50] C. Ramírez, R. Adelung, R. Kunz, L. Kipp and W. Schattke: *Lithium adsorption by  $TiSe_2$  of varying concentration via density functional theory*. Phys. Rev. B **71** (2005).
- [51] R. Anton and I. Schneidereit: *In situ TEM investigations of dendritic growth of Au particles on HOPG*. Phys. Rev. B **58**, 13874 (1998).
- [52] R. Anton and P. Kreutzer: *In situ TEM evaluations of the growth kinetics of Au particles on highly oriented pyrolytic graphite at elevated temperatures*. Phys. Rev. B **61**, 16077 (2000).
- [53] M. Voigt, S. Dorsfeld, A. Volz und M. Sokolowski: *Nucleation and Growth of Molecular Organic Crystals in a Liquid Film under Vapor Deposition*. Phys. Rev. Let. **91**, 026103 (2003).

- 
- [54] R. Adelung: *From Dopants to Nanowires: Rubidium Adsorption on Layered Crystal Surfaces*. Dissertation, IEP CAU Kiel (2000).
- [55] R. Adelung, L. Kipp, J. Brandt, L. Tarcak, M. Traving, C. Kreis and M. Skibowski: *Nanowire networks on perfectly flat surfaces*. Appl. Phys. Lett. **74**, 3053 (1999).
- [56] R. Adelung, J. Brandt, K. Rossnagel, O. Seifarth, L. Kipp, M. Skibowski, C. Ramirez, T. Strasser, and W. Schattke: *Tuning dimensionality by nanowire adsorption on layered materials*. Phys. Rev. Lett. **68**, 1303 (2001).
- [57] R. Adelung, J. Brandt, L. Tarcak, L. Kipp, and M. Skibowski: *Charge density waves affected by Rb nanowire network formation on 1T-TaS<sub>2</sub>*. Appl. Surf. Sci. **162**.
- [58] R. Adelung, J. Brandt, L. Kipp, and M. Skibowski: *Reconfiguration of charge density waves by surface nanostructures*. Phys. Rev. B. **63**, 165327 (2001).
- [59] R. Adelung, F. Ernst, A. Scott, M. Tabib-Azar, L. Kipp, M. Skibowski, S. Hollensteiner, E. Spiecker, W. Jäger, S. Gunst, A. Klein, W. Jägermann, V. Zaporozhchenko, F. Faupel: *Self-Assembled Nanowire Networks by Deposition of Copper onto Layered-Crystal Surfaces*. Advanced Materials **14**, 1056 (2002).
- [60] C. Ramírez and W. Schattke: *Diffusion and Intercalation of Alkali Atoms in Transition Metal Dichalcogenides*. Surface Science **482-485**.
- [61] J. Brandt: *Der Einfluß von Nanostrukturen auf die geometrische und elektronische Struktur von metallischen Schichtkristallen*. Diplomarbeit, IEAP CAU Kiel (1999).
- [62] A. V. Skripov, D. S. Sibirtsev, Y. G. Cherepanov and B. A. Aleksashin: *Se NMR study of the charge density wave state in 2H - NbSe<sub>2</sub> and 1T - VSe<sub>2</sub>*. J. Phys.: Condens. Matter **7**, 4479-4487 (1995).
- [63] R. Adelung, O.C. Aktas, J. Frank, A. Biswas, R. Kunz, M. Elbahri, J. Kanzow, U. Schürmann, and F. Faupel: *Strain controlled growth of nanowire within thin film cracks*. Nature Materials **3**, 375 (2004).

## List of abbreviations

BZ	Brillouin zone
CBM	conduction band minimum
CDW	charge-density wave
CVT	chemical vapor transport
DOS	density of states
EDX	energy dispersive X-ray
LDOS	local density of states
ODDS	one-dimensional density of states
PLD	periodic lattice distortion
RBM	rigid band model
RT	room temperature
SBZ	surface Brillouin zone
SDOS	surface density of states
SEM	scanning electron microscope
STM	scanning tunneling microscope
TED	transmission electron diffraction
TEM	transmission electron microscope
TMDC	transition metal dichalcogenide
UHV	ultrahigh vacuum
VBM	valence band maximum
XPD	X-ray photoelectron diffraction
XPS	X-ray photoelectron spectroscopy
XRD	X-ray diffraction

## List of publications

### International journals

1. C. Ramírez, R. Adelung, R. Kunz, L. Kipp and W. Schattke,  
*Lithium adsorption by  $TiSe_2$  of varying concentration via density functional theory*,  
in: Phys. Rev. B 71, 035426, 2005
2. R. Adelung, R. Kunz, F. Ernst, L. Kipp, M. Skibowski,  
*Self-Organized Structures on Flat Crystals: Nanowire Networks Formed by Metal Evaporation*,  
in: Advances in Solid State Physics 43 (Ed. B. Kramer), Springer, Heidelberg, 463-476 (2003) .
3. R. Adelung, O.C. Aktas, J. Frank, A. Biswas, R. Kunz, M. Elbahri, J. Kanzow, U. Schürmann, and F. Faupel,  
*Strain controlled growth of nanowire within thin film cracks*,  
**Nature Materials**, 3, 375, (2004)
4. A. Biswas, R. Kunz, M. Elbahri, R. Adelung, O.C. Aktas, U. Schürmann, H. Takele, V. Zaporojtchenko, F. Faupel and T. Strunskus,  
*Helical-like microwire arrays of Ag with visible wavelength transparent plasmonic response at near UV and mid IR regions*,  
Appl. Phys. Lett., in press, (2004)
5. J. Brandt, R. Kunz, L. Kipp, M. Skibowski, E. Spiecker, W. Jäger,  
*Epitaxial growth of thin PbS films on  $TiS_2$  and comparison to the misfit layered compound  $PbS_{1.18}TiS_2$* ,  
in preparation
6. R. Kunz and R. Adelung,  
*A Production Method for Aligned Nanowires on Arbitrary Materials*,  
MRS Spring Meeting Proceedings, M.3.51, 2004

### International conferences

1. R. Kunz and R. Adelung,  
*A Production Method for Aligned Nanowires on Arbitrary Materials*,  
Spring Meeting of the Material Research Society 2004, San Francisco,  
Posterpresentation.

### National conferences

1. R. Kunz, J. Brandt, L. Kipp and M. Skibowski,  
*Vergleich der elektronischen Struktur von  $(PbS)TiS_2$  und epitaktischen PbS-Lagen auf  $TiS_2$* ,  
Springmeeting der Deutschen Physikalischen Gesellschaft,  
Regensburg 2002, Posterpräsentation



2. R. Kunz and R. Adelung,  
*Selbstorganisation von Kupfer-Nanostrukturen auf strukturlosen Oberflächen*,  
Springmeeting der Deutschen Physikalischen Gesellschaft,  
Dresden 2003, Posterpräsentation
3. A. Kamenz, R. Kunz, J. Brandt, L. Kipp and M. Skibowski,  
*Geometric and electronic structure of epitaxial PbS on TiS<sub>2</sub>*,  
Springmeeting der Deutschen Physikalischen Gesellschaft,  
Dresden 2003, Posterpräsentation
4. R. Kunz and R. Adelung,  
*Metal diffusion on transition metal dichalcogenide surfaces*,  
Springmeeting der Deutschen Physikalischen Gesellschaft,  
Regensburg 2004, Talk

### Research reports

1. J. Brandt, R. Kunz, L. Kipp and M. Skibowski,  
*On the valence band maximum of PbS*,  
HASYLAB Annual Report 2001.
2. J. Brandt, R. Kunz, L. Kipp and M. Skibowski,  
*The electronic structure of epitaxial PbS on TiS<sub>2</sub>*,  
HASYLAB Annual Report 2002.



## Acknowledgements

As a member of the chair for multicomponent materials I enjoyed the work in a multicultural as well as lively group. It was often very funny and I am sad to leave this group but I am also looking forward to new duties. The solidarity and cooperativeness is extraordinary and is the merit of each single person of the chair. Therefore, I would like to thank all members of the chair for the good companionship.

In particular, I would thank my thesis advisors Prof. Dr. Franz Faupel and Dr. Rainer Adelung for the opportunity to work on my research project and to realize my own ideas and the group of Prof. Dr. Lutz Kipp for supplying the crystals. I wish to thank them for many fruitful discussions and their continuous support.

Very big thanks to my officemates Dr. Klaus Rätzke, Dr. Angela Büttner and Henry Greve for scientific and private advices or discussions and bearing me the last years.

Stefan Rehders, his person and his engineering are a benefit for the group. I will miss him also as a character, giving me new hope and strength for the future.

Special thanks to Rainer Kloth, his experience in computer systems, particular of the group, and his answers to many of my questions with regard to hard- and software made the work much easier.

Further, I wish to thank Beate Minten and her gentle manner not only for solving various problems with different application forms but also for understanding my itchy feet.

I am also very grateful to Dr. Vladimir Zaporozhchenko, Dr. Jurgita Zekonyte, Ulrich Schürmann, Haile Takele, Alexander Bartsch, Christian Pochstein, Mady Elbahri and Sebastian Wille for being the best imaginable fellows.

At least, I would like to thank again several persons. I would like to thank my girlfriend Dr. Julia Brandt. She helps me to find my tongue in order to express the complex observations in this thesis. Dear Jan Kruse, I would like to return thanks for the review of the whole thesis and the helpful advices and Michael Scharnberg for his remarks on the final important chapters. Dr. Rainer Adelung has to be mentioned again as the person, who believed in my ideas and the interpretation of the results and often he found the words helping me to describe the results.

As already mentioned, the whole group consists of different persons. One remarkable point is the following: Irrespectively of the main topic during lunch often the fundamental topic at the end of lunch are manners of death. Why?

The work in this thesis was supported by the Deutsche Forschungsgemeinschaft, Forschergruppe 353/2-1, giving me the opportunity to observe new structures for the first time.

# Lebenslauf

Rainer Kunz  
Waisenhofstr. 27  
geboren am 21. September 1972 in Preetz  
deutsche Staatsangehörigkeit

- 1979 – 1983 Friedrich-Ebert-Schule in Preetz  
1983 – 1985 Theodor-Heuss-Schule in Preetz  
1985 – 1989 Bildungszentrum Kiel-Mettenhof  
1989 – 1992 Gymnasium Kiel-Elmschenhagen  
Mai 1992 Allgemeine Hochschulreife
- 1992 – 2002 Studium der Physik an der  
Christian-Albrechts-Universität zu Kiel
- November 1997 Diplomvorprüfung
- Mai 2001 Diplomhauptprüfung der Physik
- 2001 – 2002 Diplomarbeit bei Prof. Dr. L. Kipp zum Thema:  
*Epitaxie von PbS auf TiS<sub>2</sub>: Untersuchung der geometrischen und elektronischen Struktur*
- Juli 2002 Beginn der Dissertation bei Prof. Dr. F. Faupel  
2002 – 2005 wissenschaftlicher Angestellter an der Technischen  
Fakultät der Christian-Albrechts-Universität zu Kiel

# Eidesstattliche Erklärung

Hiermit erkläre ich an Eides Statt, daß ich diese Arbeit selbständig unter der Beratung meiner wissenschaftlichen Lehrer und nur mit den angegebenen Hilfsmitteln erstellt habe.

Diese Arbeit wurde weder ganz noch in Teilen an anderer Stelle im Rahmen eines Prüfungsverfahrens vorgelegt.

Frühere Promotionsversuche wurden von mir nicht vorgenommen.

Kiel, den

# Kurzfassung

Das Aufbringen von dünnen metallischen Filmen auf Substrate ist einer der wichtigsten Prozessschritte in modernen Technologien, wie z.B. in CMOS Technologien, ohne die die aktuelle Informations- und Kommunikationstechnik nicht denkbar wären, oder in der Mikrosystemtechnik, die immer mehr Anwendung in der Sensorik und Aktorik findet. Es ist daher von immanenter Wichtigkeit, Keimbildung und Wachstum dieser Schichten zu verstehen und zu kontrollieren. Die atomar glatten und inerten Oberflächen von Kristallen der Klasse der Übergangmetalldichalkogenide (ÜMDC) bieten hier ein besonderes Modellsystem, anhand dessen die einflussreichsten Kerngrößen für Wachstum und Strukturbildung untersucht werden können. Die vorliegende Arbeit geht dabei weit über die bereits bekannten Aspekte der Alkalimetalladsorption auf ÜMDC hinaus, und unterzieht sie einer neuen und weitergehenden Betrachtung. Bisher beschränkten sich die Untersuchungen zu diesem Thema auf wenige Metalle wie z.B. Alkalimetalle, die im technisch interessanten Maßstab nicht handhabbar sind. Im Rahmen dieser Arbeit wurden daher technologisch relevante Adsorbatmetalle wie Chrom, Silber oder Kupfer für die Präparation ausgewählt und die beobachteten Adsorbatstrukturen systematisch mittels verschiedenster Methoden (SEM, EDX, AFM) untersucht. Eine Grundvoraussetzung für eine systematische Untersuchung ist die Erhaltung von konstanten Bedingungen während der Präparation. Um diese zu gewährleisten, mußte im Rahmen dieser Arbeit zunächst eine neue Präparationskammer konstruiert werden. Die erfolgreiche Inbetriebnahme dieser Kammer erlaubte eine systematische Variation der Depositionsparameter (Depositionsmenge und Substrattemperatur) und ermöglichte es so, deren Einfluß auf die Wachstumsparameter und die entstandenen Strukturen zu untersuchen. Es zeigte sich eine bisher unbekannte Strukturvielfalt der Adsorbate auf der Kristalloberfläche, die stark von dem System Adsorbat/Substrat, der Depositionsmenge und der Substrattemperatur abhing. Für weitergehende Untersuchungen wurde als Adsorbat Kupfer ausgewählt, da dieses heute als technologisch sehr interessant gilt. Es konnten neben dem bekannten Clusterwachstum erstmals auch geometrisch angeordnete Kupfercluster beobachtet werden. Bei einigen Kristallen kam es bedingt durch die Wechselwirkung zwischen Adsorbat und Substrat zu einer Zerstörung der Kristalloberfläche und der Ausbildung von Netzwerken aus teilweise aufgefalteten Kristallschichten, die sich mit den herkömmlichen Theorien zur Clusterbildung und Dünnschichtwachstum nicht erklären lassen. Hier müssen komplexe Bruchmechanismen der Substratkristalle berücksichtigt werden, die sich analytisch nicht beschreiben lassen. Einen Kernaspekt für das Adsorbatwachstum stellt das Diffusionsverhalten der aufgetragenen Materialien dar. Um die Diffusion von Kupfer auf den Kristallen systematisch untersuchen zu können, wurde eine völlig neue Methode entwickelt. Hierbei werden die Kristalle vor der Präparation maskiert. Nach der Kupferpräparation wurde die Maske entfernt, und die verschiedenen Oberflächen konnten untersucht werden. Als Ergebnis erhält man klar definierte Oberflächenbereiche ohne direkte Kupferdeposition, die direkt an Bereiche angrenzen, auf welche die Kupferatome direkt deponiert worden sind. Anhand des Verlaufes des EDX Signals im Elektronenmikroskop konnten fundamentale Aussagen über das Diffusionsverhalten von Kupfer auf verschiedenen Oberflächen getroffen werden. Eine weitere Methode zur Untersuchung des Wachstums beruht auf einer Vorstrukturierung der Substratkristalle durch einen fokussierten Ionenstrahl. Die bisherigen Ergebnisse deuten allerdings darauf hin, daß es während des Vorstrukturierungsprozesses zu einer Kontamination der Oberfläche kommt, was die Beobachtung von Strukturen in diesem Bereich erschwert bis unmöglich macht. In diesem Bereich

muß die Meßmethodik noch weiter verfeinert werden. Insgesamt konnte gezeigt werden, daß es bei der Deposition von Metallen auf ÜMDC Kristallen zu einer bisher unbekanntem Strukturvielfalt kommt. Diese große Vielfalt wurde in den Zusammenhang mit theoretischen Modellen gesetzt und anhand der entscheidendsten Einflußgrößen diskutiert. Neben der Zerstörung der Kristalloberfläche durch die Wechselwirkung Adsorbat/Substrat wurde als bestimmende Größe für die Strukturentstehung die Diffusionslänge der Adsorbatatome erkannt, die anhand von neu entwickelten Verfahren gemessen werden konnte und tatsächlich auf ein starkes Abweichen von üblichen Wachstumsmodellen hinweist.

## Abstract

The deposition of metallic thin films on substrates is one of the most important process steps in modern technology. Without CMOS technology for example, neither the modern information and communication technology nor the microsystem technology and its progressive application to sensor and actor devices is conceivable. Therefore, it is of immanent importance to understand and to control the nucleation and the growth process of such films. The atomically flat and inert surfaces of crystals belonging to the class of transition metal dichalcogenides (TMDC) offer a special model system to investigate the growth and structure formation. The present work goes far beyond the already known aspects of alkali metal adsorption on TMDC and will consider it in a new and further manner. Until now, the investigations of this topic were restricted to only few metals like, e.g. alkali metals, which cannot be handled on a technological scale. In this thesis, technologically relevant adsorbate metals like chromium, silver or copper were chosen and the adsorbate structures were investigated by different experiments (SEM, EDX, AFM). One basic requirement for a systematic investigation is the conservation of constant preparation conditions. Therefore, a completely new preparation chamber had to be constructed. The successful operation of the chamber enables the variation of the deposition parameters (deposition amount, substrate temperature) systematically and offers the possibility to investigate the influence of the deposition parameters on the growth parameters and on the occurring structures. On the crystal surfaces a large unknown variety of structures can be observed, depending highly on the adsorbate/substrate system, amount of deposited metal and substrate temperature. For further investigations copper as technologically very interesting adsorbate material was chosen. Besides the known cluster growth, geometrically arranged copper cluster formations were observed. On some crystals, due to the interaction between adsorbate and substrate a destruction of the crystal surface takes place. The formation of a network that consists of upfolded crystal surface layers was observed which cannot be explained by the conventional theories of cluster and thin film growth. In this case, one has to consider the complex fracture mechanisms of the substrate crystals which cannot be described analytically. One main aspect for the adsorbate growth is the diffusion length of the deposited material. In order to investigate the diffusion of copper on the crystals systematically a completely new method was developed. Therefore, the crystals were masked prior to film preparation. After the copper deposition the mask was removed and the surfaces were investigated. The resulting surfaces consist of well defined areas where no direct copper deposition took place adjacent to areas where copper is directly deposited. Fundamental statements of the diffusion behavior on the crystals could be given by monitoring the distribution of the copper signal by EDX using the electron microscope. A further method for investigation of the growth process is the pre-structuring of the substrate by a focussed ion beam. The obtained results point to a contamination of the crystal surface during the structuring process. Thus, investigations of structures in these areas are complicated or even impossible. This method of research has to be refined. In the whole it could be shown that the deposition of metals on TMDC leads to an unknown variety of structures. This large variety was discussed in the context of existing theoretical models of growth phenomena and the dominating growth parameters. In addition to the interaction of adsorbate/substrate and the resulting destruction of the crystal surface, the diffusion length of the adsorbate atoms is identified as one dominating parameter for the structure formation. A new method for measuring this quantity demonstrates the distinct deviation from general growth concepts.